

AN ABSTRACT OF THE DISSERTATION OF

Craig M. Smith for the degree of Doctor of Philosophy in Atmospheric Sciences
presented on May 24, 2010.

Title: A Modeling Study of Downslope Windstorms

Abstract approved: _____.

Eric Skillingstad

The generation mechanism for downslope windstorms was shown to vary according to inversion height and strength using a series of numerical experiments. Strong low level inversions were dominated by interfacial waves on the inversion, while high level inversion and cases without an inversion were dominated by internal gravity wave (IGW) breaking. For cases with an inversion at intermediate heights the following mechanisms of downslope windstorm formation were explored and discarded: trapping of IGW energy in the lower layer by an inversion, nonlinear IGW breaking, and subcritical to supercritical transition of the interfacial mode on the inversion. The remaining mechanism of downslope windstorm formation for this case was shown to be a direct result of mountain wave induced instabilities on the inversion and associated coupling of the stagnation zone with the lee surface jet. The generation of the stagnation zone is

due to imbalances in the momentum budget equation which lead to a pocket of neutrally stratified stagnant air which propagates back to the ridge and amplifies. Amplification of the perturbation and overturning of isotherms lead initially to buoyant production of turbulence and subsequently to shear production of TKE along the bottom of the stagnation zone and upper part of the surface jet. This shear production acts to grow the stagnation zone downstream, forcing the flow beneath the inversion into a lee jet beneath and leading to the creation of a downslope windstorm. The inversion instability mechanism suggests a scenario in which downslope windstorms may occur when neither a barotropic transition nor IGW breaking are predicted, and mesoscale models may not be able to adequately resolve relevant turbulent processes.

Next, an analysis of observations is presented which explores the effect of surface heat fluxes on downslope windstorms. The observations of downslope windstorms on the Falkland Islands revealed a number of interesting characteristics. Most of the observed events are of limited downstream extent. Those that do extend far downstream tend to occur in conjunction with a strong low level inversion, while those of limited length more often occur in conjunction with weaker inversions. Finally, downslope windstorms often occur at night. Two specific case studies of events are presented which are indicative of these larger trends.

A series of simplified numerical experiments are presented which explore the effect of surface heat fluxes on downslope windstorms using an eddy resolving

model. Initially we focus on IGW breaking and lee wave rotors without an upstream inversion. In the basic case with no surface heating, a typical nonlinear wave response was produced, with a lee side surface jet and a large zone of stagnant air above the lee side of the mountain that eventually resulted in overturning of isotherms and generation of turbulence. Turbulence is generated initially by overturning isotherms in the nascent stagnation zone, and then by shear production along the edges of the stagnation zone, especially at the interface with the surface jet on the lee of the slope. Over time, a series of trapped waves or rotors formed in the lee of the ridge, with the first rotor representing the separation of the lee side jet from the mountain slope.

Weak surface heat flux was found to reduce rotor strength and increase rotor heights. Strong surface heating prevented the formation of rotors entirely and produced a much weaker downslope wind event. Experiments with heating confined to either the upstream or downstream side of the mountain suggest that locally generated turbulence on the downstream side of the mountain is more important in controlling the rotor behavior than turbulence advected over the mountain from the upstream boundary layer. The application of moderate surface cooling led to a train of lee side waves capped by a jet of increased streamwise winds. Increased stratification from surface cooling was found to be important in the formation of a stably stratified undulating jet, which capped the rotors. Shear between this jet and the rotors generated increased turbulence in the rotors

themselves, while buoyant destruction of TKE in the rotor downdrafts acted to maintain the rotor circulations for a longer distance downstream from the ridge.

Next a series of experiments were presented which explored the effect of surface heat fluxes which occur in conjunction with a strong ridgetop level inversion. Surface heating was shown to reduce lee jet length due to transport of TKE over the ridge and buoyant production of TKE in the lee of the ridge. Surface cooling applied to a low inversion case with a fully turbulent neutrally stratified boundary layer resulted in an increase in jet length. The katabatic contribution to this jet length was fairly significant far away from the slope, which seems to be in agreement with observations from the Falkland Islands.

The series of cases presented with a medium height level inversion presented an even more extreme example of surface heating leading to a complete absence of downslope windstorms. It was suggested that this is due to the lack of mountain wave induced perturbation on the inversion. When surface cooling was applied to a medium inversion case with a fully turbulent neutrally stratified boundary layer, the lee flow transitioned to downslope windstorm. The transition which occurred resulted in a jet which, besides additional near surface stratification, was not much stronger than the no heating case and katabatic contributions to the cooling case were minimal.

A number of forecasting considerations are implied by this research: downslope windstorms over a low ridge may preferentially occur at night, daytime events may be of limited downstream extent, and downslope windstorms which

occur in conjunction with an inversion may not be adequately predicted by IGW breaking or interfacial wave considerations, or non-eddy resolving mesoscale models.

© Copyright by Craig Smith

May 24, 2010

All rights reserved

A Modeling Study of Downslope Windstorms

by

Craig M. Smith

A DISSERTATION

submitted to

Oregon State University

in partial fulfillment of

the requirements for the

degree of

Doctor of Philosophy

Presented May 24, 2010

Commencement June 2010

Doctor of Philosophy dissertation of Craig M. Smith presented on May 24, 2010.

Approved:

Major Professor, representing Atmospheric Sciences

Dean of the College of Oceanic and Atmospheric Sciences

Dean of the Graduate School

I understand that my dissertation will become part of the permanent collection of Oregon State University libraries. My signature below authorizes release of my dissertation to any reader upon request.

Craig M. Smith, Author

ACKNOWLEDGMENTS

I would like to express thanks and appreciation to my adviser, Dr. Eric Skyllingstad, for providing me with an interesting research topic and being an source of guidance and help to improve my study. It has been my pleasure to work with him. I would also like to thank April Lindeman for her support and friendship.

This research was funded by the National Science Foundation under grant ATM-0527790. We are pleased to acknowledge the super-computer time provided by the National Center by Atmospheric Research, which is funded by the National Science Foundation.

TABLE OF CONTENTS

	<u>Page</u>
1. Introduction	1
1.1 Mechanisms of downslope windstorm formation	1
1.2 Influence of surface heat fluxes and slope flows on downslope windstorms	3
2. Investigation of upstream boundary layer influence on mountain wave breaking and lee wave rotors using a large eddy simulation	5
Abstract	6
2.1 Introduction	7
2.2 Model introduction and setup	11
2.3 Results	13
2.4 Conclusions	23
Acknowledgements	27
Figures	28
Tables	38
3. An inversion based instability mechanism for downslope windstorms	39
Abstract	40
3.1 Introduction	41
3.2 Model introduction and setup	44
3.3 Inversion height results	46
3.4 Mountain height results	54
3.5 Conclusions	58

TABLE OF CONTENTS (Continued)

	<u>Page</u>
Acknowledgements	59
Figures	62
Tables	70
4. Slope flow-downslope windstorm interaction over a low 2-D ridge	71
Abstract	72
4.1 Introduction	73
4.2 Observations of downslope windstorms on the Falkland Islands	75
4.3 Numerical experiments	78
4.4 Conclusions	84
Acknowledgements	85
Appendix	86
Figures	87
Tables	94
5. Conclusions	95
5.1 Mechanisms of downslope windstorm formation	95
5.2 Influence of surface heat fluxes and slope flows on downslope windstorms	96
References	100

LIST OF FIGURES

<u>Figure</u>	<u>Page</u>
2.1 Schematic showing the channel flow configuration used in the simulations.	28
2.2 Close up view of a) streamwise velocity (shading in ms^{-1}), b) vertical velocity (shading in ms^{-1}), and c) average TKE (shading in m^2s^{-2}) and potential temperature (lines of constant $^{\circ}\text{C}$) for the no heating case at $t = 180$ min (left column), $t = 205$ min (middle column) and $t = 235$ min (right column).	29
2.3 Close up view of average TKE budget terms of a) buoyant production of TKE and b) shear production of TKE (shading in m^2s^{-3}) and potential temperature (lines of constant $^{\circ}\text{C}$), for the no heating case at $t = 215$ min (left column) and $t = 235$ min (right column).	30
2.4 Inflow near surface velocity (a), potential temperature (b), and TKE (c) profiles at $y = 4$ km for the experiments at $t = 200$ min.	31
2.5 Close up view of a) streamwise velocity (shading in ms^{-1}), b) vertical velocity (shading in ms^{-1}), and c) average TKE (shading in m^2s^{-2}) and potential temperature (lines of constant $^{\circ}\text{C}$) at $t = 220$ min for the no heating case (left column), weak heating case (2 nd column), strong heating case (3 rd column) and cooling case (right column).	32
2.6 Close up view of average TKE budget terms of a) buoyant production of TKE and b) shear production of TKE (shading in m^2s^{-3}) and potential temperature (lines of constant $^{\circ}\text{C}$) at $t = 220$ min for the no heating case (left), strong heating case (middle) and cooling case (right).	34
2.7 Close up view of a) streamwise velocity (shading in ms^{-1}), b) vertical velocity (shading in ms^{-1}), and c) average TKE (shading in m^2s^{-2}) and potential temperature (lines of constant $^{\circ}\text{C}$) at $t = 230$ min for the upstream heating case (left), and downstream heating case (right).	35

LIST OF FIGURES (Continued)

<u>Figure</u>	<u>Page</u>
2.8	Close up view of average TKE budget terms of a) buoyant production of TKE and b) shear production of TKE (shading in m^2s^{-3}) and potential temperature (lines of constant $^{\circ}\text{C}$) for the upstream heating case (left) and downstream heating case (right) at $t = 230$ min. 36
2.9	Integrated turbulent flux for no heating, weak heating, upstream heating, and downstream heating cases at $t = 195$ min. 37
2.10	Close up view of spanwise vorticity (shading in s^{-1}) and vectors of flow velocity at $t = 205, 210,$ and 215 min for the no heating case. 37
3.1	Schematic showing the channel flow configuration used in the simulations. 62
3.2	Close up view of streamwise velocity (shading in ms^{-1}) and potential temperature (lines of constant $^{\circ}\text{C}$) for the a) no inversion case at $t = 360$ min, b) low inversion case at $t = 120$ min c) medium inversion case at $t = 360$ min, and d) high inversion case at $t = 200$ min. 62
3.3	Close up view of streamwise velocity (shading in ms^{-1}) and potential temperature (lines of constant $^{\circ}\text{C}$) for the medium inversion case at a) $t = 60$ min, a) $t = 90$ min, a) $t = 150$ min, and d) $t = 240$ min. 63
3.4	Shallow water mode Froude number versus streamwise distance for the low inversion, medium inversion and high inversion cases at the times presented in figure 3.2. 63
3.5	Close up view of average TKE (shading in m^2s^{-2}) and potential temperature (lines of constant $^{\circ}\text{C}$) for the a) low inversion case at $t = 120$ min and b) medium inversion case at $t = 360$ min and TKE budget terms of shear production of TKE (shading in m^2s^{-3}) and potential temperature (lines of constant $^{\circ}\text{C}$) for the c) low inversion case at $t = 35$ min and d) medium inversion case at $t = 210$ min. 64

LIST OF FIGURES (Continued)

<u>Figure</u>	<u>Page</u>
3.6	Close up view of Richardson number and potential temperature (lines of constant $^{\circ}\text{C}$) for the a) no inversion case at $t = 150$ min, b) low inversion case at $t = 20$ min c) medium inversion case at $t = 110$ min, and d) high inversion case at $t = 100$ min. 65
3.7	Vertical profiles of buoyancy (s^{-2}) (top row) and streamwise velocity (ms^{-1}) (bottom row) as a function of height at various times used in the instability analysis for the medium inversion case at a) $t = 60$ min, b) $t = 90$ min and c) $t = 100$ min (stable profiles are solid, unstable profiles are dashed). 65
3.8	Close up view of sum of momentum budget terms of advection and pressure gradient (shading in ms^{-2}) and potential temperature (lines of constant $^{\circ}\text{C}$) for the medium inversion case at $t = 105$ min for a) the horizontal momentum budget and b) the vertical momentum budget. 66
3.9	Close up view of streamwise velocity (shading in ms^{-1}) and potential temperature (lines of constant $^{\circ}\text{C}$) for the a) inversion $Nh/\nu = 0.4$ case at $t = 240$ min, b) no inversion $Nh/\nu = 0.9$ case at $t = 420$ min and c) inversion $Nh/\nu = 0.9$ case at $t = 360$ min. 66
3.10	IGW KE aloft versus Nh/ν for the experiments listed in Table 2. 67
3.11	Vertical profiles of buoyancy (s^{-2}) (top rows) and streamwise velocity (ms^{-1}) (bottom rows) as a function of height at various times for the inversion $Nh/\nu = 0.4$ case at a) $t = 180$ min), b) $t = 240$ min), and c) $t = 300$ min), and inversion $Nh/\nu = 0.9$ case d) $t = 80$ min), e) $t = 110$ min), and f) $t = 130$ min. 67
3.12	Vertical profiles of a) potential temperature (K) and b) streamwise velocity (ms^{-1}) as a function of height used to initialize 3-D instability simulations. 68
3.13	Close up view of sum of horizontal momentum budget terms of advection and pressure gradient (shading in ms^{-2}) and potential temperature (lines of constant $^{\circ}\text{C}$) for the a) inversion $Nh/\nu = 0.4$ case at $t = 180$ min, and b) inversion $Nh/\nu = 0.9$ case at $t = 140$ min. 68

LIST OF FIGURES (Continued)

<u>Figure</u>	<u>Page</u>	
3.14	Close up view of sum of vertical momentum budget terms of advection and pressure gradient (shading in ms^{-2}) and potential temperature (lines of constant $^{\circ}\text{C}$) for the a) inversion $Nh/\nu = 0.4$ case at $t = 240$ min, and b) inversion $Nh/\nu = 0.9$ case at $t = 120$ min.	69
4.1	The location of the stations on the East Falkland Island used in this analysis. Terrain height (m) is shaded.	87
4.2	Diurnal variation of a) northerly wind events and b) southerly wind events for stations #05 and #24.	87
4.3	Percentage of northerly wind events which occur at station #5 only, and stations #5 and #1 contemporaneously.	88
4.4	Percentage of northerly wind events whose correlated soundings have a) $\Delta\theta < 4$ K and b) $\Delta\theta > 4$ K which occur at station #5 only (left bar), and stations #5, and #1 contemporaneously (right bar). ...	88
4.5	Northerly wind velocity at stations #01, #05, and #24 versus Time for a) 6am 8/12/01 to 6pm 8/13/01 (LST), and b) 6am 1/26/01 to 6pm 1/27/01 (LST).	89
4.6	Temperature (left column) and northerly wind velocity (right column) versus height for the soundings taken between a) 8pm 8/12/01 to 8pm 8/13/01 (LST) and b) 8pm 1/26/01 to 8pm 1/26/01 (LST).	89
4.7	Schematic showing the channel flow configuration used in the simulations.	90
4.8	Close up view of streamwise velocity (shading in ms^{-1}) and potential temperature (lines of constant $^{\circ}\text{C}$) for the a) low inversion case at $t = 180$ min, b) low inversion heating case at $t = 180$ min c) and low inversion cooling case at $t = 390$ min. ...	90
4.9	Close up view of average TKE (shading in m^2s^{-2}) and potential temperature (lines of constant $^{\circ}\text{C}$) for the a) low inversion case at $t = 180$ min, b) low inversion heating case at $t = 180$ min c) and low inversion cooling case at $t = 350$ min. ...	90

LIST OF FIGURES (Continued)

<u>Figure</u>	<u>Page</u>
4.10	Close up view of streamwise velocity (shading in ms^{-1}) and potential temperature (lines of constant $^{\circ}\text{C}$) for the a) low inversion cooling case at a) $t = 260$ min, and b) $t = 280$ min. 91
4.11.	Close up view of streamwise velocity (shading in ms^{-1}) and potential temperature (lines of constant $^{\circ}\text{C}$) for the a) medium inversion case at $t = 360$ min, b) medium inversion heating case at $t = 300$ min c) and medium inversion cooling case at $t = 630$ min. 91
4.12	Close up view of average TKE (shading in m^2s^{-2}) and potential temperature (lines of constant $^{\circ}\text{C}$) for the a) medium inversion case at $t = 360$ min, b) medium inversion heating case at $t = 300$ min c) medium inversion cooling case at $t = 600$ min. 91
4.13	Close up view of streamwise velocity (shading in ms^{-1}) and potential temperature (lines of constant $^{\circ}\text{C}$) for the a) medium inversion upstream heating case at $t = 300$ min, b) medium inversion downstream heating case at $t = 360$ min. 92
4.14	Close up view of average TKE (shading in m^2s^{-2}) and potential temperature (lines of constant $^{\circ}\text{C}$) for the a) medium inversion upstream heating case at $t = 300$ min, and b) medium inversion downstream heating case at $t = 360$ min. 92
4.15	Close up view of streamwise velocity (shading in ms^{-1}) and potential temperature (lines of constant $^{\circ}\text{C}$) for the medium inversion cooling case at a) $t = 380$ min, b) $t = 480$ min and c) $t = 520$ min. 92
4.16	Close up view of streamwise velocity (shading in ms^{-1}) and potential temperature (lines of constant $^{\circ}\text{C}$) for the medium inversion a) strong cooling katabatic flow case at $t = 150$ min and b) weak cooling katabatic flow case at $t = 180$ min. 93
4.17	Velocity profiles of the a) low inversion and b) medium inversion katabatic flow and katabatic-downslope flows at $y = 65\text{km}$ (left) and $y = 75$ km (right). 93

LIST OF TABLES

<u>Table</u>		<u>Page</u>
2.1	List of all simulations and their characteristics	38
3.1	List of all simulations and their characteristics	70
3.2	List of inversion height experiments	70
4.1	List of all simulations and their characteristics.....	94

1 Introduction

Downslope windstorms occur in the lee of many mountain ridges worldwide. They often result in significant structural damage and can loft vast amounts of dust into the boundary layer. Aloft, downslope windstorms often occur in conjunction with rotors and significant variability of vertical velocity resulting in significant hazards to airplanes. Downslope windstorms are part of larger set of phenomena by which the Earth's surface may exert drag on the atmosphere.

1.1 Mechanisms of downslope windstorm formation

The two main theories of downslope windstorm formation are that of internal gravity wave (IGW) breaking and subcritical to supercritical transition of the barotropic mode. The crucial difference between the two is that the latter requires an inversion to support an interfacial mode, which cannot propagate vertically, while the former does not require an inversion and instead depends on the vertical propagation of IGWs in a continuously stratified system. In some circumstances vertical propagation of IGW energy in a continuously stratified system can be constrained through the creation of a self-induced critical layer via IGW breaking, a well documented example of which is that of the January 11, 1972 Boulder downslope windstorm (Lilly and Zipser 1972; Clark and Peltier 1977; Peltier and Clark 1979; Doyle et al. 2000). Over the very same Front Range of the Rocky Mountains, Brinkmann (1974) and Bower and Durran (1986), instead show that downslope windstorms tend to occur in conjunction with upstream inversions. The same has been suggested for the Sierra Nevada's (Colson 1954, Kuettner 1959), and in Southeast Alaska (Colman and Dierking 1992). Colle and Mass (1998), however, showed that crest level stability was less correlated with strong lee flow winds than wind speed at ridge top level over the Washington Cascades. Both the bora and foehn are sometimes attributed to interfacial physics on an inversion, and sometimes occur due to

IGW breaking (Glasnovic and Jurcec 1990, Klemp and Durran 1987, Gohm and Mayor 2005, Belusic et al. 2007, Flamant et al. 2002, Klemp et al. 1997, Gohm et al. 2008, Gohm and Mayor, 2004).

Observations on the Falkland Islands (Mobbs et al. 2005) illustrate the ambiguity succinctly. First the authors show a direct correlation between downslope windstorms and non-dimensional mountain height,

$$\hat{h} = \frac{Nh}{v} \quad (1)$$

where N is the Brunt-Vaisala frequency,

$$N = \sqrt{\frac{g}{\theta_0} \frac{\partial \theta}{\partial z}}, \quad (2)$$

h is the ridge height, v is the cross-ridge velocity, g is the acceleration due to gravity, θ is the potential temperature, and θ_0 is a reference potential temperature, suggesting that IGW nonlinearity and breaking is the dominant mechanism for the downslope windstorms. Then the authors show a correlation between downslope windstorms and the Froude number,

$$Fr = \frac{v}{\sqrt{g' z_i}} \quad (3)$$

where the reduced gravity, and g' is defined as

$$g' = g \frac{\Delta \theta}{\theta_0} \quad (4)$$

and z_i is the height of the inversion, suggesting that interfacial wave phenomena, of which the Froude number is a measure of, is the dominant physics for the downslope windstorm formation.

Taken together, these studies suggest that many uncertainties remain regarding the distinction between downslope windstorms associated with elevated inversions and those associated with IGW breaking, and that the presumed dichotomy between two different mechanisms of downslope windstorm formation is not entirely unambiguous, especially considering that the criteria for inversion based windstorms may be substantially different than that of IGW breaking in a continuously stratified system.

1.2 Influence of surface heat fluxes and slope flows on downslope windstorms

While the onset and decay of downslope windstorm events is frequently tied to synoptic scale processes in the atmosphere such as the passage of a front over a mountain range, downslope windstorms can also occur with little change in synoptic scale forcing. Boundary layer processes are one example of phenomena which may affect the strength and duration of downslope windstorm events, but little is known about the extent to which they may be affected by surface heat fluxes on diurnal time scales. Although synoptic scale features which aid in forecasting strong downslope winds have been studied by a number of researchers (Colle and Mass 1998a and 1998b; Brinkmann, 1974; Czyzyk and Runk, 2006), there have been few observational studies that have focused on the influence of the surface heat fluxes and boundary layer structure on mountain waves. A few studies have shown observations which suggest preferred times for wind storm and rotor formation in the lee of three major mountain ranges: the Sierra Nevadas (Jiang and Doyle, 2008, and Zhong et. al, 2008), the Rocky Mountains (Miller et. al, 1974) and the Andes (Seluchi et. al, 2003 and Norte, 1988). The more recent study of Smith and Skillingstad (2010), presented herein, shows a preferential time of onset and decay of downslope windstorms over the Falklands Islands using the data set of Mobbs et. al (2005). Unlike the previous mentioned studies, the forcing mechanism for this case cannot be attributed a multiscale process involving a mixing of the cold valley pool in the lee a ridge, since topography on the East Falkland Island is characterized by a single ridge.

A few modeling studies have attempted to address the influence of surface heating on lee flow regimes. Doyle and Durran (2002), showed that even relatively weak surface heating can result in significantly reduced rotor strength, increased rotor height, and increase in near surface TKE for trapped lee wave rotors. Jiang et. al (2006) and Smith et. al (2006) showed that the absorption of wave energy by the boundary layer in the lee of the ridge can be increased by stagnant near surface layers and that stable boundary layers are more efficient in absorbing trapped lee waves than turbulent neutrally stratified boundary layers. Both of these studies focused on the nonhydrostatic trapped lee wave

regime. Poulos et. al (2000), in a study of katabatic flow interaction with mountain waves, showed that in some cases mountain waves were not strong enough to inhibit the usual morning and evening transitions generally seen in slope flows, while in other cases the mountain wave response was strong enough to scour out the katabatic flow entirely. Ying and Baopu (1993) attribute the primary mode of influence of surface heat fluxes on downslope windstorms over a low ridge to changing boundary layer stability and a modulation of wind speed at the top of the boundary layer. As these studies have all focused on the trapped lee wave regime or the IGW breaking regime little is known about the extent to which diurnal heat fluxes may affect downslope windstorms induced by interfacial wave physics or mountain wave induced instabilities on an inversion.

**Investigation of upstream boundary layer influence on mountain wave breaking and
lee wave rotors using a large eddy simulation**

Craig M. Smith and Eric D. Skillingstad

College of Oceanic and Atmospheric Sciences

104 COAS Admin Bldg

Oregon State University, Corvallis, OR 97331-5503, USA

Journal of Atmospheric Sciences

Volume 66, 2009, p. 3147-3164.

Abstract

Interactions between a turbulent boundary layer and nonlinear mountain waves are explored using a large-eddy simulation model. Simulations of a self-induced critical layer are considered, which develop a stagnation layer and a strong lee-side surface jet. Over time, wave breaking in the stagnation region forces strong turbulence that influences the formation and structure of downstream lee side rotors. Shear production is an important source of turbulence in the stagnation zone and along the interface between the stagnation zone and surface jet, as well as along the rotor edges. Buoyancy perturbations act as a source of turbulence in the stagnation zone, but are shown to inhibit turbulence generation on the edges of the stagnation zone.

Surface heating is shown to have a strong influence on the strength of downslope winds and the formation of lee side rotors. In cases with no heating, a series of rotor circulations develop, capped by a region of increased winds. Weak heating disrupts this system and limits rotor formation at the base of the downslope jet. Strong heating has a much larger impact through a deepening of the upstream boundary layer and an overall decrease in the downslope winds. Rotors in this case are nonexistent. In contrast to the cases with surface warming, negative surface fluxes generate stronger downslope winds and intensified rotors due to turbulent interactions with an elevated stratified jet capping the rotors. Overall, the results suggest that for nonlinear wave systems over mountains higher than the boundary layer, strong downslope winds and rotors are favored in late afternoon and evening when surface cooling enhances the stability of the low level air.

2.1 Introduction

Downslope windstorms and associated rotor events are very important in determining aviation hazards in the lee of major mountain ranges. Turbulence generated by mountain wave breaking and rotor dynamics can create severe conditions for aircraft operations. The onset and decay of such events are frequently tied to synoptic-scale processes in the atmosphere, such as the passage of a front over a mountain range, however, downslope windstorms can also occur on days with little change in synoptic conditions. In the absence of strong synoptic forcing, boundary layer processes may affect the strength and duration of downslope wind storm and rotor events, and may explain observations suggesting preferred times for wind storm and rotor formation. The topic of this paper centers on understanding the formation and dynamics of turbulence generated by downslope wind storms and lee-side rotors. In particular, we focus on the influence of boundary layer turbulence on mountain wave and rotor formation, and on the generation and interaction of turbulence forced by mountain wave breaking.

Although synoptic scale features which aid in forecasting strong downslope winds have been studied by a number of researchers (Colle and Mass 1998a and 1998b; Brinkmann, 1974; Czyzyk and Runk, 2006), there have been few observational studies that have focused on the influence of the upstream boundary layer stability and depth on mountain waves. Recent observations from the Terrain-Induced Rotor Experiment (T-REX) field campaign (Grubisic and Kuettner, 2003), suggest a tendency for downslope windstorms to occur preferentially in the late afternoon and early evening (Grubisic and Xiao, 2006) in the lee of the Sierra Nevada mountains. Observations from Argentina reported in Seluchi et al. (2003) and Norte (1988) also show an increased frequency of downslope windstorms in the afternoon. These results are suggestive of a dynamical effect of the boundary layer depth and stratification on lee flow regimes, however studies in other regions show a propensity for downslope windstorms to occur at times other than late afternoon. For example, Brinkmann (1974) found that the most likely time of day for downslope windstorms to occur in Boulder, Colorado was roughly between midnight and 7 AM in the morning during the winter months.

Due to the difficulty of observing localized and transient mesoscale atmospheric events, there have been few direct observations of mountain wave breaking and associated turbulence. The scarcity of observations has been cited as a major reason why mountain wave breaking events are still so poorly understood (Doyle et al., 2005). One prominent and well-studied case is the 11 January 1972 windstorm along the Front Range of the Rockies (Lilly and Zipser, 1972; Lilly, 1978). The dynamics of this case have been examined in a number of modeling experiments (Clark and Peltier, 1977; Clark and Peltier, 1984; Durran, 1986). Other important observations of mountain wave breaking events include those over Greenland (Doyle et al., 2005), documentation of clear air turbulence over the Front Range of the Rockies (Clark et al., 2000), the Alps (Jiang and Doyle, 2004), rotor generation over the Falkland Islands (Mobbs et al., 2005), and the importance of upstream inversions and internal gravity wave breaking to the bora (Glasnovic and Jurcec 1990, Klemp and Durran 1987, Gohm and Mayor 2005, Belusic et al. 2007, Klemp et al. 1997, Gohm et al. 2008).

As with observational studies, very few mountain wave modeling experiments have focused on turbulence and upstream boundary layer stability controls on lee flow regimes. In a modeling study of the diurnal variation of lee wave regimes, Ying and Baopu (1993) point out that classical mountain flow theory does not account for the thermal stratification of the atmospheric boundary layer. They examine the effects of boundary layer stability on flow blocking, mountain wave amplitudes and lee slope jet speeds. Other researchers have also found that boundary layers tend to reduce the amplitude of mountain waves and in some cases can inhibit internal gravity wave breaking (Olafsson and Bougeault, 1997). Richard et al. (1989) note that the inclusion of a boundary layer in their numerical experiments leads to shooting flows that, compared with experiments without a boundary layer, have a spatial extent that is significantly reduced on the lee slope. Peng and Thompson (2003) extend the analysis to the case of narrow mountains where internal gravity wave amplitude may be increased by the presence of a boundary layer. They suggest that the boundary layer height plus the terrain height acts as an effective terrain barrier that determines the lower boundary condition for wave launching.

Vosper (2004) examined the importance of sharp upwind temperature inversions on flow over mountains and the role of surface friction in the formation of rotors. Lee slope flow regimes were found to be sensitive to inversion strengths and heights, which were for the most part greater than the hill height. While physically relevant for small hills and the Falkland Islands, this situation is generally not representative of realistic conditions near major mountain ranges such as the Front Range in Colorado and the Sierra Nevadas in California.

Doyle and Durran (2002) examine the effect of lee slope heating on the structure and development of rotors associated with resonant mountain waves using numerical simulations. They demonstrate that the inclusion of surface friction is a requirement of modeling realistic rotors and increasing the surface heat flux downstream from the mountain crest increases the vertical extent of the rotor circulation and the strength of the turbulence, but decreases the magnitude of the reversed rotor flow. Studies such as Jiang et al. (2006) and Smith et al. (2006) examine the absorption of trapped lee waves by the atmospheric boundary layer downstream from a ridge. They show that the decay of lee waves is sensitive to surface roughness and heat flux, and that the stable nocturnal boundary layer is more efficient in absorbing trapped waves than a turbulent convective boundary layer.

Other contributions have concentrated on the dynamics and energetics of mountain wave breaking. Afanasyev and Peltier (1998), using a direct numerical simulation (DNS) emphasized the inherent three-dimensional nature of internal gravity wave breaking and role of Kelvin-Helmholtz (K-H) billows above the downslope jet along the lee side of a simulated obstacle. Gheusi et al. (2000) performed a similar modeling study representing a laboratory tank experiment, examining the formation of three-dimensional vortical disturbances generated in the wake breaking region. They emphasized the production of turbulent kinetic energy (TKE) by shear at the bottom of the mixed layer. A series of papers (Laprise and Peltier, 1989a; Laprise and Peltier, 1989b; Laprise and Peltier, 1989c) concerning the energetics and stability of breaking mountain waves developed a conceptual framework for the transition of a mountain wave lee flow regime to that of a self induced critical layer and the dominance of a resonant mode producing shooting flow along the lee slope. As noted by the authors, these experiments were performed without

the benefit of a turbulence closure scheme. Addressing this issue, Epifanio and Qian (2008) used a large-eddy simulation (LES) to analyze the momentum and turbulence budgets for a breaking mountain wave and found that the mean wave energy dissipation was mostly due to turbulent momentum fluxes, which act counter to the mean flow disturbance wind.

In the majority of mountain wave modeling studies, upstream conditions are prescribed and typically do not consider how the stability and turbulence in the upstream boundary layer affect mountain wave systems. The focus of this paper is on the role of the upstream boundary layer and surface heating in controlling the strength of mountain-induced internal waves, low-level internal gravity wave breaking, and downslope windstorms and rotors. We define rotors as a low-level circulation in the lee of a ridge, about an axis parallel to the ridge (Glickmann, 2000). In this sense, the existence of negative streamwise surface velocities in the lee of the ridge is not a requirement of the existence a rotor. We concentrate on the effect of turbulence on lee flow response by applying a large eddy simulation (LES) model designed to directly simulate turbulent eddies that control the boundary layer dynamics as well as eddies forced by mountain wave breaking. Application of LES also allows us to simulate the turbulent boundary layer with arguably more fidelity than models with parameterized turbulence closure (e.g. Mellor and Yamada type closures) because a portion of the energy-carrying turbulent eddies are resolved in the model, whereas most other simulations completely parameterize turbulent fluxes.

One other prominent modeling study (Epifanio and Qian, 2008) that has used the LES approach for lee flow regimes focused on the dynamics of internal gravity wave breaking generated by a self-induced critical layer, and orographic generation of potential vorticity. We consider a scenario very similar to their simulations, except that we use a different surface boundary condition (limited-slip in ours versus free-slip in theirs), simulate a well-developed upstream boundary layer, apply a higher model resolution (10 m in our simulation versus 180 m in theirs), and focus more on downstream rotors.

The paper is structured as follows. A description of the LES model is presented in Section 2 along with an outline of the experiments performed in our study. Results are presented next in Section 3 for a basic experiment that includes no surface heating. Next

we compare the basic no heating simulation to simulations that include weak surface heating, strong surface heating, and surface cooling. Then, we further explore the effects of both upstream and downstream heating in the weak heating case. Summary and conclusions are given in Section 4.

2.2 Model Introduction and Setup

Experiments were performed using a modified version of the LES model described in Skyllingstad (2003) and used in Smith and Skyllingstad (2005). This model is based on the Deardorff (1980) equation set, with the subgrid-scale model described by Ducros et al. (1996). Pressure in the model is calculated using the anelastic approximation with a conjugate residual iterative pressure solver (Smolarkiewicz and Margolin 1994). Terrain in the LES model is prescribed using a shaved cell approach described in Adcroft et al. (1997) and Steppeler et al. (2002). This approach was selected over the more commonly used terrain following coordinate methods to avoid problems with the LES filtering assumptions. Comparisons between mountain waves simulated using terrain-following coordinates and the shaved cell approach show only minor differences (Skyllingstad and Wijesekera, 2004). Further tests, which are not shown, confirm that simulations using this model compare quite well with previously reported results (Steppeler et al., 2002, figures 2 and 3).

Simulations were conducted using a narrow channel domain with periodic boundaries in the cross slope direction, an Orlanski (1976) type boundary condition at the outflow boundary, and a recirculating upstream boundary (figure 2.1). For the upwind boundary, the recirculating scheme was developed following Mayor et al. (2002) and provides a method for generating a fully developed boundary layer upstream from the mountain. The scheme was implemented by treating a portion of the domain as a periodic sub-domain, and then using the velocity and scalar fields as boundary values on the upstream edge of the open boundary channel. The length of the periodic sub-domain (from $y = 0$ km to $y \approx 1$ km, where y is in the streamwise direction), was chosen to be large enough so that there were no signatures of the sub-domain length in the eddy structures in the boundary layer.

A limited-slip lower boundary for some of the simulations was set by assuming a neutral log scaling and setting the subgrid momentum flux to

$$\langle v''w'' \rangle = -C_D v^2 \quad (1)$$

$$C_D = \left[\frac{\kappa}{\ln(\delta z/z_o)} \right]^2 \quad (2)$$

with a surface roughness, $z_o = 0.01$ m, where $\langle v''w'' \rangle$ is the average subgrid scale momentum flux, C_D is the drag coefficient, v is the velocity in the streamwise direction, w is the velocity in the vertical direction, $\kappa = 0.4$ is the von Karman constant, and $\delta z = \Delta z/2$ is half of the vertical grid spacing. The turbulent viscosity, K_m , is specified in the lowest grid cell only following similarity theory for neutrally stable boundary layers

$$K_m = u_* z \kappa \quad (3)$$

where u_* is the friction velocity defined in the usual manner. The top boundary condition included a sponge layer following Durran and Klemp (1983) with a depth of 2500 m, which was greater than the wavelength of the dominant waves generated by the mountain in our model. We chose the sponge layer depth to eliminate significant energy reflection off of the upper boundary and sponge layer. Mass conservation in the model was ensured by calculating the difference between the mean outflow momentum flux on the downstream boundary and the prescribed inflow momentum flux, and then setting the model-top vertical velocity to maintain constant mass.

A two-dimensional ridge obstructing the flow was based on the Witch of Agnesi profile (4)

$$h(y,z) = \frac{h a^2}{y^2 + a^2} \quad (4)$$

for a mountain of height, $h = 400$ m, and width, $a = 4000$ m. The non-dimensional mountain height, $Nh/v = 1.2$, and non-dimensional mountain width, $Na/v = 12$, were calculated using the prescribed inflow conditions in the free atmosphere above the surface boundary layer where N is the Brunt-Vaisala frequency,

$$N = \sqrt{\frac{g}{\theta} \frac{\partial \theta}{\partial z}}, \quad (5)$$

g is the acceleration due to gravity, and θ is the potential temperature.

An idealized initial state is prescribed with constant streamwise velocity, v , set to 5 m s^{-1} and $N = 0.015 \text{ s}^{-1}$. Both are constant with height in contrast to previous modeling studies, which have generally used a trapping mechanism of decreasing N with height or increasing U with height (Doyle and Doyle, 2002; Hertenstein and Kuettner, 2005) to generate rotors. In this study we instead use a wave breaking mechanism in which a self-induced critical layer acts as a reflector of wave energy in order to generate rotors. Although computational issues restrict us to modeling flow over a ridge that is small in comparison to the Sierra Nevada or the Rocky mountains, our ridge height is comparable to the rotor inducing terrain on the Falkland Islands (Mobbs et al., 2005). Moreover, dynamical similarity, based on non-dimensional mountain height and non-dimensional width, can be used for comparisons. Domain size was set to $100 \times 4560 \times 300$ grid points in the along slope, cross slope, and vertical directions respectively, with grid resolution of 10 m in all directions below 1.5 km. Above 1.5 km, the vertical grid spacing stretches from 10 m to 80m. The total domain size was $1.0 \text{ km} \times 45.6 \text{ km} \times 9.8 \text{ km}$. The mountain was centered at $y = 27 \text{ km}$, slightly past the center point in the streamwise direction.

Surface heating was applied throughout the entire domain unless otherwise indicated. The surface heating characteristics and names of the simulations are summarized in Table 2.1. In all simulations, surface heating of 25 W m^{-2} was applied for the first 20 minutes to initiate boundary layer turbulence. Heat fluxes for the weak and strong heating runs were set to 25 W m^{-2} and 200 W m^{-2} respectively and held constant after the initial 20 minutes. In the surface cooling run, a surface heat flux of -50 W m^{-2} was applied after a 1 hour spin up period. All of the cases began with a neutrally stratified boundary layer height, z_i , of 200 m.

2.3 Results

No heating run

We first present results from the no heating case, which provides a baseline for assessing the effects of surface fluxes. Cross-section plots of streamwise velocity, vertical velocity, and average resolved eddy TKE overlaid with contours of potential temperature are presented in figure 2.2 for three different times. In this and subsequent

plots we have chosen to present results at dynamically important times in the flow evolution. After 3 hours of integration, in all cases the flow has reached a quasi-steady state. All variables presented in the plots are instantaneous at a single cross section in the model domain unless otherwise specified as being averaged. For the purposes of this study we define the average of a variable ϕ as follows.

$$\bar{\phi}(y,z) = \frac{1}{i_{\max} \cdot n_{\max}} \sum_{n=1}^{n_{\max}} \sum_{i=1}^{i_{\max}} \phi(x,y,z) \quad (6)$$

where the overbar denotes average. In this equation i_{\max} is the number of points in the spanwise direction and n_{\max} is the number of time steps over the 5 minute averaging time.

The spanwise mean

$$\phi_{spanwise\ mean}(y,z) = \frac{1}{i_{\max}} \sum_{i=1}^{i_{\max}} \phi(x,y,z) \quad (7)$$

is used to calculate perturbations about the spanwise mean

$$\phi'(x,y,z) = \phi(x,y,z) - \phi_{spanwise\ mean}(y,z) \quad (8)$$

In figure 2.2c we present average resolved eddy TKE, where resolved eddy TKE is defined as

$$e' = \frac{1}{2} (u'^2 + v'^2 + w'^2), \quad (9)$$

the perturbation velocities are calculated as in (7) and (8), and the averaging is done in the spanwise direction as well as temporally as in (6). Computing averages in this way removes the large-scale internal waves generated by the mountains, however smaller scale waves are still treated as ‘‘turbulence.’’ Nevertheless, this method yields turbulence fields that are consistent with buoyant and shear production of turbulence as shown below.

Figure 2.2 spans the time period when a self-induced critical level at ~ 1 km becomes buoyantly unstable and generates a breaking wave with considerable turbulence. The first time is at $t = 180$ min, which is just before the breaking event begins. Streamwise velocity at this time shows a typical nonlinear amplified gravity wave response with a large zone of stagnant air with near zero streamwise velocity over the lee of the mountain between 1 and 1.5 km height. Beneath this stagnant layer is a jet of increased winds along the surface of the lee of the mountain. The surface jet extends

down the slope until boundary layer separation occurs at $y = \sim 34$ km and the jet is lofted into the air by the first of a series of rotors, which are in the initial stage of formation. Turbulence at $t = 180$ min is generally limited to the boundary layer beneath the evolving rotor circulation.

At 205 min the isotherms in the stagnation zone (near $y = 30$ km) begin to overturn indicating the onset of internal gravity wave breaking. As the isotherms overturn, wave breaking generates strong vertical motion and increased turbulence aloft. Over time, turbulence generated aloft is advected throughout the stagnation zone and over the rotor system. Vertical velocities associated with the rotors nearest the mountain are intensified during the breaking process and the rotor heights increase. The rotors also propagate upstream with the first rotor moving from $y = 34$ km at 180 min to $y = \sim 32$ km at $t = 235$ min. Negative streamwise velocities associated with the rotor nearest the mountain are quickly destroyed by transport and mixing in the breaking stagnation zone. Rotors further downstream, which have not yet interacted with the turbulence advected downstream from the breaking wave region, are shorter, less turbulent and still contain negative streamwise velocities at the surface.

Factors controlling TKE in the simulations can be diagnosed using the TKE budget equation,

$$\frac{\partial e}{\partial t} = \underbrace{-U_j \frac{\partial e}{\partial x_j}}_{\text{I}} + \underbrace{\delta_{i3} \frac{g}{\theta_0} \overline{u'_i \theta'_i}}_{\text{III}} - \underbrace{\overline{u'_i u'_j}}_{\text{IV}} \frac{\partial U_i}{\partial x_j} - \underbrace{\frac{\partial (\overline{u'_j e})}{\partial x_j}}_{\text{V}} - \underbrace{\frac{1}{\rho} \frac{\partial (\overline{u'_i p'})}{\partial x_i}}_{\text{VI}} - \underbrace{\varepsilon}_{\text{VII}}, \quad (10)$$

where U_j represent the spanwise average velocity components, ε is the dissipation of turbulence, ρ is the density, p' is the perturbation pressure, and over bars represent a spanwise average. Terms in (10) are defined as TKE storage (I), horizontal advection (II), buoyant production/destruction (III), shear production (IV), turbulent transport (V), pressure transport (VI), and dissipation (VII).

Formation of TKE in the mountain wave system is dominated by the combined action of the buoyancy and shear production terms as presented in figure 2.3 along with contours of potential temperature. At the onset of wave breaking aloft (at $t = 215$ min) buoyant perturbations associated with the overturning of stable isotherms and shear

production act to generate turbulence in the stagnation zone. Buoyant suppression on the edges of the stagnation zone is offset by shear production of TKE between the surface and 0.5 km. Shear production in the lower layer is associated with vertical gradients of streamwise velocity at the top of the surface jet, which can clearly be seen in the velocity field (figure 2.2). Concentrated TKE in the first rotor at 215 min is associated with both buoyant production and shear production of TKE in the rotor updraft region. Eventually, TKE from this updraft source region is advected throughout the rotor system. These results are in general agreement with Epifanio and Qian's (2008) and Gheusi et al. (2000), which show that shear production from the top of the surface jet is the dominant source of TKE, and that buoyant production is much less important than shear production of TKE.

Vertical gradients of streamwise velocity above the stagnation layer decrease much faster than they do below the stagnation layer. Consequently, by 235 minutes the shear production at the top of the stagnation zone is significantly less than it is at the interface of the stagnation zone and the surface jet. Some of shear production at the top of the stagnation zone might be due to the elevated jet near 2 km (fig 2.2). The existence of this elevated jet is thought to be at least partially due to the leakage of some portion of wave energy through the stagnation zone. Although the secondary breaking zone might be strictly a numerical artifact of an upstream velocity profile that does not change with height, observational evidence provides little insight into the existence of secondary wave breaking regions.

Shear and buoyant production at 235 minutes continue to play dominant roles throughout the slope flow and rotor system, and turbulence generated in the stagnation zone has largely advected downstream above the trapped lee wave system. Animations of this simulation reveal that most of the TKE within the rotors is generated locally, especially along the rotors updrafts, and not advected into the rotors from the stagnation zone.

Influence of surface heat fluxes

In this section we compare results from cases where surface heat flux has been applied to the models. These simulations were designed to examine the effects of weak surface heating (25 Wm^{-2}), strong surface heating (200 Wm^{-2}) and surface cooling (50

Wm^{-2}) on downslope winds and rotor formation. A list of all experiments and their abbreviated names can be found in Table 3.1. For the weak and strong heating cases, fluxes are applied for the entire period of model simulation. In the surface cooling case, a positive surface flux of 25 Wm^{-2} is applied for the first hour of simulation time to generate a well-mixed upstream boundary layer. This is followed by surface cooling of 50 Wm^{-2} , simulating the transition from afternoon to evening in the upstream boundary layer.

Upstream profiles of velocity, potential temperature and TKE are presented in figure 2.4 for each case after 200 minutes, demonstrating the effects of the heat flux on the boundary layer structure. We note that the cooling case generates a weakly stratified, shallow boundary layer that is not well resolved by the model. Our intent in simulating this case was to examine how reduced surface turbulence and increased low-level stratification affects the mountain wave response.

In figure 2.5 we present streamwise velocities, vertical velocities, and averaged TKE and contours of potential temperature for the no heating, weak heating, strong heating, and cooling cases, respectively, at $t = 220 \text{ min}$. Compared with the no heating case, weak heating produces small differences in the downstream lee wave structure with a reduction in lee wave strength beyond the first rotor, and the absence of negative streamwise velocities under all lee waves. The absence of negative streamwise velocities beneath the lee waves means that rotors are not present at all in the weak heating case. However, the strength of the downslope jet is roughly the same in these two cases. In contrast, both the lee wave structure and downslope jet in the strong heating case are nonexistent relative to the weak heating and no heating cases. Surface flow reversal in this case is much less prevalent than it is in the no heating case. In addition to differences in the lee wave structure, the lee side surface jet is significantly shorter and higher in the strong heating case. Stratification in the lowest 0.5 km above the ground is essentially unstable, which leads to a much more diffuse surface jet. The stagnation zone is also smaller in the strong heating case, with most of the boundary layer turbulence resulting from convective forcing rather than turbulence from mountain wave breaking.

In contrast to the heating cases, the surface cooling case shows a series of well-developed and distinct lee wave rotors. The first rotor begins slightly upslope from the

location of the first rotor in the no heating case ($y = 32$ km versus $y = 33$ km), a result which is consistent with the numerical experiments of Poulos et al. (2002). Unlike the no heating case, each rotor is capped by a stably stratified, undulating jet with relatively high velocities. Negative streamwise velocities under each rotor crest are more pronounced in the cooling case than in the other simulations. In comparison with the no heating case, rotor wavelengths in the cooling case are shorter (~ 1.9 km versus ~ 2.5 km). This result is consistent with Jiang et al. (2006) who find that surface cooling results in shorter wavelengths for trapped lee waves. An additional simulation, not shown here, run with surface cooling but no mean streamwise flow velocity, develops a katabatic flow of small magnitude (roughly 2 ms^{-1}) over the slope, less than ~ 50 m in depth, which is significantly less than the depth of the shooting flow on the lee slope. Due to the small height and width of our mountain we found katabatic flow velocities on the lee slope to be significantly less than previous researchers who have studied the interaction of katabatic flow and mountain waves (Poulos et al., 2000). The increased near surface stratification, as shown below, does however play a dynamically significant part in the structure of the lee rotors.

Plots of TKE for the no surface heating, weak surface heating, strong surface heating, and surface cooling cases are also presented in figure 2.5. Both the weak and no heating cases show very little difference in the stagnant flow region above the lee side jet. Surface heating is not strong enough in the weak heating case to affect the stratification of the stagnation zone, which begins over $\frac{1}{2}$ km above ground level on the lee slope. However, turbulence in the boundary layer is significantly different between the two cases. In the no heating case, turbulence in the rotors and boundary layer is confined to the lee of the mountain, whereas turbulence is located upstream of the mountain and throughout the entire flow downstream of the mountain in the weak heating case. Indeed, some of the upstream boundary layer turbulence is advected over the mountain and into the rotors themselves (although as shown below, turbulence transport for the weak heating case is not the dominate factor inhibiting rotors). Increased boundary layer turbulence is one reason why the rotor circulations downstream of the mountain are more diffuse and weaker in the weak heating case.

Boundary layer turbulence plays a very prominent role in the dynamics of the strong surface heating case. Here, convection located both upstream and downstream of the mountain generates strong turbulence that is transported over the mountain. The well-mixed upstream turbulent boundary layer is approximately twice the height of the mountain in this case (see figure 2.4). Increased turbulence in the boundary layer weakens the surface jet, decreasing the amount of shear-produced turbulence at the bottom of the stagnation zone and top of the surface jet. Both the stagnation zone and dispersive waves play a significantly smaller role in the strong heating case.

For the surface cooling case, the dynamics of the stagnation zone and associated internal gravity wave breaking are similar to the no heating case. However, surface cooling enhances the strength of near-surface stratification upstream from the mountain. Increased surface stratification leads to a strengthening of the potential temperature gradient at the top of the rotor zone, and an extension of the lee side jet over the rotors further downstream in comparison with the no heating case. Increased streamwise velocities associated with the lee side jet and flow over the rotors fuels increased TKE through shear production. In the no heating case, the largest concentrations of TKE in the boundary layer decrease rapidly as a function of downstream distance.

Contour plots of TKE budgets for the no heating, strong heating, and cooling cases at $t = 220$ (figure 2.6) show significantly less shear production of TKE aloft in the strong heating case. As noted before, TKE from the surface acts to diffuse and weaken the surface jet, which is the primary source of shear-produced TKE in the lower stagnation zone. Consequently shear production in the strong heating case is spread over a larger area in comparison with the no heating and cooling cases. Convection in the strong heating case generates a deep mixed layer upstream from the mountain, which effectively prevents a strong mountain internal wave response.

In the surface cooling case, shear production of TKE is significant along the rotor interfaces, especially further downslope from the ridge, because of the undulating jet discussed above. Buoyant production of TKE in the rotor updrafts is also a source of TKE, but not as dominant as shear production. The maintenance of the strongly stratified undulating jet above the rotors is largely due to buoyant suppression of TKE along the crest of the rotors and in the rotor downdrafts. This is also important in maintaining the

rotor circulation by preventing turbulence advected from the stagnation zone from destroying the stratified layer that defines the top of the rotors. The increased amount of shear production along the bottom of the especially strong and distinct stably stratified undulating jet also generates more turbulence within the rotors themselves. In contrast, convective mixing in the strong heating case prevents the formation of the stratified layer and accompanying rotors.

Upstream versus downstream weak surface heating

Overall, our results suggest that boundary layer turbulence can have a dramatic impact on the strength of lee side winds and trapped waves. However, it is not clear if turbulence generated locally by convection is more or less important than turbulence generated upstream from mountains and transported downstream by the mean flow in cases with weak heating. We next explore the effects of upstream versus downstream heating by conducting experiments where weak surface heating (25 Wm^{-2}) is applied either upstream of the ridge crest only, or downstream of the ridge crest only. A separate set of simulations, not shown here, run with no mean streamwise flow velocity and surface heating on half of the domain only, show a surface horizontal flow speed of less than 1 ms^{-1} . Thus the mean flow in the simulations presented dominates the horizontal flow that results from the differential heating of the surface.

In figure 2.7 we present streamwise velocities, vertical velocities, and averaged TKE and contours of potential temperature for the upstream heating and downstream heating cases at $t = 230 \text{ min}$. Although there is a significant amount of TKE transported over the ridge in the upstream heating case, the downstream heating case has more turbulence in the boundary layer in the lee of the ridge. The rotors in the upstream heating case are fairly well defined, while the rotors in the downstream heating case are not as distinct. The downstream heating case shows a lee wave train in which there are virtually no negative streamwise velocities. In contrast, the upstream heating case bears a strong resemblance to the no heating case (figure 2.5), except that the rotors in the upstream heating case are slightly taller (as in Doyle and Durran, 2002), and the streamwise wavelength is smaller.

Turbulence aloft and at the surface jet/stagnation zone interface is stronger in the downstream heating case in comparison with the upstream heating case. This is largely due to an increase in the shear production of TKE (see figure 2.8, contour plots of the TKE budget terms). Transport of TKE over the mountain in the upstream heating case is not as important as locally generated TKE in the downstream heating case. Most of the TKE within the rotors in the upstream heating case is generated by shear production in the rotors themselves, and at the foot of the surface jet where the rotors begin. In the downstream heating case, shear production of TKE is more vigorous at the interface of the surface jet and stagnation zone and continues to a lower height than in the upstream heating case, allowing for more efficient entrainment of TKE from the foot of the jet into the rotors (near $y = 33$ km). The increased shear production of TKE results in weaker and more diffuse lee wave rotors in the downstream heating case. Hence surface heating affects the rotor and lee wave structure indirectly through increased shear production of TKE, rather than through direct buoyant production of TKE.

Further insight into the role of upstream versus downstream heat fluxes is presented in figure 2.9, which shows the streamwise flux of integrated turbulence as a function of downstream distance at $t = 195$ min, just after the onset of wave breaking aloft. Integrated turbulence flux is defined as a vertical integral of the product of streamwise velocity, v , with turbulence, e ,

$$\overline{ve} = \int v e dz. \quad (11)$$

where the integral is taken over the entire domain. We concentrate on locations with $y < 30$ km and $y > 40$ km, since these do not include the direct effects of wave breaking aloft. Integrated turbulence flux values in the weak heating case upstream of the mountain are almost exactly the same as those of the upstream heating case, while both the no heating case and the downstream heating case show almost no integrated turbulent flux upstream of the mountain. However, in the lee of the mountain and behind the area affected by the stagnation zone breaking ($y > 40$ km) the integrated turbulence flux in the upstream heating case is very small, while the integrated turbulence flux in the downstream heating case is roughly the same as the weak heating case. This points to the role of indigenously generated turbulence in the lee of the mountain as a controlling factor in the formation of rotors. In the case of weak surface heating, where the flux of turbulence from the

upstream boundary layer does not completely dominate the dynamics of the lee flow, surface heating downstream of the ridge crest plays a more important role in determining lee flow dynamics than does surface heating upstream of the ridge crest. For larger upstream surface heating (and higher boundary layer heights relative to mountain heights), the effect of upstream surface heating on lee rotors is much more pronounced, as shown by the strong heating case. Nevertheless, even weak heating on the lee side of the mountain is able to increase low-level turbulence and prevent strong rotor formation.

Rotor Structure

Throughout our analysis we emphasize the significant role of turbulence in controlling the number and strength of trapped waves and rotors in the simulations. For the large-scale structure of rotors, our results are in many ways similar to past studies showing a range of rotor behavior dependent on boundary layer heating and surface roughness. However, our results do not show the organized structures noted in the previous high-resolution rotor study of Doyle and Durran (2007). In their study, small-scale circulations or subrotors are produced along the upstream edge of the rotor and propagate through the rotor circulation. They attribute these subrotors to K-H waves that are triggered by the flow separation at the leading edge of the rotor and amplify at the expense of shear. For comparison, we present plots of spanwise vorticity similar to Doyle and Durran (2007) for the leading rotor in the no heating case (figure 2.10). Spanwise vorticity is defined as

$$\eta_{spanwise} = \frac{\partial v}{\partial z} - \frac{\partial w}{\partial y} \quad (12)$$

In contrast to their results, our simulations do not show strongly organized subrotors along the edge of the main circulation, but display a more chaotic vorticity field indicative of fully turbulent flow. The flow in the simulations of Doyle and Durran (2007), in which turbulent motions of all length scales are explicitly accounted for by the TKE parameterization, does not contain vorticity perturbations as are apparent in figure 2.10 along the slope of the ridge. We speculate that grid resolution or subgrid scale TKE parameterization issues may play a role in this. Small-scale turbulence in our simulations is the likely reason that K-H billows are not generated in the shear layer above the rotor. Resolved turbulence prevents K-H billow formation by disrupting the smooth shear flow

upstream from the rotor, preventing the more gradual growth of well organized instability waves noted in Doyle and Durran (2007).

2.4 Conclusions

The focus of this study was twofold: to examine low-level internal gravity wave breaking and its interaction with lee wave rotors using an eddy resolving model, and to examine the interaction of an upstream boundary layer modified by surface heat fluxes on downslope winds and rotors.

Our experiments were based on a simple scenario with constant velocity and stratification, a mountain height selected to generate low-level internal wave breaking, and an upstream boundary layer $\frac{1}{2}$ the height of the mountain. Simulations with various heat fluxes were conducted and analyzed to understand how rotors interact with internal wave breaking and turbulence. In the case with no surface heating, a typical nonlinear wave response was produced, with a lee side surface jet and a large zone of stagnant air above the lee side of the mountain that eventually resulted in overturning of isotherms and generation of turbulence. Turbulence was also generated by shear production along the edges of the stagnation zone, especially at the interface with the surface jet on the lee of the slope. Over time, a series of trapped waves or rotors formed in the lee of the ridge, with the first rotor representing the separation of the lee side jet from the mountain slope. Downstream rotors maintain a distinct identity as they slowly propagate back towards the ridge. Once sufficiently close to the ridge, the lead rotor decayed because of interaction with turbulence advected from wave breaking region and turbulence generated indigenously in the rotor zone by gradients in vertical and horizontal velocity.

Increasing surface flux was found to alter the strength and number of rotors. With weak heating of 25 W m^{-2} , there were no longer any negative streamwise velocities under the lee waves, which were strongly modified by turbulence generated in the stagnant, wave-breaking region and through convective forcing. However, lee-side downslope winds in this case were not strongly affected by turbulence. Strong surface heating of 200 W m^{-2} prevented the formation of rotors and produced a much weaker downslope wind event. In this case, the boundary layer depth increased rapidly to a depth roughly

double the mountain height, thereby reducing the stratification of flow forced over the mountain. Simulations with heating confined to either the upstream or downstream side of the mountain (similar to the Doyle and Durran 2002 study) revealed that locally generated turbulence on the downstream side of the mountain was much more important in controlling the rotor behavior than turbulence advected over the mountain from the upstream boundary layer.

In contrast with the surface heating cases, surface cooling of 50 W m^{-2} forced an enhanced rotor circulation, leading to a train of lee side waves capped by a jet of increased streamwise winds. Increased stratification from surface cooling was found to be important in the formation of a stably stratified undulating jet, which capped the rotors. Shear between this jet and the rotors generated increased turbulence in the rotors themselves, while buoyant destruction of TKE in the rotor downdrafts acted to maintain the rotor circulations for a longer distance downstream from the ridge.

In general, there are three relevant physical cases, in terms of the ratio of upstream boundary height to ridge crest height, presented in our experiments. When upstream boundary layer height is much less than ridge crest height, upstream surface heat fluxes are largely irrelevant for the downstream flow because upstream turbulence is not advected over the ridge. When upstream boundary layer height is much greater than ridge crest height, upstream turbulence is advected over the ridge crest and can dominate lee flow behavior. Finally, in the case where upstream boundary layer height is comparable to ridge crest height, both upstream turbulence and surface heat fluxes can affect the lee flow behavior, depending on the strength of surface heat fluxes. For these cases, our simulations suggest that well-developed lee wave trains will be favored at night and in the early morning, and will generally become indistinct or washed out on days with strong surface heating.

Our simulations, for the most part, represent conditions that have not been examined in past modeling studies of lee wave systems and rotors. For example, Doyle and Durran (2007) examined rotors and small-scale subrotor circulations for environmental conditions without the low-level internal gravity wave breaking and turbulence generated by a self-induced critical level. They used a sounding which included a low level inversion and velocity which increased with height, which prevented

the low level internal gravity wave breaking which is so dominant in our simulations. In their simulations, rotors were found to produce well-defined Kelvin-Helmholtz billows. Rotors in our study did not produce the same structures, but instead were characterized by chaotic eddies more indicative of fully turbulent flow. Differences between our simulations and Doyle and Durran (2007) might be explained by different upstream soundings, presence or absence of internal gravity wave breaking, differences in grid resolution in our simulations (by roughly a factor 3), the presence of upstream turbulent eddies, and differing subgrid parameterization of turbulence.

Epifanio and Qian (2008) also used an eddy-resolving model to examine how turbulence affects internal wave breaking for a self-induced critical level, but without considering upstream boundary layer effects or rotor formation. In general, our analysis of turbulence formation in the stagnant region compares favorably with their results. However, our simulations suggest a more prominent role for shear production of TKE along the top of the stagnation zone early on in the breaking process.

Simulations focusing on the effects of surface fluxes and boundary layers on internal waves have largely applied mesoscale models that are not turbulence resolving. For example, Jiang et al. (2006) examined the role of the boundary layer, surface heat fluxes, and drag on trapped waves generated by a two-layer atmospheric structure. Their scenario was quite different from conditions we examined in that trapping was produced by a reduction in stratification with height rather than the nonlinear effects of a self-induced critical level. Consequently, it is not too surprising that their results differ from ours. In particular, they found that the boundary layer acts as a sponge for trapped waves by partially absorbing down going wave energy. For stagnant, stable surface conditions forced by surface cooling, wave absorption was highly efficient because of the formation of a critical level when the flow decreases to zero. We find a directly opposite result; surface cooling in our simulations enhances lee side waves by decoupling the waves from turbulence generated at the surface, whereas surface heating decreases lee wave intensity by disrupting the lee wave system through increased turbulent mixing.

Differences between our study and Jiang et al. (2006) are mostly likely tied to the very different lee wave characteristics. In our experiments, the lee side atmospheric structure is similar to an interfacial wave scenario with a two-layer structure divided by a

thin, strongly stratified layer. Waves are trapped along the interfacial layer and propagate horizontally along the interface with little vertical propagation. In contrast, waves in the Jiang et al. (2006) case have a vertical structure that spans a stratified fluid depth many times the boundary layer depth and mountain height. Vertical energy propagation in these waves is much larger relative to our cases, allowing for greater loss of wave energy in the boundary layer. Ultimately, waves in our simulations are more strongly affected by turbulent processes whereas waves in Jiang et al. (2006) are governed more by internal wave dynamics.

In a more recent mesoscale modeling study, Jiang et al. (2008) examined the effects of surface heating using idealized conditions with a simple ridge, where the internal wave response was strongly controlled by surface fluxes. With no fluxes, their simulations produced a very weak internal wave response. They found that cooling forced a lee side jet similar to a mountain wave response, in partial agreement with our cooling experiment. The effect of heating on the downstream side of the ridge was also examined, similar to our experiment contrasting upstream and downstream heating. However, in their experimental setup, heating on the downstream side of the ridge increased the cross-mountain pressure gradient, resulting in a stronger lee side jet rather than a more turbulent downstream boundary layer. Overall, their experiments suggest that for large-scale mountains (100's km), the effects of heating on buoyancy and cross-mountain pressure gradient are more important than the effects of turbulent mixing. In our case, both the height and width of the mountain are much smaller and so, not surprisingly, the turbulent boundary layer has a larger impact on the flow dynamics.

Many unanswered questions remain regarding the relative importance of environmental factors such the role of upper level stratification, elevated inversions and ridge-top level shear in the formation of downslope windstorms and rotors. While results presented here address some of the outstanding issues regarding the importance of surface heat fluxes in nonlinear trapped lee wave regimes, a significant portion of the physically feasible parameter space (based on upstream soundings taken during T-REX and elsewhere) remains unexplored. Moreover, it is not clear that synoptically based upstream soundings (i.e. once every 12 hours) can help to resolve these issues, hence we intend to continue to explore the relative importance of these factors in the onset and

decay of lee flow regimes, especially those with hydraulic jump conditions and rotors, which are considered extremely hazardous to the aviation community.

Acknowledgements: We are pleased to acknowledge the super-computer time provided by the National Center by Atmospheric Research, which is funded by the National Science Foundation. This research was funded by the National Science Foundation under grant ATM-0527790. We also wish to thank the anonymous reviewers for their help in strengthening the manuscript.

Figures

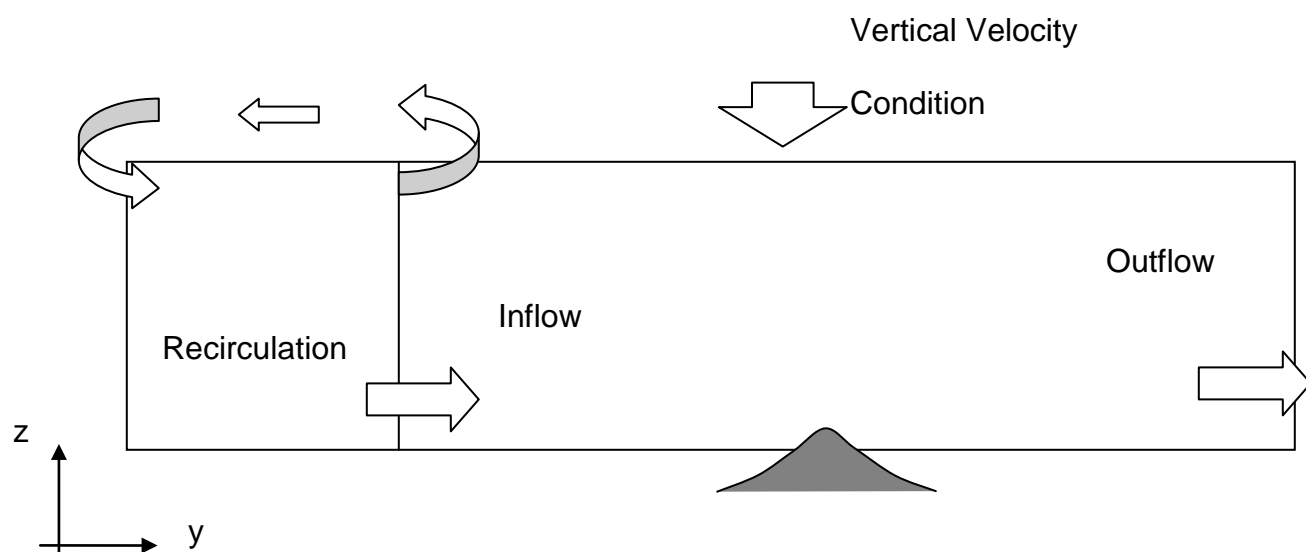


Figure 2.1. Schematic showing the channel flow configuration used in the simulations.

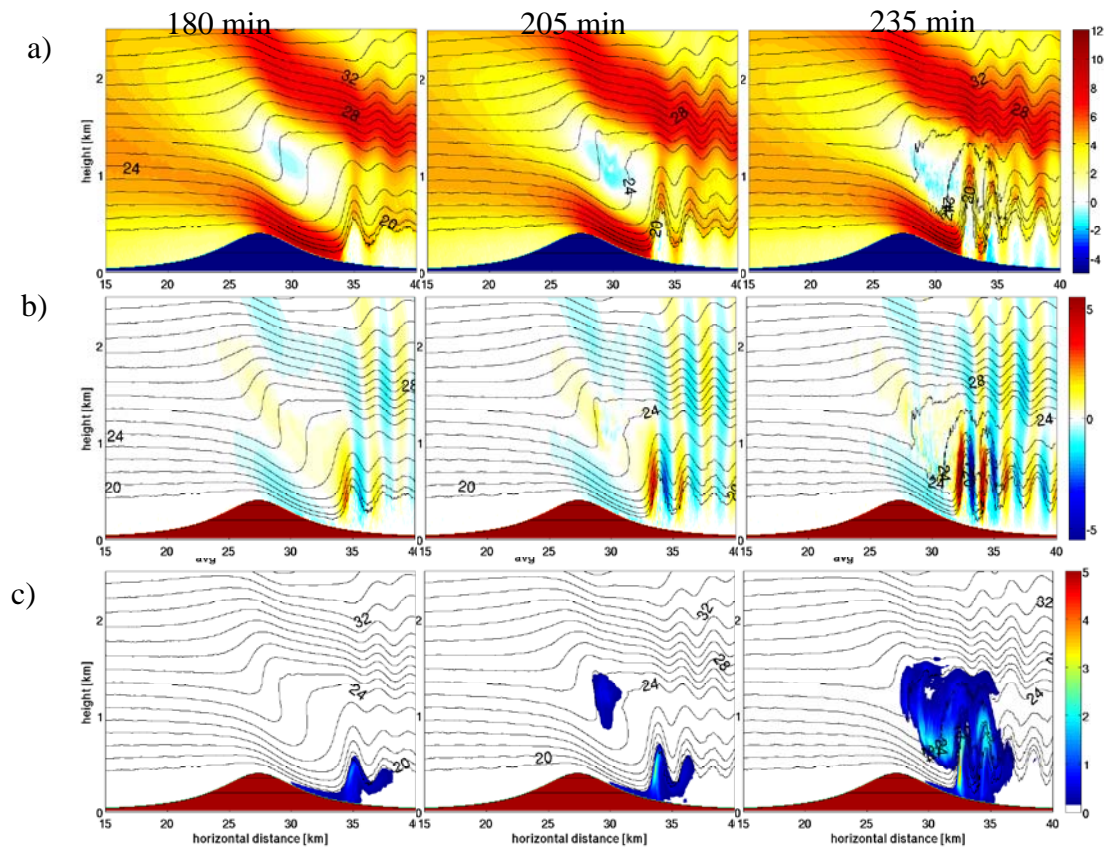


Figure 2.2. Close up view of a) streamwise velocity (shading in ms^{-1}), b) vertical velocity (shading in ms^{-1}), and c) average TKE (shading in m^2s^{-2}) and potential temperature (lines of constant $^{\circ}\text{C}$) for the no heating case at $t = 180$ min (left column), $t = 205$ min (middle column) and $t = 235$ min (right column).

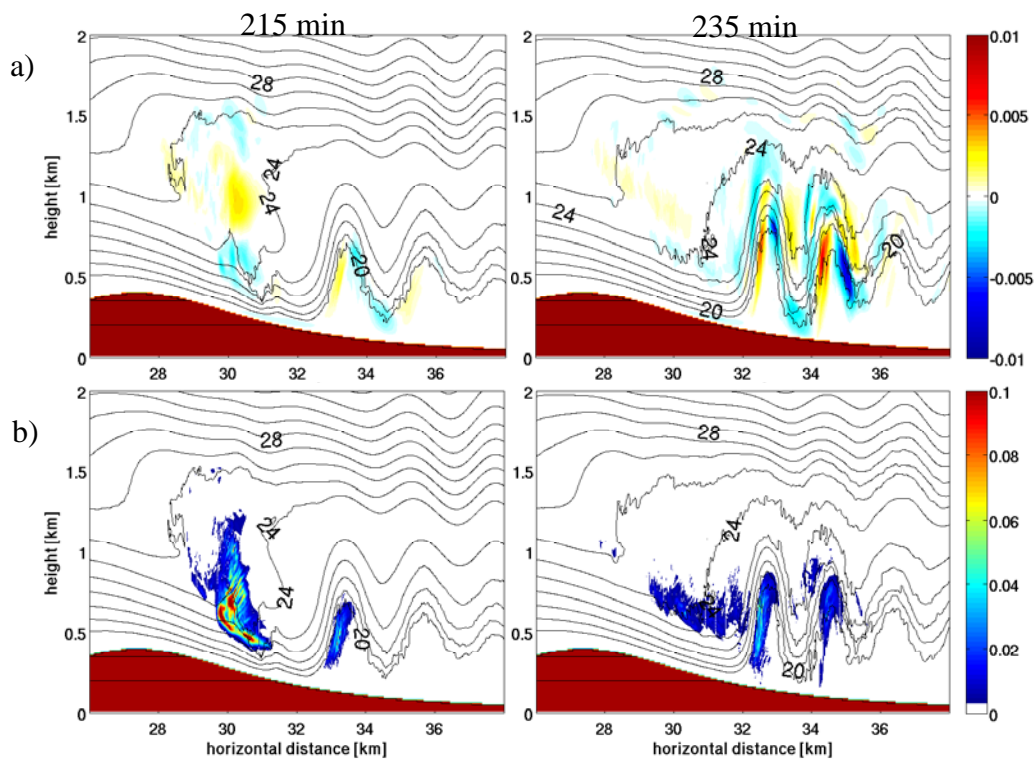


Figure 2.3. Close up view of average TKE budget terms of a) buoyant production of TKE and b) shear production of TKE (shading in m^2s^{-3}) and potential temperature (lines of constant $^{\circ}\text{C}$), for the no heating case at $t = 215$ min (left column) and $t = 235$ min (right column).

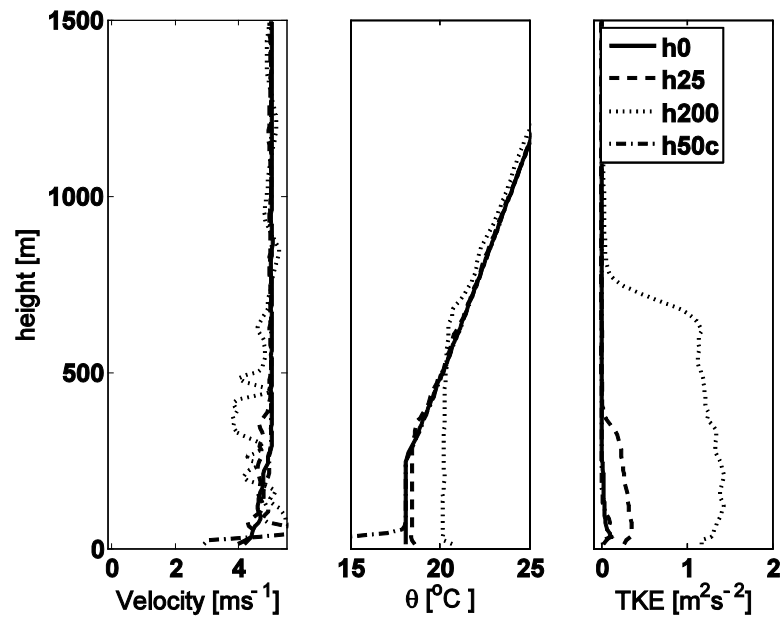


Figure 2.4. Inflow near surface velocity (a), potential temperature (b), and TKE (c) profiles at $y = 4$ km for the experiments at $t = 200$ min.

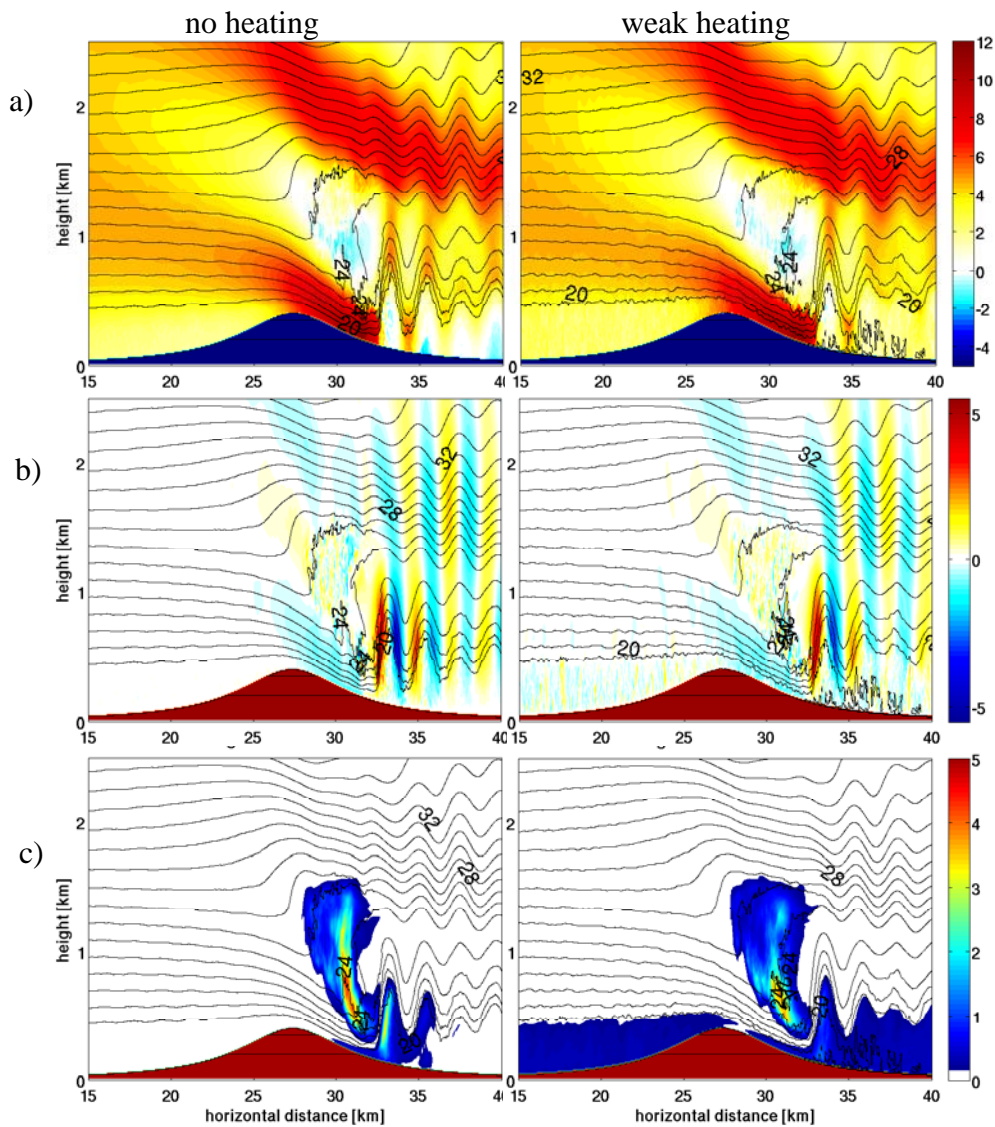


Figure 2.5. Close up view of a) streamwise velocity (shading in ms^{-1}), b) vertical velocity (shading in ms^{-1}), and c) average TKE (shading in m^2s^{-2}) and potential temperature (lines of constant $^{\circ}\text{C}$) at $t = 220$ min for the no heating case (left column), weak heating case (2nd column), strong heating case (3rd column) and cooling case (right column).

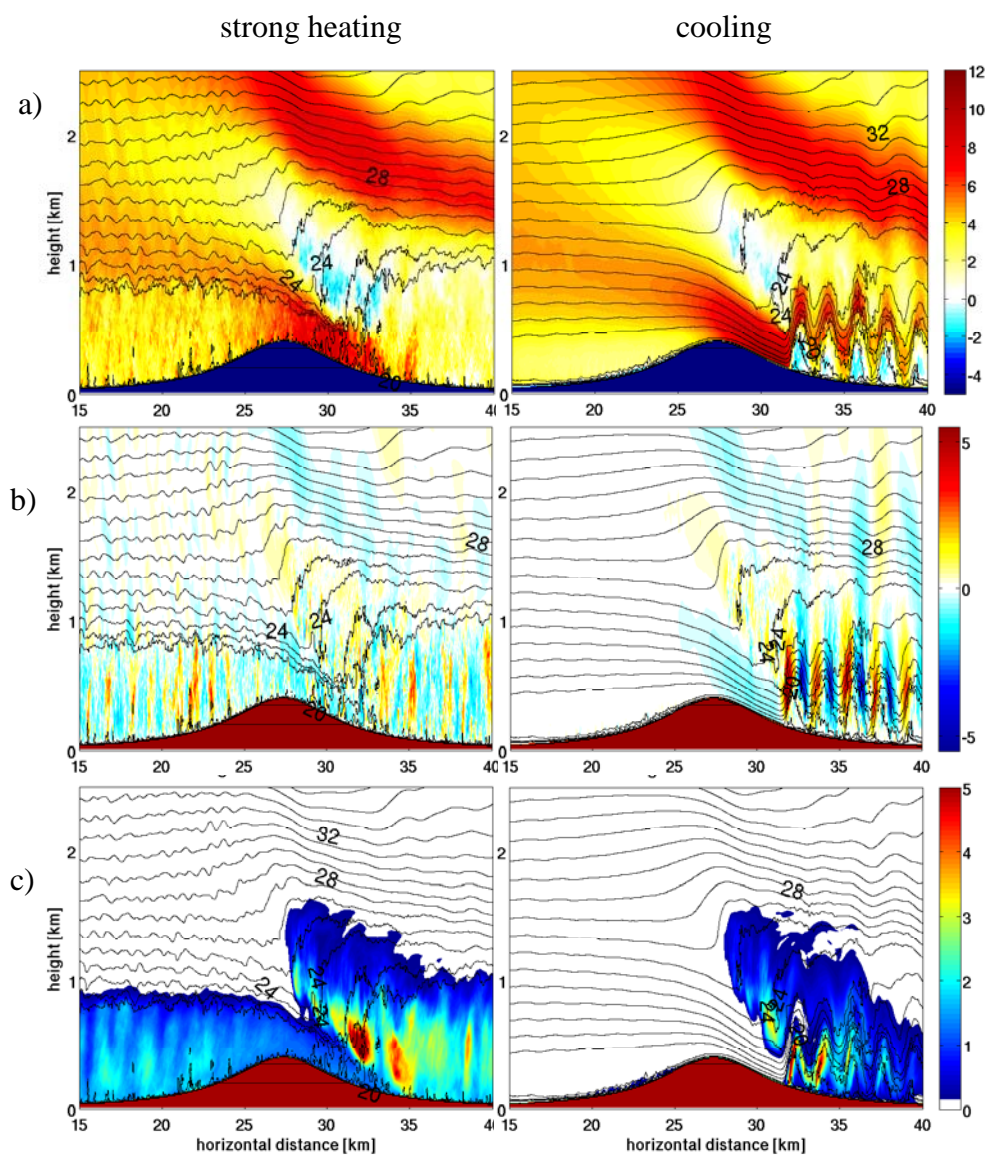


Figure 2.5 continued.

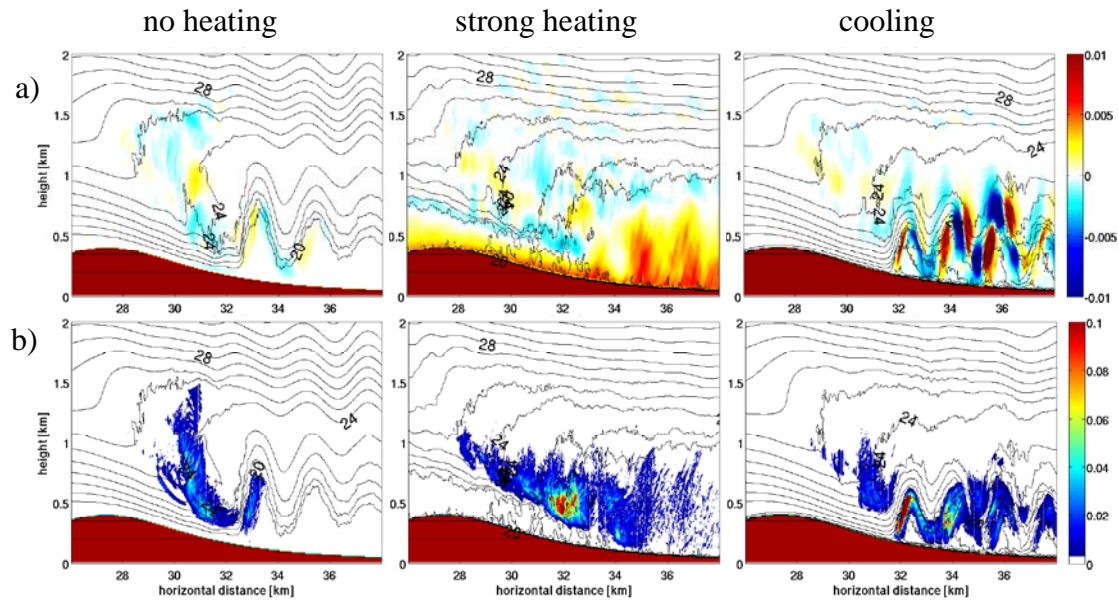


Figure 2.6. Close up view of average TKE budget terms of a) buoyant production of TKE and b) shear production of TKE (shading in m^2s^{-3}) and potential temperature (lines of constant $^{\circ}\text{C}$) at $t = 220$ min for the no heating case (left), strong heating case (middle) and cooling case (right).

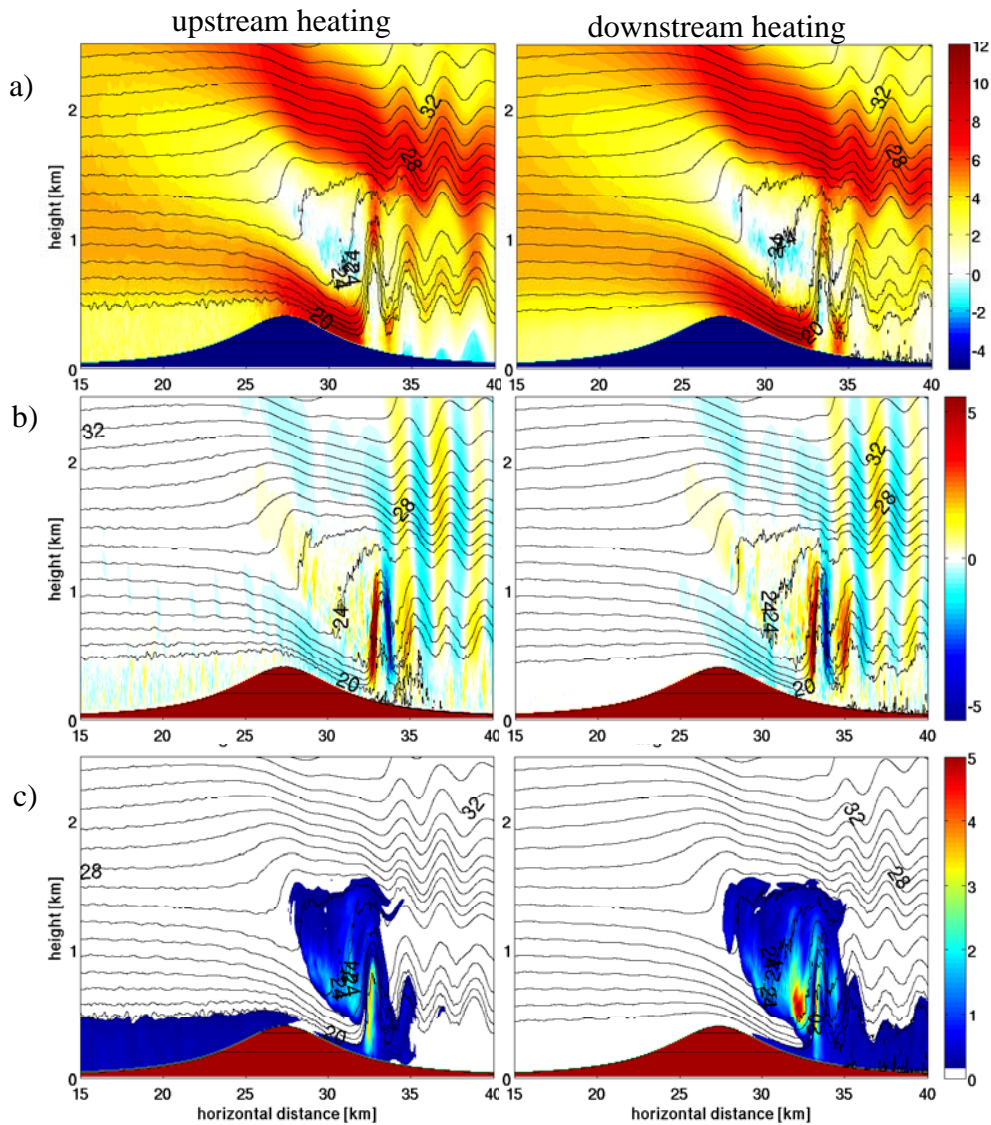


Figure 2.7. Close up view of a) streamwise velocity (shading in ms^{-1}), b) vertical velocity (shading in ms^{-1}), and c) average TKE (shading in m^2s^{-2}) and potential temperature (lines of constant $^{\circ}\text{C}$) at $t = 230$ min for the upstream heating case (left), and downstream heating case (right).

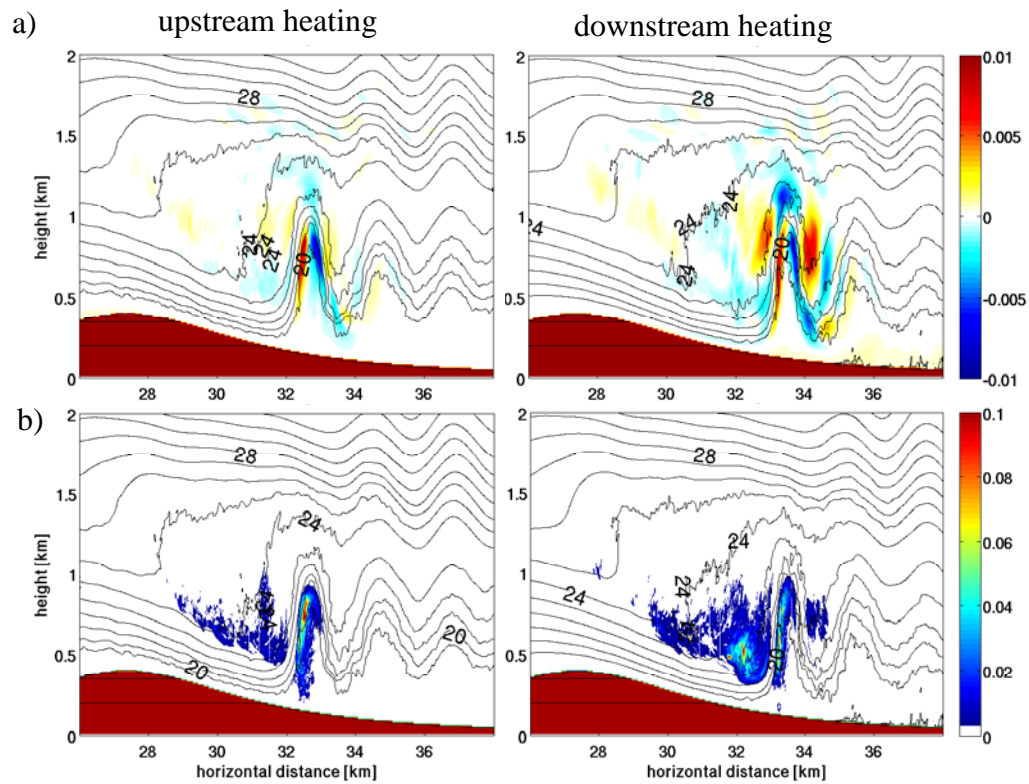


Figure 2.8. Close up view of average TKE budget terms of a) buoyant production of TKE and b) shear production of TKE (shading in m^2s^{-3}) and potential temperature (lines of constant $^{\circ}\text{C}$) for the upstream heating case (left) and downstream heating case (right) at $t = 230$ min.

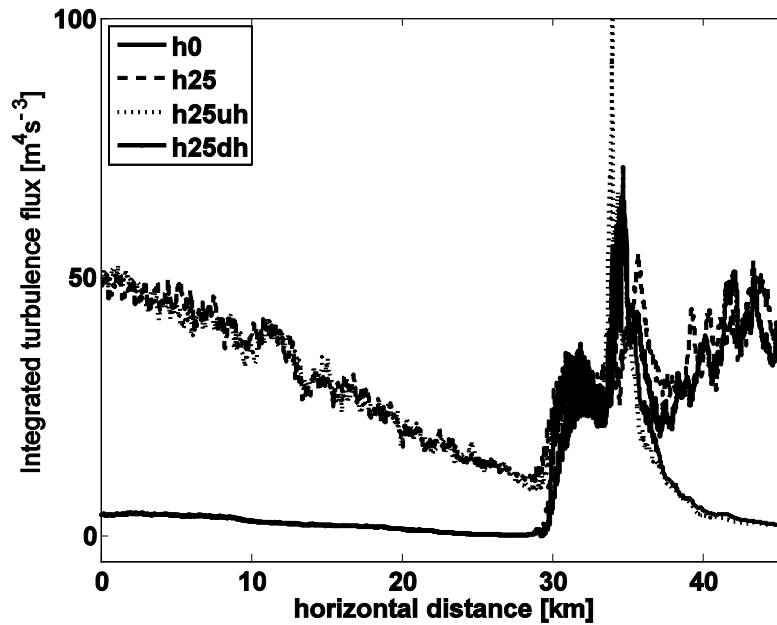


Figure 2.9. Integrated turbulent flux for no heating, weak heating, upstream heating, and downstream heating cases at $t = 195$ min.

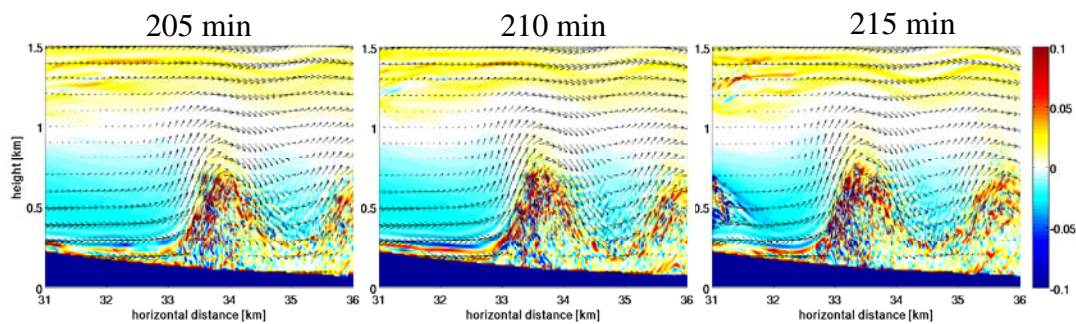


Figure 2.10. Close up view of spanwise vorticity (shading in s^{-1}) and vectors of flow velocity at $t = 205, 210,$ and 215 min for the no heating case.

Tables

Run name	Surface Heating (Wm^{-2})
No heating (h0)	0
Weak heating (h25)	25
Strong heating (h200)	200
Cooling (h50)	-50
Upstream heating (h25uh)	25 (upstream only)
Downstream heating (h25dh)	25 (downstream only)

Table 2.1: List of all simulations and their characteristics.

An inversion based instability mechanism for downslope windstorms

Craig M. Smith and Eric D. Skillingstad

College of Oceanic and Atmospheric Sciences

104 COAS Admin Bldg

Oregon State University, Corvallis, OR 97331-5503, USA

Submitted to Journal of Atmospheric Sciences

Abstract

A new mechanism of leading to the generation of downslope windstorms is proposed based on results from large eddy simulations (LES) of two dimensional ridge with upstream inversions of varying heights. This mechanism involves instabilities on the inversion which couple with shear production of turbulence resulting in a growing stagnation zone below which the flow is forced forming a lee surface jet. Momentum budget analysis show the creation of vertical profiles of velocity and buoyancy which are unstable with respect to perturbations by the combined action of pressure gradient forces and nonlinear advection associated with the flow response to the topographical perturbation. These forces act to split the inversion and slow the horizontal flow down, thus creating a pocket of neutrally stratified stagnant air. In this nascent stagnation zone instabilities spontaneously occur and grow, thus creating a large stagnation zone and associated lee surface jet.

Previous suggested mechanisms of downslope windstorm formation of trapping of internal gravity (IGW) energy by the inversion, nonlinear hydrostatic IGW breaking and a subcritical to supercritical transition of the shallow water mode are explored with respect to the experiments presented. In cases with inversions present downslope windstorms may occur for small forcing, i.e. mountain height below which IGW breaking would not be expected to occur. Overall, the inversion instability mechanism, which many mesoscale models may not be able to adequately resolve, predicts the formation of downslope windstorms in cases where traditional theories of nonlinear IGW breaking and transition of the barotropic mode do not.

3.1. Introduction

The presence or absence of an upstream inversion often leads to downslope windstorms by one of two mechanisms: internal gravity wave (IGW) breaking in cases lacking an upstream inversion, or a supercritical transition of the barotropic mode for cases with an inversion. The dichotomy between the two mechanisms is not entirely unambiguous however and the dynamics of downslope windstorms induced by interfacial phenomena supported on inversions has not been as thoroughly explored as those induced by IGW breaking, especially considering that the criteria for inversion based windstorms may be substantially different than the criteria for IGW breaking in a continuously stratified system.

The propensity for downslope windstorm events to occur in conjunction with upstream inversions has been well established in U.S. locations as widespread as the Sierra Nevada's (Colson 1954, Kuettner 1959), the Front Range of the Rocky Mountains (Brinkmann 1974, Bower and Durran 1986), and Southeast Alaska (Colman and Dierking 1992). Yet other studies suggest that ridgetop level inversions may not be so important. In fact, in the Washington Cascades, crest level stability was shown to be less correlated with strong lee flow winds than wind speed at ridge top level, sea level pressure gradient, and the height of a mean state critical level (Colle and Mass 1998).

The ambiguity between inversion based downslope windstorms and those induced by breaking IGW and self-induced critical levels is prevalent in the Alps as well, where the foehn sometimes occurs contemporaneously with IGW breaking, as shown by lidar observations (Gohm and Mayor, 2004), and also occurs during periods in which upstream inversions are observed. The bora as well is also sometimes associated with upstream inversions, and other times associated with IGW breaking (Glasnovic and Jurcec 1990, Klemp and Durran 1987, Gohm and Mayor 2005, Belusic et al. 2007, Klemp et al. 1997, Gohm et al. 2008).

Recent observations on the Falkland Islands (Mobbs et al. 2005) illustrate the ambiguity as well. On one hand the authors show that downslope windstorms are correlated with non-dimensional mountain height,

$$\hat{h} = \frac{Nh}{v} \quad (1)$$

where N is the Brunt-Vaisala frequency,

$$N = \sqrt{\frac{g}{\theta_0} \frac{\partial \theta}{\partial z}}, \quad (2)$$

h is the ridge height, v is the cross-ridge velocity, g is the acceleration due to gravity, θ is the potential temperature, and θ_0 is a reference potential temperature, suggesting that IGW nonlinearity and breaking is the dominant mechanism for the downslope windstorms. On the other hand the authors also show that the lee slope winds are also correlated with the reduced gravity shallow water (RGSW) Froude number,

$$Fr = \frac{v}{\sqrt{g' z_i}} \quad (3)$$

where the reduced gravity, g' is defined as

$$g' = g \frac{\Delta \theta}{\theta_0} \quad (4)$$

z_i is the height of the inversion, and $\Delta \theta$ is the strength of the inversion. The Froude number is the ratio of fluid speed to the speed of RGSW waves, and indicates the direction of propagation for barotropic interfacial waves on the inversion.

To adequately address and differentiate the role of upstream inversions and IGW breaking in downslope windstorms, researchers have generally resorted to modeling studies focusing on either the importance of IGW breaking in continuously stratified systems or the applicability of RGSW theory in 2-layer hydraulically controlled flow. A major distinction between the two models is that continuously stratified models allow for vertical energy propagation, which in some circumstances can be constrained thru the creation of a self-induced critical layer via IGW breaking, while RGSW models, which do not require stratification anywhere besides the inversion itself, can support interfacial waves on the inversion but cannot support vertical energy propagation. Many numerical studies have focused on the former as an explanation for the observations of IGW breaking in the January 11, 1972 Boulder downslope windstorm case (Lilly and Zipser 1972; Clark and Peltier 1977; Peltier and Clark 1979; Doyle et al. 2000). With regards to the latter, many studies have shown that the hydraulic analogy can adequately address

observations of downslope windstorms without the occurrence of IGW breaking. The RGSW models, which are based upon hydraulic flow concepts, have a rich history dating back to Long's (1954) two layer seminal work. Contributions to this model were made by Houghton and Kasahara (1968), whose single layer hydraulic flow model conserved mass and momentum, Klemp et al. (1997) who chose instead to conserve energy, and Rotunno and Smolarkiewicz (1995) who studied vorticity generation in shallow water hydraulic jumps. Successful applications of the RGSW model to explain observed lee flows in the atmosphere include the bora (Gohm et al. 2008); shallow fohn (Flamant et al. 2002); and Tramontane events (Drobinski et al., 2001).

The groundwork for analogies between hydraulic theory (RGSW models) of downslope windstorms and continuously stratified systems began with the studies of Durran (1986) and Smith (1985). The case for the analogy between RGSW and IGW breaking models was made more explicitly shortly thereafter (Durran and Klemp 1987; Liu et al. 2000), where equivalences for an interfacial wave Froude number were made with a Froude number for a continuously stratified system. More recently researchers have begun to further link the RGSW model to continuously stratified cases via numerical experiments. Vosper's (2004) modeling study included both IGW breaking simulations and hydraulic jump simulations. His results (see his figure 9) may be thought of as extension of Houghton and Kasahara's (1968, see their figure 3) for two-layer flows in which the upper layer is stratified and the lower layer is neutral. Jiang et al. (2007) also modeled the importance of an upstream inversion. Although the authors of this study claim that the shallow water mode is dominant in their experiments, it is not possible to ascertain to what extent IGW breaking above the lee slope (see the isotherms at the top of their figure 14) plays a role in their experiments. Despite recent progress many uncertainties remain regarding the distinction between downslope windstorms associated with elevated inversions and those associated with IGW breaking.

The goal of this study is to examine eddy resolving numerical experiments of downslope windstorms for causes other than hydrostatic wave trapping, IGW breaking and subcritical to supercritical transition of the barotropic interfacial mode. The paper is structured as follows. A description of the large eddy simulation (LES) model is presented in Section 2 along with an outline of the experiments performed in our study.

Results are presented next in Section 3 for a comparison of cases which do and do not contain an inversion at various heights. We first explore these cases with respect to IGW trapping and transition of the RGSW mode. Next we examine the cause of turbulence and growth of the stagnation zone for the medium inversion height case. In section 4 we look more closely at the role of IGW breaking in determining lee flow response for the medium inversion height case. Finally we investigate the causes of initiation of instabilities on the inversion. Summary and conclusions are given in Section 5.

3.2. Model Introduction and Setup

Experiments were performed using a modified version of the LES model described in Skillingstad (2003) and used in Smith and Skillingstad (2005) and Smith and Skillingstad (2009). This model is based on the Deardorff (1980) equation set, with the subgrid-scale model described by Ducros et al. (1996). Pressure in the model is calculated using a compressible pressure solver (Klemp and Wilhelmson, 1978). Terrain in the LES model is prescribed using a shaved cell approach described in Adcroft et al. (1997) and Steppeler et al. (2002). This approach was selected over the more commonly used terrain following coordinate methods to avoid problems with the LES filtering assumptions. Comparisons between mountain waves simulated using terrain-following coordinates and the shaved cell approach show only minor differences (Skillingstad and Wijesekera, 2004). Further tests, which are not shown, confirm that simulations using this model compare quite well with previously reported results (Steppeler et al., 2002, figures 2 and 3).

Simulations were conducted using a narrow channel domain with periodic boundaries in the cross slope and along slope direction (figure 3.1). We used a sponge layer in the along slope direction in the first 10 kilometers of the domain to return the flow to an unperturbed upstream condition (Bacmeister and Pierrehumbert, 1987).

A limited-slip lower boundary for some of the simulations was set by assuming a neutral log scaling and setting the subgrid momentum flux to

$$\langle v''w'' \rangle = C_D v^2 \quad (5)$$

$$C_D = \left[\frac{\kappa}{\ln(\delta z/z_o)} \right]^2 \quad (6)$$

with a surface roughness, $z_o = 0.01$ m, where $\langle v''w'' \rangle$ is the average subgrid scale momentum flux, C_D is the drag coefficient, w is the velocity in the vertical direction, $\kappa = 0.4$ is the von Karman constant, and $\delta z = \Delta z/2$ is half of the vertical grid spacing. The turbulent viscosity, K_m , is specified in the lowest grid cell only following similarity theory

$$K_m = u_* z \kappa \quad (7)$$

where u_* is the friction velocity defined in the usual manner. The top boundary condition was a rigid lid with a sponge layer following Durran and Klemp (1983) having a depth of 8 km, which was greater than the wavelength of the dominant waves generated by the mountain in our model. We chose the sponge layer depth to eliminate significant downward energy reflection.

A two-dimensional ridge obstructing the flow was based on the Witch of Agnesi profile

$$h(y,z) = \frac{h a^2}{y^2 + a^2} \quad (8)$$

for a mountain of height, $h = 600$ m, and width, $a = 4000$ m, which is comparable to the rotor inducing terrain on the Falkland Islands (Mobbs et al., 2005).

An idealized initial state is prescribed with constant static stability of $N = 0.01$ s⁻¹. The streamwise velocity, v , increases linearly from 5 m s⁻¹ to 11.5 m s⁻¹ at 13 km. Temperature inversions, if present, are centered at $z_i = 900, 1800,$ and 3000 m and all have a depth of 200m. Using the velocity at crest level of 5 ms⁻¹ and the free troposphere stability, $N = 0.01$ s⁻¹, a non-dimensional mountain height of $Nh/v = 1.2$, and a non-dimensional mountain width of $Na/v = 8$ were prescribed for our simulations.

Domain size was set to 80 x 6480 x 300 grid points in the along slope, cross slope, and vertical directions respectively, with grid resolution of 15 m in all directions below 3 km. Above 3 km, the vertical grid spacing stretches from 15 m to 170m at the model domain top. The total domain size was 1.2 km x 97.2 km x 13.1 km. The mountain was centered at $y = 58.3$ km, slightly past the center point in the streamwise direction. A summary of all experiments can be found in tables 3.1 and 3.2.

3.3. Inversion height results

a. Overview of the inversion level experiments and IGW breaking

We first examine the role of inversions and inversion height in determining lee flow response by conducting a set of four cases having different inversion heights as described in table 3.1. Cross-section plots of streamwise velocity overlaid with contours of potential temperature are shown in figure 3.2. In this figure we have chosen to present results at dynamically important times in the flow evolution; we have run all the experiments until the flow response is fully mature. Like other investigators, we note that the experiments do not achieve steady state. All variables presented in the plots are instantaneous at a single cross section in the model domain unless otherwise specified as being averaged. For the purposes of this study we define the average of a variable ϕ as follows.

$$\bar{\phi}(y,z) = \frac{1}{i_{\max} \cdot n_{\max}} \sum_{n=1}^{n_{\max}} \sum_{i=1}^{i_{\max}} \phi(x,y,z) \quad (9)$$

where the overbar denotes average. In this equation i_{\max} is the number of points in the spanwise direction and n_{\max} is the number of time steps over the 5 minute averaging time.

Figure 3.2 for the no inversion case (a) shows a time when a self-induced critical level near $z = 2.5$ km becomes buoyantly unstable and generates a breaking wave with considerable turbulence. This experiment is broadly comparable to the basic case presented in an earlier study (Smith and Skillingstad, 2009) except with shear added to help avoid elevated secondary breaking regions. Just before the onset of IGW breaking the isotherms become vertical and begin to overturn, generating increasing turbulence aloft. Streamwise velocity shows a typical nonlinear amplified gravity wave response with a large zone of trapped, stagnant air with near zero streamwise velocity over the lee of the mountain between 2 and 3 km high. Beneath this stagnant layer is a jet of increased winds along the surface of the lee of the mountain. Turbulence, initially limited to the boundary layer beneath the evolving first rotor circulation defined by the boundary layer separation of the surface jet near $y = 65$ km, is advected throughout the stagnation zone and over the rotor system. The trapped lee wave rotors (we define a rotor

as a negative streamwise surface velocity) are partly due to the nonhydrostatic forcing of the mountain on the flow ($Na/v = 8$) and partly due to nonlinear interactions with the IGW breaking and stagnation zone (this phenomena is also shown in Jiang et al., 2007, figure 14b). Broad mountains generally tend to launch hydrostatic waves but, due to interactions with the self induced stagnation zone in highly nonlinear cases, can also launch dispersive waves. Vertical velocities associated with the rotors nearest the mountain are intensified during the breaking process and the rotor heights increase. Turbulence from the stagnation zone is not strong enough to mix out negative streamwise velocities within in the rotor nearest to the mountain.

Figure 3.2 for the low inversion case (b) shows the time period when the barotropic mode on the inversion at $z_i = 900\text{m}$ transitions from subcritical to supercritical. Initially there is very little turbulence present as the flow descends the lee slope. Breaking then becomes evident on the upstream side of the incipient hydraulic jump. Vertical velocities at the edge of the shooting flow are fairly high at this time. The fully developed flow descends well past the base of the slope and is almost entirely beneath a stagnation zone, which is in turn constrained below the inversion at 900m. Downstream, the inversion then returns relatively intact to $z_i = 900\text{ m}$. The lee slope flow evolves much faster in this simulation with a strong downslope flow in 120 min versus 360 min for IGW breaking case. Both hydrostatic, vertically propagating internal gravity waves and trapped lee waves are evident above the inversion but play only a small role in the slope flow.

As in the low inversion case, the medium inversion height case (2c) also shows both a weak hydrostatic IGW and lee wave response above the inversion. This case, however, has a lee side downslope flow which is much deeper than the low inversion case. Rotors are also produced, more in line with the no inversion case, but they are located much further downstream, and their height is constrained to be less than the inversion. The mechanism for the generation of the lee slope flow, which is shown in more detail in figure 3.3, is a bit different for this case and explored in more detail below. The lee flow response begins with a mountain wave induced perturbation which is mostly constrained beneath the inversion (fig 3.3a). As the perturbation on the inversion grows the inversion splits, creating a pocket of neutrally stratified stagnant air (fig 3.3b). In this

pocket shear production of turbulent kinetic energy (TKE) occurs (fig 3.3c) and acts to grow the nascent stagnation zone downstream. As the stagnation zone propagates downstream, the lee jet is forced beneath it, resulting in a long lee slope jet (fig 3.3d).

A large rotor and self-induced stagnation zone is present in the high inversion case (figure 3.2d). Downstream of the rotor the surface jet is highly turbulent and downstream of the first rotor another stagnation zone is present. The dominant physics for both the high inversion case and the no inversion case (figure 3.2a) is that of IGW breaking. The nonlinearity parameter for internal gravity waves for these cases, $Nh/v = 1.2$, corresponds to a hydrostatic vertical wavelength,

$$\lambda_z = 2\pi \frac{v}{N} = 3142m, \quad (10)$$

using $v = 5 \text{ ms}^{-1}$, with a corresponding level of IGW breaking of $3/4 * \lambda_z = 2356 \text{ m}$. Since the level of IGW breaking is less than the height of the inversion, $z_i = 3000\text{m}$, the IGW breaking dynamics are relatively unaffected by the presence of the inversion, and the lee flow for the no inversion and high inversion cases are relatively similar. More generally, the ratio of hydrostatic vertical wavelength (or level of IGW breaking), to inversion height, λ_z/z_i , is very useful in describing the flow for nonlinear IGW cases (i.e. $Nh/v > 1$). Compared to the no inversion case, the high inversion case has reduced vertically propagating IGW energy aloft and slightly a stronger and more turbulent lee jet.

b. IGW trapping

We next examine the role of IGW trapping in the lee flow response by examining the mean kinetic energy (KE) aloft, which we take as the square of the largest absolute value of vertical velocity in the vertically propagating hydrostatic IGW response above the mountain, inversion, and self-induced stagnation zone and below $z = 5 \text{ km}$, and between $y = 55\text{-}70 \text{ km}$ at the times presented in figure 3.2. The mean KE was obtained for all cases and is listed in table 3.1. The amount of IGW aloft can also be examined qualitatively by noting the displacement of the isotherms in the region above the mountain. The no inversion case (fig 3.2a) has much more KE aloft than does the low inversion case (fig 3.2b), whose inversion height is much lower than the hydrostatic wavelength. Both the medium (fig 3.2c) and high inversion (fig 3.2d) cases have only

about a quarter of the KE aloft in comparison with the no inversion cases. The no inversion case radiates significantly more energy in vertically propagating IGW than the high inversion case yet the lee flow in both cases looks similar besides the large stagnant zone downstream of the first rotor in the high inversion case. Given the dominant role of IGW breaking in both simulations, the trapping of IGW energy by the inversion seems to play very little role in the formation of the downslope jet and rotor in the high inversion case. Further experiments on the importance of IGW trapping are presented in part 4 and supplemental numerical experiments, which are not shown, were performed to test how the free tropospheric stability affects the lee flow beneath the inversion. In these experiments we varied the free troposphere stability for various inversion heights. The results showed that the lee flow beneath the inversion is relatively insensitive to upper layer stability. Experiments with a rigid lid at inversion height were also qualitatively similar.

c. RGSW mode

It has often been suggested that downslope windstorms associated with inversions occur as a result of hydraulically controlled flow in which there is a subcritical to supercritical transition of the barotropic mode at the ridge crest (Houghton and Kasahara, 1968, Gohm and Mayr, 2004). We consider this notion in figure 3.4, which shows the shallow water Froude number as a function of downstream distance for the low inversion, medium inversion and high inversion cases at the times presented in the figure 3.2. The shallow water barotropic Froude number is defined as in (3) and (4), with $\Delta\theta = 8$ K and a height that is based on the inversion height or the top of the lee slope shooting flow, whichever is lowest, minus the height of the mountain or any rotor if present. The shallow water Froude number for the no inversion case is not shown since in a continuously stratified system there is arguably no well defined inversion layer. Another way to view the continuously stratified system is as a combination of interfacial layer flows of varying strength and depth, however the strength of the inversion of arbitrary depth, corresponding to $N = 0.01\text{s}^{-1}$, would be so low that any calculated shallow water Froude number would be supercritical.

Interestingly, in the medium and high inversion cases the lee flow jet is well below the entire inversion, and has θ values less than the inversion, rather than the inversion coming down to cap the lee jet as in the low inversion case (and as in the simulations of Jiang et al., 2007). The stagnation zone is also located below the inversion and there is significant entrainment of the inversion air in the lee flow (which also occurs in some of the Vosper, 2004 experiments, see his figure 8). It can be argued that the use of the upstream inversion strength is not correct over the lee surface jet for these cases, since the inversion itself does not cap the shooting flow. In this paradigm, however, it's not clear what the inversion strength should be over the lee flow surface jet. It may perhaps be incorrect to choose an inversion strength based on the upstream undisturbed strength of the inversion but there are actually no obvious reasons to assume that interfacial waves are the predominant physics in any of the experiments besides the low inversion case.

The low inversion case is the only one which undergoes a subcritical to supercritical transition near the ridge crest based on the inversion height Froude number. Despite its strong resemblance to hydraulically controlled flow, the barotropic Froude numbers in the medium and high inversion cases are not consistent with a hydraulic control point at the ridge crest and subcritical to supercritical transition of the shallow water mode on the inversion. Notably the perturbations on the inversion above the lee slope have a horizontal length scale on the same order as the height of the inversion itself. Since the barotropic mode is a hydrostatic phenomena, the horizontal length scale should be much larger than the inversion height. Additionally, hydraulic analogies of the no inversion case suffer from uncertainties regarding the inversion strength and inversion depth.

d. TKE and growth of the stagnation zone

To better understand the growth of the stagnation zone we present cross-section plots of average resolved eddy TKE overlaid with contours of potential temperature in figure 3.5 for the low inversion case and medium inversion case at the same times presented in figure 3.2. Average resolved eddy TKE is calculated as follows. The spanwise mean of a variable ϕ

$$\phi_{spanwise\ mean}(y, z) = \frac{1}{i_{max}} \sum_{i=1}^{i_{max}} \phi(x, y, z) \quad (11)$$

is used to calculate perturbations about the spanwise mean

$$\phi'(x, y, z) = \phi(x, y, z) - \phi_{spanwise\ mean}(y, z) \quad (12)$$

and resolved eddy TKE is defined as

$$e' = \frac{1}{2} (u'^2 + v'^2 + w'^2), \quad (13)$$

the perturbation velocities are calculated as in (11) and (12), and the averaging is done temporally over 5 minute intervals as well as in the spanwise direction as in (9).

Computing averages in this way removes the large-scale internal waves generated by the mountains, however smaller scale waves are still treated as “turbulence.” Nevertheless, this method yields turbulence fields that are consistent with shear production of turbulence as shown below. Also shown in figure 3.5 is the shear production term in the TKE budget defined as

$$\frac{\partial e}{\partial t} = \underbrace{-U_j \frac{\partial e}{\partial x_j}}_{\text{I}} + \underbrace{\delta_{i3} \frac{g}{\theta_0} \overline{u'_i \theta'_i}}_{\text{III}} - \underbrace{\overline{u'_i u'_j} \frac{\partial U_i}{\partial x_j}}_{\text{IV}} - \underbrace{\frac{\partial (\overline{u'_j e})}{\partial x_j}}_{\text{V}} - \underbrace{\frac{1}{\rho} \frac{\partial (\overline{u'_i p'})}{\partial x_i}}_{\text{VI}} - \underbrace{\varepsilon}_{\text{VII}}, \quad (14)$$

where U_j represents the spanwise average velocity components, ε is the dissipation of turbulence, ρ is the density, p' is the perturbation pressure, and over bars represent a spanwise average. Terms in (11) are defined as TKE storage (I), horizontal advection (II), buoyant production/destruction (III), shear production (IV), turbulent transport (V), pressure transport (VI), and dissipation (VII).

There is substantial near surface TKE in the low inversion case (figure 3.5a) due to the large shear production term (figure 3.6a) in the area where the inversion capping the lee surface jet returns to its upstream height. In this and all other cases, shear production dominates the TKE budget. In contrast, TKE in the medium inversion height case (figure 3.5b) starts at the instability on the inversion, and is largely confined to the stagnation zone in between the surface jet and the inversion. Shear production (figure 3.6b) is largest at the interface of the stagnation zone and the surface jet, where horizontal

velocity gradients are strongest. Gradually this production moves downwards and downstream acting to grow the nascent stagnation zone.

e. Inversion instabilities

Instabilities on the inversion and associated coupling of the stagnation zone with the lee surface jet are very important to the lee surface jet dynamics in the medium inversion case. The stability of the lee flow with respect to small perturbations can be examined with the Taylor Goldstein (TG) equation,

$$(U - c) \left(\frac{\partial^2}{\partial z^2} - k^2 \right) \hat{\psi} - U_{zz} \hat{\psi} + \left(\frac{N^2}{U - c} \right) \hat{\psi} = 0, \quad (15)$$

where the streamfunction, φ , is defined as

$$u = \frac{\partial \psi}{\partial z}, \quad w = -\frac{\partial \psi}{\partial x}. \quad (16)$$

We first show a close up of the gradient Richardson number,

$$Ri_g = \frac{\frac{g}{\theta_0} \frac{\partial \theta}{\partial z}}{\left(\frac{\partial u}{\partial z} \right)^2}, \quad (17)$$

which provides a qualitatively convenient way to visualize linear instabilities in the flow, in figure 3.6. In the no inversion case (fig 3.6a) linear instabilities, as indicated by $Ri_g < 1/4$ contour, appear first near the bottom of the overturning isotherms and gradually expand and move up to encompass the entire region of overturning isotherms. The high inversion case (fig 3.6d) shows the same pattern of instabilities characteristic of the no inversion case in addition to instabilities on the inversion itself that are more clearly shown in the medium inversion case (fig 3.6c). In the medium inversion case instabilities on the inversion first appear at the bottom and then the top of the perturbation area where isotherms on top and bottom of the inversion are being displaced upwards and downwards respectively. Gradually the instabilities on the bottom of this area expand downwards and downstream as the stagnation zone grows. In contrast to the three other cases, instabilities in the low inversion case (fig 6b) first appear on the upstream side of

the hydraulic jump, where the entire inversion begins overturning, as in a breaking interfacial wave. The large amount of turbulence and instabilities in this region propagate downstream, gradually mixing out the well defined inversion layer in the region of the hydraulic jump on the lee slope. The inversion layer is still, however, well defined downstream from the jump.

Vertical profiles of the horizontal velocity and buoyancy, N^2 , are shown in figure 3.7 for the medium inversion case. Buoyancy profiles are calculated by taking the square of the Brunt-Vaisala frequency (2). In using these profiles we have been careful to avoid the top of lee surface jet by centering the upstream inversion height midway in the profiles and constraining the profiles from 600 m above the inversion to 600 m below the inversion. Any values of the buoyancy and velocity profile which included part of the surface jet were replaced with values from immediately above the surface jet, thus ensuring that the area of large shear production of TKE (see figure 3.5b) at the top of the lee surface jet is not included in our analysis. We solve the Taylor-Goldstein equation (15) numerically and search for normal mode solutions with the form

$$\varphi(y, z, t) = \hat{\psi}(z) \exp[i\alpha(x - ct)] \quad (18)$$

where α and c are the streamwise wavenumber and phase velocity.

The profiles are shown at 60, 90 at 100 min, which covers the time when instability on the inversion appears and begins to grow (see figure 3.3). Stable profiles are solid, while dashed lines indicate that the profile is unstable with respect to small perturbations, and that the real part of the normal mode solution grows with time. In the first two time periods presented some of the profiles are characterized by a spreading of the inversion over a larger depth and a monotonic increase or decrease in the horizontal velocity over the inversion layer. In the last plot, at 100 min, the dashed profile indicates the flow has gone unstable with respect to linear perturbations. We note that the choice of a critical growth rate derived from the Taylor Goldstein equation is somewhat arbitrary, since the Reynolds number separating positive real growth rates from those that are dampened out due to viscosity is somewhat hard to define in this situation. Regardless, the frozen flow hypothesis serves as a useful qualitative tool to differentiate between instabilities that can be expected to grow from those that are dampened out by viscosity. Returning to the unstable profile at $t = 100$ min, we see that the stable stratification in the inversion layer

(at the center of the profile) is greatly reduced while stable stratification remains above and below what was the inversion layer. Importantly, a horizontal velocity defect has appeared in the layer, with the horizontal velocity falling to zero.

f. Momentum budget and instability initiation

Change in horizontal velocity and stratification for the medium inversion case can be discerned using the horizontal (figure 3.8a) and vertical (figure 3.8b) momentum budget. Figure 3.8a reveals that the sum of the advection and pressure gradient term in the horizontal momentum budget act to create horizontal velocity defect in the perturbation on the inversion. This is due to the nonlinear advection term increasing with respect to the horizontal pressure gradient force. In the vertical momentum budget (figure 3.8b), both nonlinear advection and vertical pressure gradient force act to perturb flow on the upper/lower part on the inversion up/down respectively. Thus, the combined action of pressure gradient and nonlinear advection caused by IGWs in the lower layer act to create a pocket of quiescent air in the inversion layer which is gradually pulled apart and becomes unstable. The instabilities are followed by shear produced turbulence (as shown in figure 3.3) and an extension of the stagnation zone downstream with time. Since the stagnation zone essentially provides an upper lid on the lee surface jet, the lee surface jet is forced to continue further downstream until the adverse horizontal pressure gradient become large enough to lift the surface jet over the first rotor.

Thus far we have discarded the barotropic mode transition and hydrostatic IGW trapping as mechanisms for the formation of downslope windstorms in the medium inversion case. We have shown the importance of instability mechanisms on the inversion. We now turn to a different series of experiments to elucidate the role of nonlinear IGW breaking and further explore the mechanism by which perturbations on the inversion may destabilize.

3.4. Mountain height results

a. Overview and IGW breaking

To further explore the causes of the instabilities on the inversion we ran a series of experiments with varied mountain height. By reducing the mountain height, we reduce the nonlinearity parameter, Nh/ν and can isolate the effects of IGW breaking from those of inversion instabilities. These cases were conducted both without an inversion and with an inversion whose inversion strength, $\Delta\theta = 8$ K, and inversion height, $z_i = 1800$ m, were the same as the medium inversion case presented above. The experiments in this section were run at 25m resolution with the same domain size as those above. No significant differences between similar simulations run at 25 m resolution and those run at 15 m resolution were noted. A summary of the cases is presented in table 3.2, and results from case with $h_{min} = 200$ m ($Nh/\nu = 0.5$) and $h_{min} = 450$ m ($Nh/\nu = 0.9$) with and without an inversion are presented in figure 3.9. As expected, in the cases without an inversion, only large mountains produce downslope windstorms. The $h_{min} = 600$ m, with $Nh/\nu = 1.2$, case shows internal gravity wave breaking (see figure 3.2a) while all other cases with $Nh/\nu < 1$ do not (fig 3.9c). This result is consistent with the notion of Nh/ν as a measure of the nonlinearity of the response (Clark and Peltier, 1977). However, the mountain height threshold for breaking with an inversion present is significantly lower than it is for cases lacking an inversion. In fact, for inversion cases all experiments with Nh/ν greater than or equal to 0.7 result in a downslope windstorm with significant lee extent (fig 3.9b). For the inversion case with $h_{min} = 200$ m and $Nh/\nu = 0.5$ (figure 3.9a) a perturbation develops on the inversion but does not lead to a spontaneously growing instability; neither a stagnation zone nor a jet forms. The inversion cases with $Nh/\nu = 0.7$ and 0.9 (fig 3.9b) bear further examination since the nonlinearity parameter, Nh/ν , is less than 1 indicating that the IGW should not overturn and create a self-induced stagnation zone (Lin and Wang, 1996). Similar to the medium inversion case presented in figure 3.3, none of these cases exhibit a subcritical to supercritical transition of the shallow water mode.

Patterns of TKE and gradient Richardson number were similar in all the inversion breaking cases (not shown) to those presented before (see figure 3.5 and figure 3.6, respectively). Growth of the stagnation zone by shear production of TKE is similar in all of the inversion downslope windstorms cases as to the medium inversion height case shown in figure 3.5. Shear production of TKE is the dominant term in the TKE budget

and is largest along the interface of the upper edge of the surface jet and lower edge of the growing stagnation zone, where horizontal velocity gradients are highest.

b. IGW trapping

The role, if any, played by IGW trapping in determining the lee flow response can be discerned by examining the amount of KE aloft in vertically propagating hydrostatic IGW. Figure 3.10 shows the maximum KE in the vertical velocity field at any point above the inversion and the ridge for all the experiments as a function of Nh/ν . For cases with and without inversions the amount of KE aloft increases as mountain height increases due to the larger amplitude forcing at the surface. However low mountain height cases with inversions actually have more KE aloft in the IGW response than the no inversion cases, which indicates that the lower layer IGW perturbations on the inversion layer effectively act as a more efficient forcing for the vertically propagating IGW in the upper layer than the mountain itself. At $Nh/\nu = 1.2$ the IGW response in the no inversion cases is much more energetic than it is in the inversion case, consistent with the notion of trapping of IGW energy by the inversion. The $Nh/\nu = 0.7$ and $Nh/\nu = 0.9$ inversion cases, however, which do not exhibit significant IGW trapping, also have downslope windstorms. Thus trapping of IGW energy by the inversion is unlikely to be the dominant mechanism for presence or absence of downslope windstorms in these cases.

Inversion instabilities

In figure 3.11 we present vertical profiles of buoyancy and horizontal velocity for the $Nh/\nu = 0.5$ and $Nh/\nu = 0.9$ inversion cases. A similar pattern of instability occurs in the $Nh/\nu = 0.9$ as in the previously presented $Nh/\nu = 1.2$ case (figure 3.7). Profiles in the first two times of the $Nh/\nu = 0.9$ case are characterized by a monotonic increase or decrease in horizontal wind velocity across the inversion, and the smearing out of the inversion over a larger depth. Profiles in the $Nh/\nu = 0.5$ case have a much smaller horizontal velocity defect, which doesn't fall to zero, and the perturbation on the inversion layer never actually becomes neutrally stable. The unstable profile at $t = 130$ min in the $Nh/\nu = 0.9$ case, indicated by the dashed line, shows that stable stratification initially present in the

inversion layer has become neutrally stratified while the horizontal velocity has fallen to zero.

To further explore the instabilities associated with the various profiles of buoyancy and velocity presented in figure 3.11 we ran a series of experiments with no topography or forcing outside of initial perturbations to initiate turbulence. We initialized these experiments with the profiles presented in figure 3.12, which were based on the evolution of the $Nh/\nu = 0.9$ profiles presented in figure 3.11. The velocity profiles are characterized by increasing shear over the inversion layer, decreasing shear over the inversion layer and a horizontal velocity defect in the inversion layer. The temperature profiles represent a strong intact inversion, a diffuse inversion spread out over greater depth, and an inversion that has been pulled apart to create two smaller upper and lower inversions with an unstable layer in the middle. All of the velocity profiles satisfy Fjortoft's theorem for the minimum requirement of instabilities to be present, namely that $v_{zz}(z) * (v(z) - v_i) < 0$ somewhere flow, where v_{zz} is the second derivative of horizontal velocity with respect to height and v_i is the velocity at the inflection point. Due the increased shear all of the experiments with the horizontal velocity defect in the middle of the inversion developed instabilities, and lack of stable stratification in all of the experiments with split inversion layer also promoted instability. The positive and negative shear cases were only unstable with the split inversion temperature profile, and the strongly stable and weakly stable inversion cases were only unstable with the horizontal velocity defect profile. For these cases, one of two requirements must be met for the instability to occur and grow spontaneously: the inversion must be pulled apart to form a neutrally stable layer in between an upper and lower inversion, or strong shear in the form of a large horizontal velocity defect must be present.

c. *Momentum budget*

Momentum budget analysis reveals the causes of instability initiation on the inversion. Advection and pressure gradient oppose each other in the horizontal momentum budget in the perturbation on the inversion. For smaller mountain heights (figure 3.13a) the horizontal pressure gradient term is able to match the nonlinear advection term and prevent the horizontal velocity defect from dropping to zero. For

larger mountain heights (figure 3.13b), as in the $h_{\text{mtn}} = 450\text{m}$ case shown in figure 3.9, nonlinear advection increases relative to the horizontal pressure gradient force in the perturbation on the inversion, creating a pocket of stagnant air. In the vertical momentum budget (figure 3.14) both vertical pressure gradient and nonlinear advection act to pull apart the inversion, by creating a zone of negative vertical velocity on the bottom of the perturbation zone, and positive vertical velocity on the top of the perturbation zone. The pressure gradient term is larger than the nonlinear advection term. For smaller mountain heights (figure 3.14a) the combined action of the two is not enough to pull apart the inversion and force the perturbation to grow, while for larger mountain heights (figure 3.14b) the combined effect of nonlinear advection and pressure gradient force acts to pull apart the inversion and form a layer of neutrally stratified air with a strong horizontal velocity defect, both of which are crucial in initiating instabilities on the inversion. Shear production on this instabilities then grow the stagnation zone and force the lee slope jet beneath. These effects can occur in inversion cases even when $Nh/v < 1$, but do not occur for the same forcing in cases without inversions.

3.5 Conclusions

The focus of this study was twofold: determine the applicability of the RGSW framework and nonlinear IGW breaking to various downslope windstorm scenarios, and explore the instability mechanisms of inversion based downslope windstorms. We have explored and discarded the following mechanisms for the generation of downslope windstorms in the medium inversion height experiments presented in this study:

- 1) Trapping of hydrostatic IGW energy in the lower layer by the inversion.
- 2) Barotropic transition of the interfacial wave on the inversion.
- 3) Nonlinear IGW breaking and self induced stagnation zone.

This research proposes a new mechanism of downslope windstorms based on instability mechanisms on the inversion itself and associated coupling of the stagnation zone with the lee surface jet.

Our initial set of experiments focused on four cases: low inversion, medium inversion, high inversion and no inversion. The no inversion case resulted in IGW breaking and the creation of a stagnation zone. This case showed a series of trapped lee

wave rotors. In the low inversion case the trapped lee waves were essentially absent from the flow and the downslope windstorm and stagnation zone extends far down the slope. The medium inversion case the mechanism for generation of the lee jet was shown to be result of mountain wave induced instabilities on the inversion. The pocket of neutrally stratified, stagnant air in the inversion grows spontaneously by shear production of TKE to create a large stagnation zone downstream. The lee jet is forced beneath the stagnation zone, resulting in a long lee slope jet. Both the medium inversion and high inversion cases shows some lee waves and reduced IGW energy aloft. Flow in the high inversion case is qualitatively similar to the no inversion case. The significant reduction of IGW energy aloft for high inversion case versus the no inversion case was not consistent with the trapping of IGW aloft as being the cause of the downslope windstorms. All cases with inversions show more turbulence near the surface than the no inversion case. The low inversion case especially so, largely due to increased shear production along the interface between the surface jet and stagnation zone. This may provide a mechanism for the significant gustiness observed in many downslope windstorms (Belusic et al., 2007).

Despite the similarity of all three inversion cases, only the low inversion case has a control point for interfacial waves at the ridge crest indicating a two layer behavior with transcritical flow. The barotropic Froude number in the medium and high case never exceeds unity, indicating that interfacial waves on the inversion may propagate upstream and downstream everywhere in this flow. A further objection to a simplified RGSW framework to describe the medium and high inversion cases is that the lee jet is not capped by the inversion, but rather the inversion remains above the stagnation zone. This stands in contrast to other recent modeling experiments (Jiang et al., 2007 and Vosper, 2004) where the selection of a proper inversion strength for the flow over the lee slope is more well defined. Furthermore, we note that the horizontal length scales associated with these flows are of the same order of magnitude as the vertical length scales, which combined with the lack of control point, indicates that barotropic transition of the interface mode is not important.

We then presented a series of experiments, with an inversion at the medium height and without an inversion in which we varied the mountain height across the parameter range $Nh/v = 0.4-1.2$ to clarify the role of IGW breaking in the lee slope flow.

Downslope windstorms occurred for inversion cases even when $Nh/\nu < 1.0$, indicating that nonlinear IGW breaking was not the dynamical reason for the lee slope jet. It was shown instead that pressure gradient forces and nonlinear advection associated with the flow response to the topographical perturbation act to split the inversion and slow the horizontal flow, creating a pocket of neutrally stratified stagnant air with an inversion and strong horizontal velocity gradients both above and below the pocket. This results in instabilities which spontaneously grow due to increased shear production, especially along the interface between the growing stagnation zone and the lee surface jet, the downstream extent of which is determined by being constrained beneath the stagnation zone.

The amount of IGW energy present aloft was not consistent with trapping of IGW energy by the inversion as being the cause of downslope windstorms in these experiments. None of the experiments achieved a transition of the barotropic mode over the ridge. Experiments with $Nh/\nu < 1.0$ resulted in downslope windstorms counter to notions of IGW breaking. We thus discarded three out of the four previously suggested mechanisms which may be important in explaining the flow behavior: trapping of hydrostatic IGW energy by the inversion, supercritical transition of the barotropic mode, and nonlinear IGW breaking, leaving only instability mechanisms on the inversion as an explanation for the flow behavior in the medium inversion cases with $Nh/\nu < 1$. Pressure gradient and nonlinear advection generally act to create conditions on the inversion in which instabilities may spontaneously occur and grow. Once turbulence is initiated, the stagnation region grows due to shear production along the bottom of the stagnation zone and top of the lee jet. The entire upstream flow from the surface up to inversion is constrained between the mountain and the stagnation zone, resulting in high surface velocities on the lee slope. The inversion instability mechanism is relevant for forecasters because it suggests a scenario in which downslope windstorms may occur when neither a barotropic transition nor IGW breaking are predicted.

Acknowledgements: We are pleased to acknowledge the super-computer time provided by the National Center by Atmospheric Research, which is funded by the National Science Foundation. This research was funded by the National Science Foundation under

grant ATM-0527790. We also wish to thank the anonymous reviewers for their help in strengthening the manuscript.

Figures

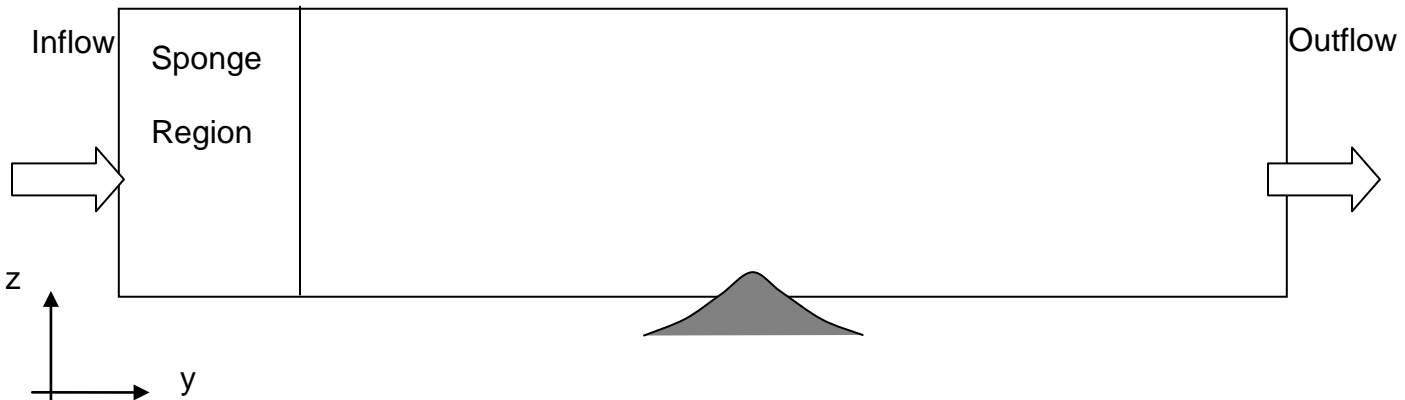


Figure 3.1. Schematic showing the channel flow configuration used in the simulations.

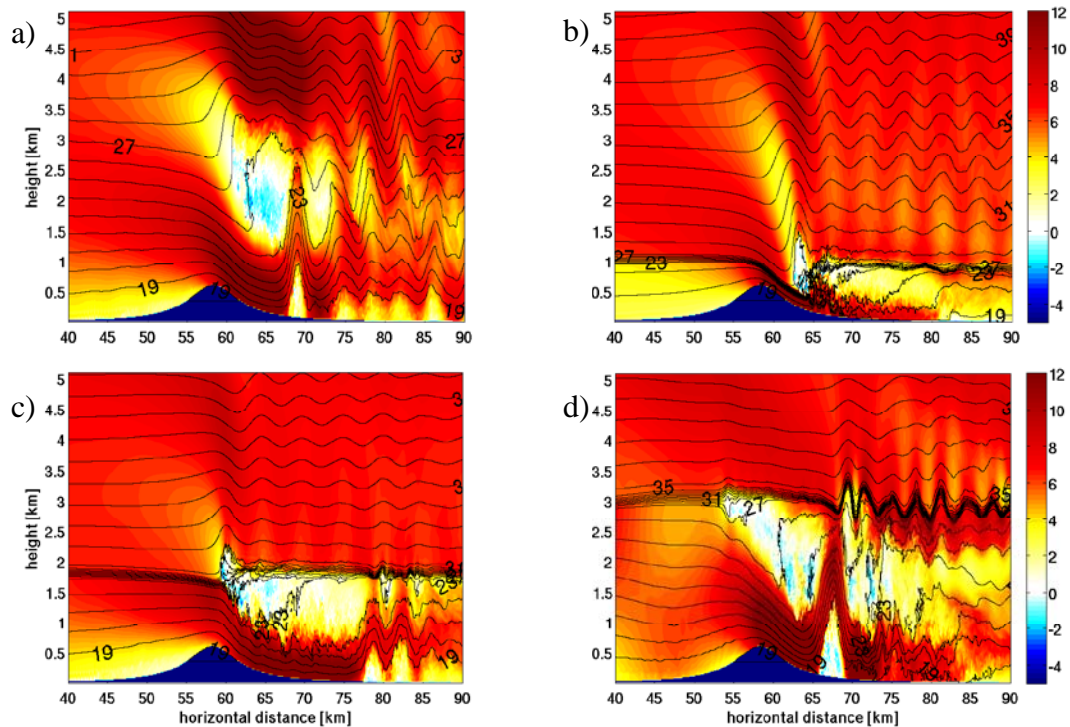


Figure 3.2. Close up view of streamwise velocity (shading in ms^{-1}) and potential temperature (lines of constant $^{\circ}\text{C}$) for the a) no inversion case at $t = 360$ min, b) low inversion case at $t = 120$ min c) medium inversion case at $t = 360$ min, and d) high inversion case at $t = 200$ min.

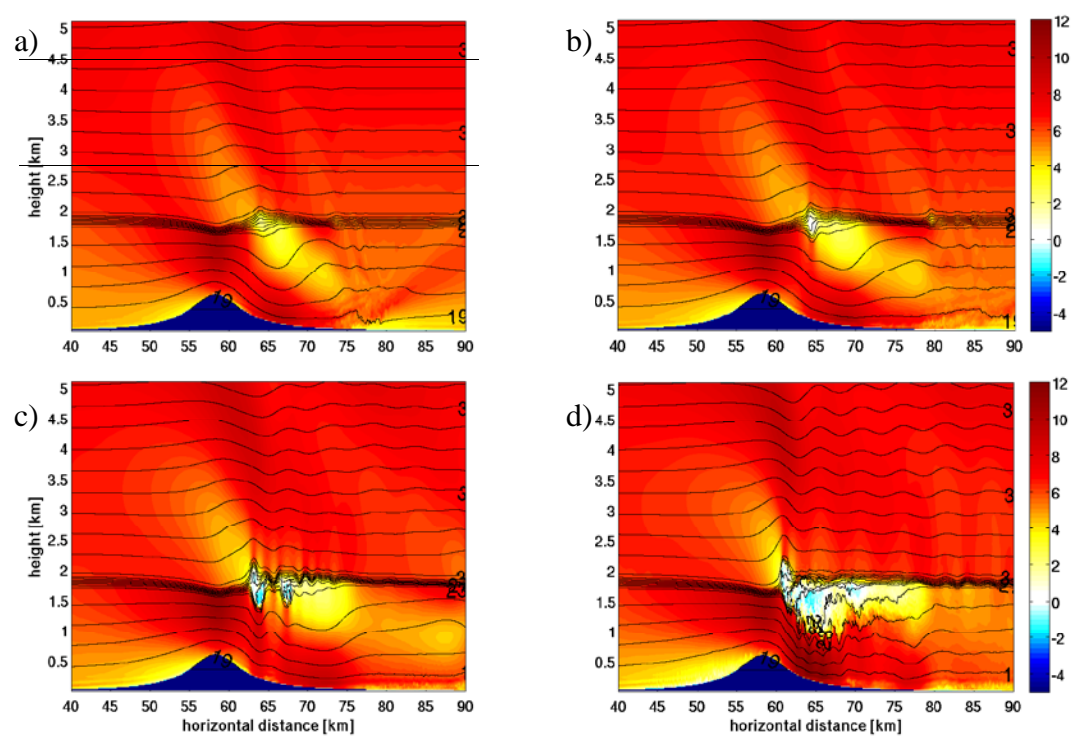


Figure 3.3. Close up view of streamwise velocity (shading in ms^{-1}) and potential temperature (lines of constant $^{\circ}\text{C}$) for the medium inversion case at a) $t = 60$ min, b) $t = 90$ min, c) $t = 150$ min, and d) $t = 240$ min.

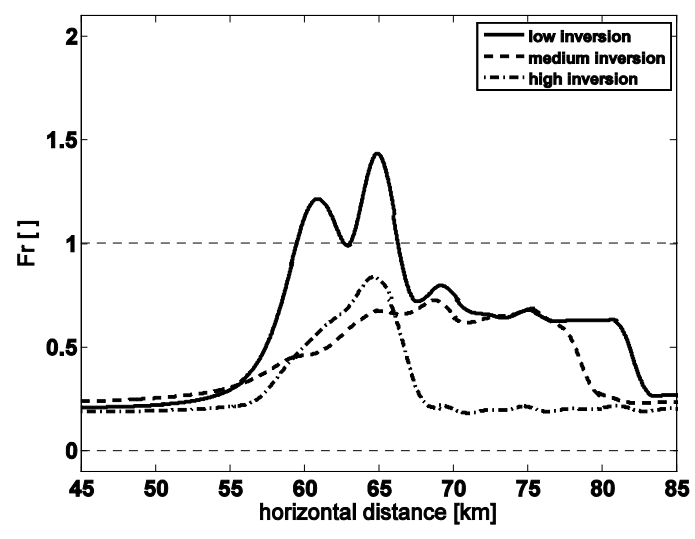


Figure 3.4. Shallow water mode Froude number versus streamwise distance for the low inversion, medium inversion and high inversion cases at the times presented in figure 3.2.

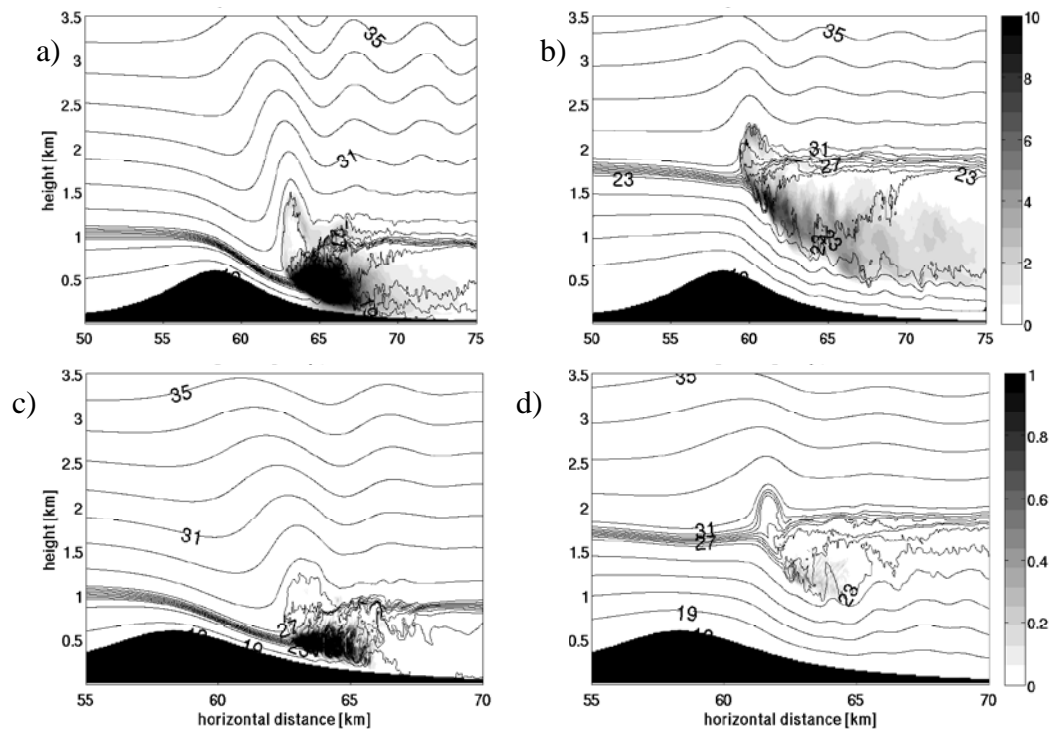


Figure 3.5. Close up view of average TKE (shading in m^2s^{-2}) and potential temperature (lines of constant $^{\circ}\text{C}$) for the a) low inversion case at $t = 120$ min and b) medium inversion case at $t = 360$ min and TKE budget terms of shear production of TKE (shading in m^2s^{-3}) and potential temperature (lines of constant $^{\circ}\text{C}$) for the c) low inversion case at $t = 35$ min and d) medium inversion case at $t = 210$ min.

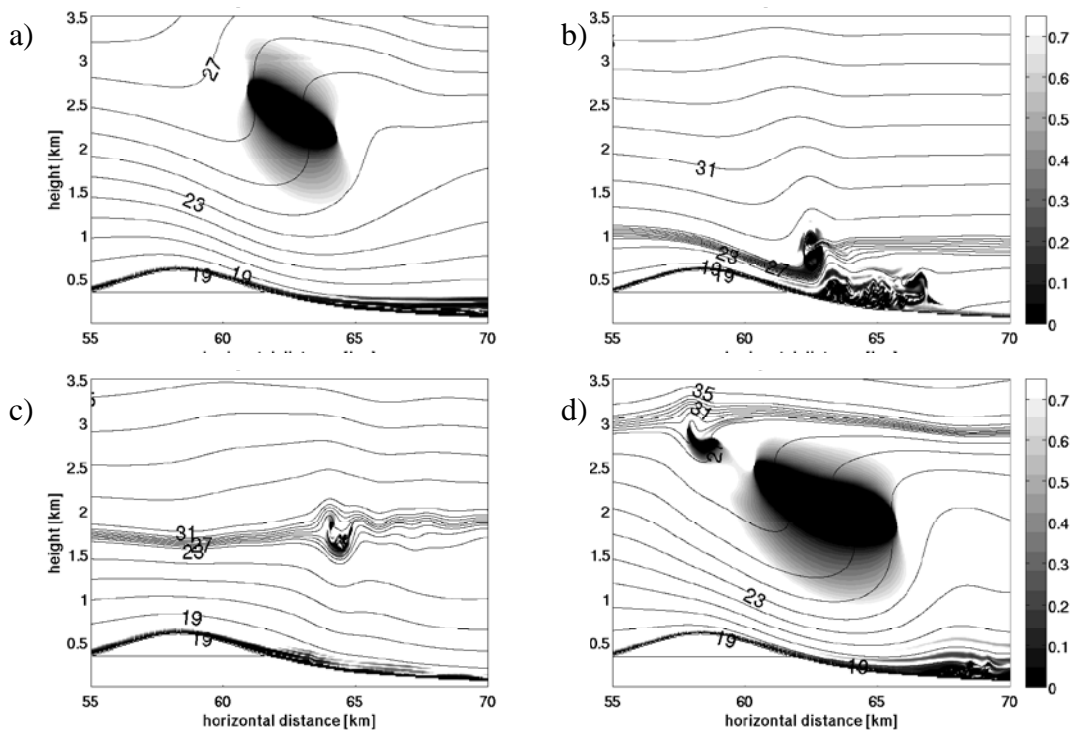


Figure 3.6. Close up view of Richardson number and potential temperature (lines of constant $^{\circ}\text{C}$) for the a) no inversion case at $t = 150$ min, b) low inversion case at $t = 20$ min c) medium inversion case at $t = 110$ min, and d) high inversion case at $t = 100$ min.

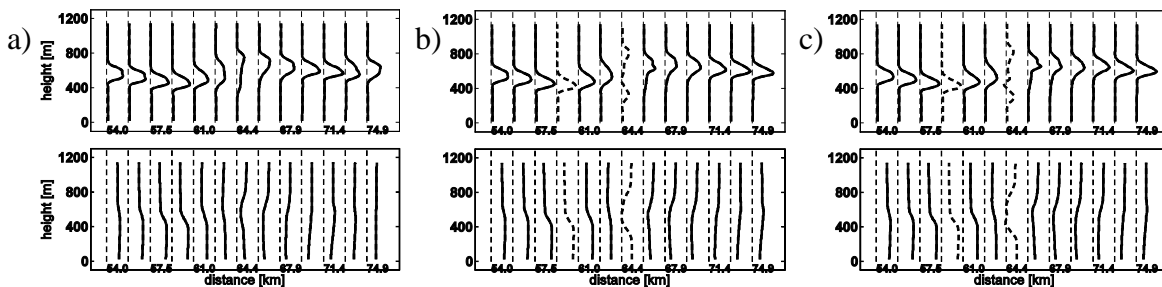


Figure 3.7. Vertical profiles of buoyancy (s^{-2}) (top row) and streamwise velocity (ms^{-1}) (bottom row) as a function of height at various times used in the instability analysis for the medium inversion case at a) $t = 60$ min, b) $t = 90$ min and c) $t = 100$ min (stable profiles are solid, unstable profiles are dashed).

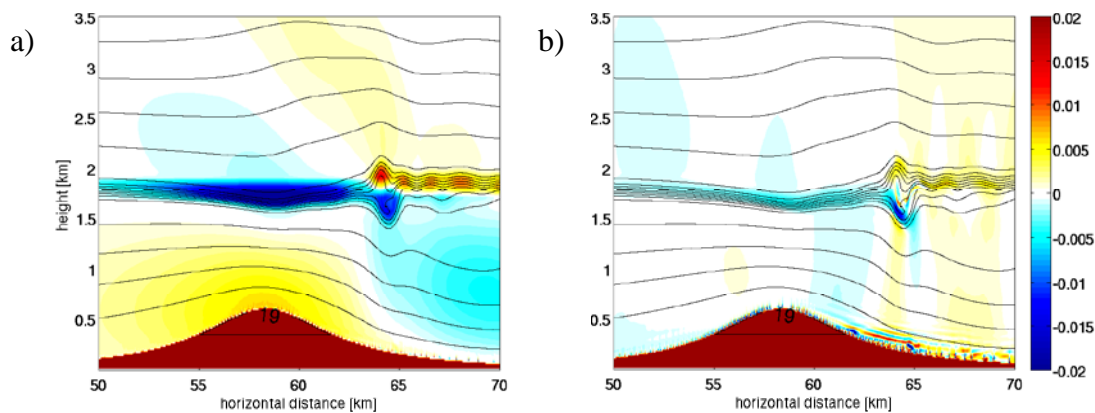


Figure 3.8. Close up view of sum of momentum budget terms of advection and pressure gradient (shading in ms^{-2}) and potential temperature (lines of constant $^{\circ}\text{C}$) for the medium inversion case at $t = 105$ min for a) the horizontal momentum budget and b) the vertical momentum budget.

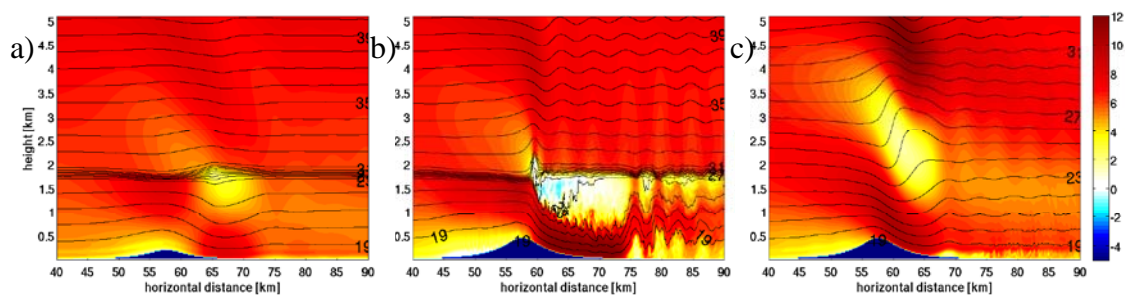


Figure 3.9. Close up view of streamwise velocity (shading in ms^{-1}) and potential temperature (lines of constant $^{\circ}\text{C}$) for the a) inversion $Nh/\nu = 0.4$ case at $t = 240$ min, b) no inversion $Nh/\nu = 0.9$ case at $t = 420$ min and c) inversion $Nh/\nu = 0.9$ case at $t = 360$ min.

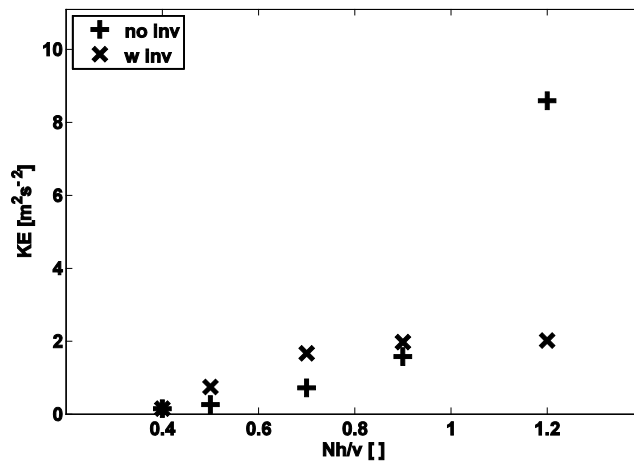


Figure 3.10. IGW KE aloft versus Nh/ν for the experiments listed in Table 3.2.

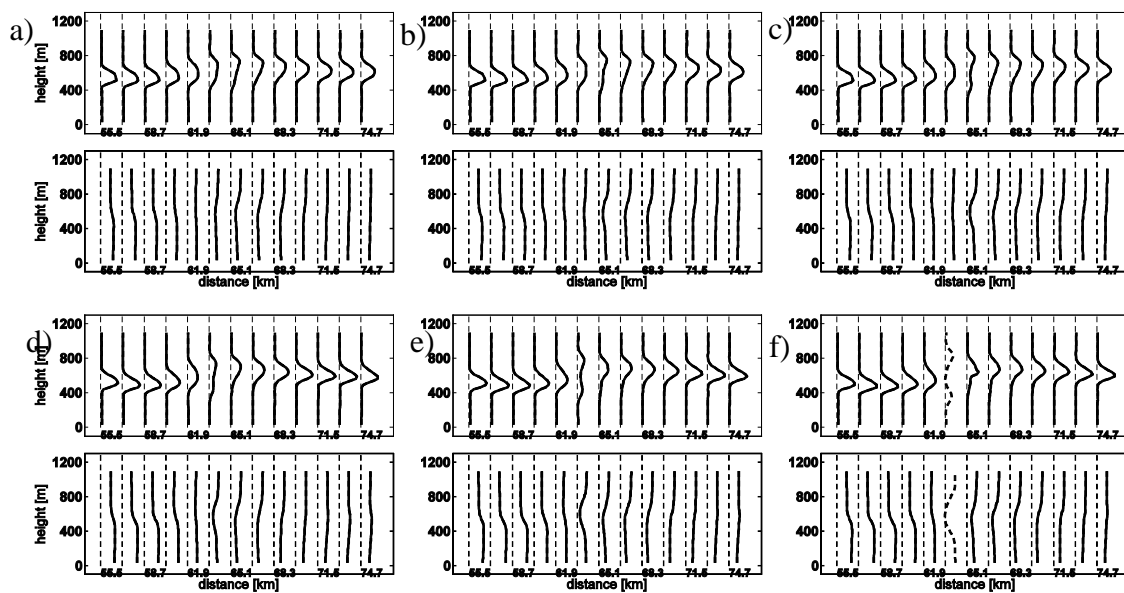


Figure 3.11. Vertical profiles of buoyancy (s^2) (top rows) and streamwise velocity (ms^{-1}) (bottom rows) as a function of height at various times for the inversion $Nh/\nu = 0.4$ case at a) $t = 180$ min), b) $t = 240$ min), and c) $t = 300$ min), and inversion $Nh/\nu = 0.9$ case d) $t = 80$ min), e) $t = 110$ min), and f) $t = 130$ min).

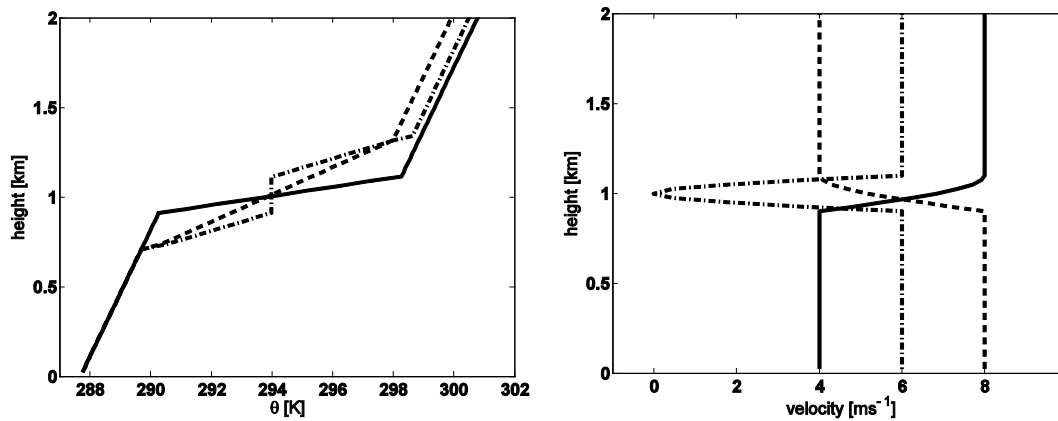


Figure 3.12. Vertical profiles of a) potential temperature (K) and b) streamwise velocity (ms⁻¹) as a function of height used to initialize 3-D instability simulations.

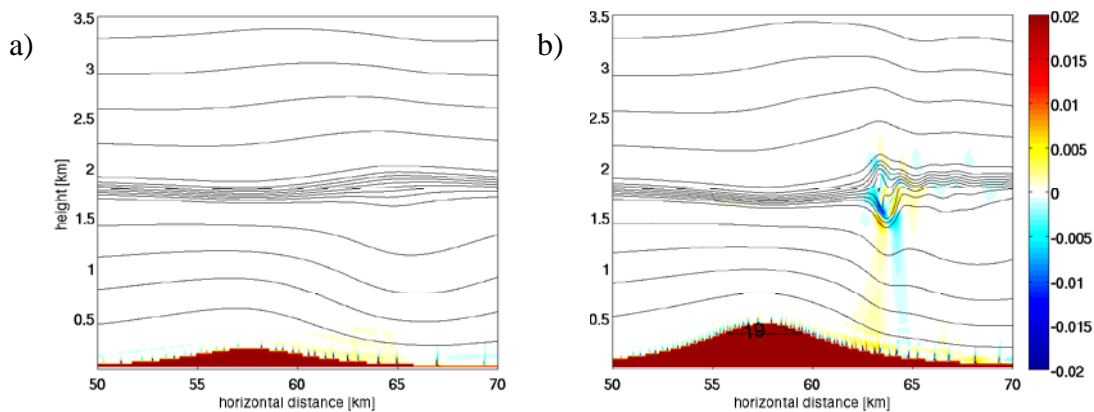


Figure 3.13. Close up view of sum of horizontal momentum budget terms of advection and pressure gradient (shading in ms⁻²) and potential temperature (lines of constant °C) for the a) inversion $Nh/\nu = 0.4$ case at $t = 180$ min, and b) inversion $Nh/\nu = 0.9$ case at $t = 140$ min.

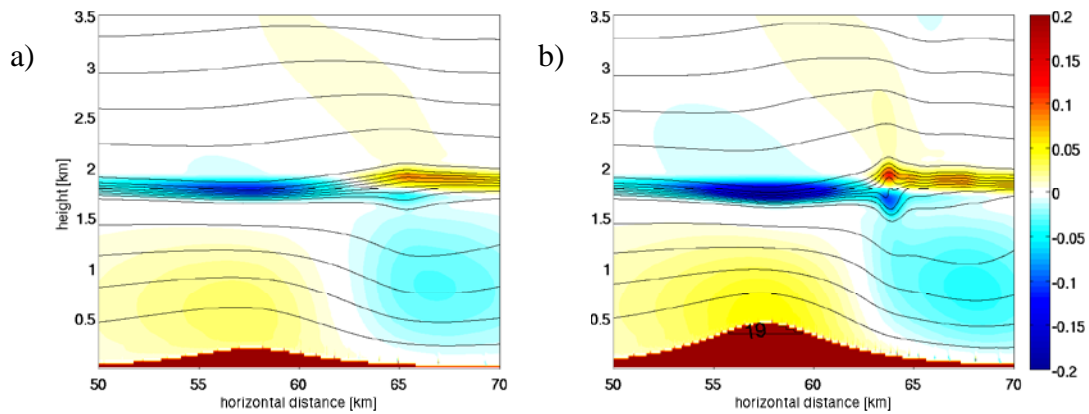


Figure 3.14. Close up view of sum of vertical momentum budget terms of advection and pressure gradient (shading in ms^{-2}) and potential temperature (lines of constant $^{\circ}\text{C}$) for the a) inversion $Nh/\nu = 0.4$ case at $t = 240$ min, and b) inversion $Nh/\nu = 0.9$ case at $t = 120$ min.

Tables

	$z_i(m)$	$\Delta\theta$ (K)	% KE aloft
No inversion	-	-	100
Low inversion	0900	8	59
Medium inversion	1800	8	24
High inversion	3000	8	27

Table 3.1: List of inversion height experiments.

h_{mtn} (m)	Nh/ν	Inversion present	Downslope windstorm
200	0.4	Y	Y
250	0.5	Y	Y
350	0.7	Y	Y
450	0.9	Y	Y
600	1.2	Y	Y
200	0.4	N	N
250	0.5	N	N
350	0.7	N	N
450	0.9	N	N
600	1.2	N	Y

Table 3.2: List of mountain height experiments.

Slope flow-downslope windstorm interaction
over a low 2-D ridge

Craig M. Smith and Eric D. Skillingstad

College of Oceanic and Atmospheric Sciences

104 COAS Admin Bldg

Oregon State University, Corvallis, OR 97331-5503, USA

In preparation

Abstract

The influence of diurnal variations of surface heat fluxes on downslope windstorms are explored using observations and an eddy resolving numerical model. Observations made on the Falkland Islands (Mobbs et. al, 2005) show that downslope windstorms may preferentially occur in early morning even without synoptic scale changes in atmospheric structure. Most windstorms on the Falkland Islands generally have a short jet length, while those windstorms with a fairly long lee extent are much rarer and often occur in conjunction with a strong low level inversion.

Large eddy simulations of a 2-D ridge with a simplified surface heating and cooling regime show a propensity for downslope windstorms to occur in the presence of surface cooling. For low inversions surface heating is shown to mix out lee rotors, resulting in a significantly shortened lee jet. This is primarily a result of heating on the lee slope, while transport of turbulence generated upstream of the ridge over the ridge is fairly small. Flow velocities in the jet far downstream for the low inversion case can largely be construed as a combination of a hydraulically controlled downslope windstorm and katabatic flow. For the medium inversion heights upstream surface heating and turbulent transport over the ridge play a crucial role in preventing communication of the topographic disturbance to the inversion layer. The application of surface cooling results in the restratification of the surface boundary layer, and as perturbations on the inversion increase instabilities on the inversion may spontaneously grow and form a stagnation zone with significant downstream extent. The lee jet is forced beneath the stagnation zone resulting in strong wind far away from the ridge which is not a result of katabatic contributions to the jet.

4.1 Introduction

Despite the widespread occurrence of downslope windstorms in the lee of mountain ridges very little is known about the extent to which they may be affected by surface heat fluxes on diurnal time scales. As their onset and decay have generally been attributed to synoptic scale processes such as frontal passage or the strengthening and weakening of the upper level jet stream, there have been only been a few studies on preferential starting and cessation times for downslope windstorms. Those which have been done have focused on the lee of three major mountain ranges: the Sierra Nevadas, the Rocky Mountains and the Andes.

In the lee of the Sierra Nevada mountains downslope windstorms tend to occur in the afternoon (Jiang and Doyle, 2008, and Zhong et. al, 2008). Zhong et. al (2008) attribute the forcing mechanism for Washoe Zephyr, as this particular windstorm is known as, to a regional scale pressure gradient induced by asymmetric heating of the ground in the San Joaquin and Sacramento River Valleys to the West and the Great Basin to the East. They note that the Zephyr can occur without westerly flow aloft and downward mixing of momentum. Jiang and Doyle (2008) meanwhile attribute the diurnal variation in strong surface westerly events to a multiscale effect largely based on a mixing out of the Owens valley cold pool. Observations from Argentina (Seluchi et. al, 2003 and Norte, 1988) also show that downslope windstorms in the lee of the Andes in Argentina tend to start around midday or early afternoon, and last until night. They suggest that vertical mixing induced by surface heating helps mix out the subsidence inversion and allow the windstorm to occur. The Rocky Mountains, in contrast to the two previously mentioned cases, tend to preferentially have downslope windstorms that occur between midnight and 7 AM in the morning (Miller et. al, 1974).

Modeling studies have also attempted to address the modulation of mountain wave systems by surface heat fluxes but have primarily focused on nonhydrostatic trapped lee waves or the IGW breaking regime. Examples of the former include Doyle and Durran (2002), who explored the effect of lee slope heating on the lee wave rotors. They showed that even relatively weak surface heating can result in significantly reduced rotor

strength, increased rotor height, and increase in near surface TKE. Jiang et. al (2006) and Smith et. al (2006) also examine the absorption of trapped lee waves by the atmospheric boundary layer downstream of a ridge. They show that the absorption of wave energy by the boundary layer can be increased by stagnant near surface layers and that stable boundary layers are more efficient in absorbing trapped lee waves than turbulent neutrally stratified boundary layers.

The Poulos et. al (2000) study looked at the interaction of katabatic flows and mountain waves, both linear and nonlinear. In some cases mountain waves were not strong enough to inhibit the usual morning and evening transitions generally seen in slope flows. In highly nonlinear cases the mountain wave response was strong enough to scour out the katabatic flow entirely. Since the effective Brunt-Vaisala frequency, N ,

$$N = \sqrt{\frac{g}{\theta_0} \frac{\partial \theta}{\partial z}}, \quad (1)$$

where g is acceleration due to gravity, θ is the potential temperature, and θ_0 is a reference potential temperature, can be affected by surface heat fluxes, they suggest that the separation point of the first rotor on the lee slope varies as a function of the non-dimensional mountain height,

$$\hat{h} = \frac{Nh}{v} \quad (2)$$

where h is the ridge height, and v is the cross-ridge velocity.

Ying and Baopu (1993) also studied the effects of diurnal heat fluxes on IGW breaking over a relatively low 2-D ridge. They note the effect of boundary stability in modulating wind speed at the top of the boundary layer and flow blocking upstream of the ridge. The convective boundary layer reduces the dynamical forcing of the flow leading to smaller mountain wave amplitude and maximum wind speeds, while for the stable morning boundary layer the maximum downslope windspeed was decreased due to a decrease in the upstream windspeed from flow blocking. More recently Jiang and Doyle (2008) modeled the effect of surface heating on downslope windstorms using idealized conditions with a double ridge and valley situation. They showed that surface heating resulted in a stronger lee side jet due to increased cross-mountain pressure

gradient and a mixing out of the stagnant valley cold pool. Finally, Smith and Skillingstad (2009) studied the effect of surface heat fluxes on downslope windstorms over a low 2-D ridge induced by IGW breaking. They found that strong surface heat fluxes dramatically reduce lee rotor structure, while surface cooling leads to a strongly stratified lee jet which is lofted over and caps the rotors. The enhanced stable stratification in the flow capping the rotors lead to a more persistent rotor structure further downstream of the ridge than would otherwise be found.

While previous work has studied the effect of surface heat fluxes on linear and nonlinear IGW systems or trapped lee wave systems, no observational or modeling studies have focused on the influence of surface heat fluxes on downslope windstorms induced by either a subcritical to supercritical transition of the barotropic interfacial mode, or the recently proposed mountain wave induced inversion instability mechanism (Smith and Skillingstad, 2010). The focus of this study is two-fold:

1) Examine recent observations of downslope windstorms over the Falkland Islands (Mobbs et. al, 2005) for evidence of diurnal variation in downslope windstorm behavior, including preferred onset and cessation times, and modulation of lee slope jet length with respect to time of day.

2) Examine the effects of surface heat fluxes on downslope windstorms over a simplified 2-D ridge using an eddy resolving simulation for two different flow regimes: transition of the reduced gravity shallow water (RGSW) barotropic mode, and mountain wave induced inversion instability model.

The paper is structured as follows. The Falkland Islands data set is analyzed in Section 2. In Section 3 a description of the large eddy simulation (LES) model is presented along with an outline of the experiments performed in our study. Results for low inversion and medium height cases are presented along with experiments used to discern katabatic contributions to lee flow behavior. Summary and conclusions are given in Section 4.

4.2 Observations of downslope windstorms on the Falkland Islands

The data set of Mobbs et. al (2005) taken on the Falkland Islands was chosen because of the intense turbulent episodes which occur at the Mount Pleasant Airfield, a

few kilometers WSW of station #5 (figure 4.1). From the data set we selected three stations: station #24, upstream of the ridge for northerly flow, and two stations (#5 and #1) downstream from the ridge for northerly flow in order of increasing distance from the slope. Surface wind velocity was collected at these stations from November 2000 to October 2001 and averaged over 10 minute periods.

The diurnal variation of northerly wind events, defined as $v_{\text{northerly}} > 10 \text{ ms}^{-1}$ for the station downstream of the ridge, #5, and $v_{\text{northerly}} > 5 \text{ ms}^{-1}$ for the station upstream of the ridge, #24 is shown in figure 4.2a. To obtain these values we sum all northerly wind events at a station by 10 minute intervals and then normalize by the total number of events per station to obtain the number of events per 10 minute interval as a percentage of the total number of events. We also present the diurnal variation of southerly wind events, defined as $v_{\text{southerly}} > 10 \text{ ms}^{-1}$ for the station downstream of the ridge, #24, and $v_{\text{southerly}} > 5 \text{ ms}^{-1}$ for the station upstream of the ridge, #5, is shown in figure 4.2b. All the stations show a propensity for southerly and northerly wind events to occur in early afternoon. The occurrence of high wind events on both sides of the ridge for northerly and southerly events during afternoon is most likely due to downward mixing of momentum from aloft as the boundary layer height increases from surface heating. However, northerly wind events at the downstream station, #5, also tend to occur in the middle of the night, with no associated increase in northerly wind events for the upstream station, indicating a preferential speedup of the flow from the upstream side of the ridge to the downstream side of the ridge. The presence of Mt Simon to the North of the main Wickham range on the East Falkland island may block of southerly events which would otherwise have impacted station #1.

We next examine the downstream extent of all northerly windstorm events by looking for events, defined as $v_{\text{northerly}} > 10 \text{ ms}^{-1}$, that occurred at station #5 alone, and stations #5 and #1 contemporaneously, indicated by the left and right bar in the figure 4.3, respectively. Approximately 74% of all windstorms only occur at the nearest downstream station and only 26% reach as far as the furthest downstream station.

The synoptic soundings, taken downstream of the ridge, were used to determine the extent to which inversion strength affected the presence of downslope windstorms and controlled jet length. The inversion strength, $\Delta\theta$, was found by searching for any

increase in temperature with height in the sounding. We looked only for inversions between 0.2 and 5 km in height, and only kept those that had a depth greater than 20m and a strength greater 0.1 K. Nearby inversions which were separated by stable layers of less than 100m depth were combined. In soundings with multiple well separated inversions only the strongest was kept. Since ridge top velocity, v_{rt} , was found to be very important in determining the existence of any downslope windstorm, we looked at only those soundings which were taken at the synoptic times in which the velocity at ridgetop level was greater than 5ms^{-1} . Each surface wind velocity measurement was correlated with the inversion strength of the nearest sounding, if any was present within two hours of the surface measurement taken. A few reservations about this correlation are noted here. First the soundings that satisfied our criteria were taken downstream of the ridge and thus the inversion strength and ridgetop velocity may not be representative of their upstream values. Second, since the upstream conditions are constantly changing it may not be appropriate to correlate all surface wind measurements taken within 2 hours for each sounding. The two hour window is arbitrary, and soundings taken at synoptic times are not ideal for this type of study.

Jets with limited downstream extent tend to be more common than those that extend as far downstream as station #1 (fig 4.3). Figure 4.4 stratifies these results by the inversion strength of the sounding associated with each surface wind velocity measurement constrained to occur within two hours of each other. Soundings with weak inversions tend to result in jet with limited downstream extent (figure 4.4a left column), which is consistent with the experiments of Smith and Skillingstad (2009), while soundings with strong inversions result in windstorms with significant downstream extent relatively more often (figure 4.4b right column) than those with weak inversions.

A few specific downslope windstorm events are useful in illustrating the type of behavior described above. The variation of surface wind velocity with time for the upstream, near downstream and far downstream surface stations for an event that occurred on the morning of 8/13/01 is presented in figure 4.5a. During this event wind velocity aloft did not change much (fig 4.6a) while before, and possibly during this event a strong inversion was present near 1 km. The low inversion present in the 8 am sounding is probably not representative of the upstream conditions, since the soundings

were taken downstream of the ridge, which is roughly 600m high. Strong northerly winds at station #5 began just after midnight local time and lasted until around 8 am. Very little secular change in the upstream surface station occurred during this time, and the strongest part of the jet did not extend fully downstream to station #1.

The event that occurred on the mornings of 1/27/01 (fig 4.5b) was characterized by a much longer jet, in which station #1 and station #5 both reported high northerly wind velocities from roughly midnight to 5 am, while the upstream station, #24, saw only a slight modulation of wind speed during this time. Conditions aloft during this time (fig 4.6b) were marked by large increase in northerly wind velocity and a very sharp increase in inversion strength near ridge top level. Since many downslope windstorm events occurred contemporaneously with a falling and strengthening of the inversion it is difficult to attribute the onset or decay of any event to changes in surface heat fluxes only, but observations from these two events are consistent with the following:

- 1) Downslope windstorms may begin and subside with little change evident in the ridgetop level wind velocity from the soundings. Some events were characterized by reduced northerly winds during daytime and strengthened northerly winds during nighttime. Many of these types of events occurred in conjunction with a lowering of inversion height.
- 2) An increase in low level inversion strength and increase in northerly wind velocity aloft can lead to an increase of jet length in the downstream direction, especially during nighttime.
- 3) The sampling frequency is not fine enough and the span of the observational record is not long enough to discern the effects of a changing inversion height and strength from that of surface heat fluxes.

4.3 Numerical experiments

a. Numerical setup

The inherent mesoscale nature of downslope windstorms lead to observations of phenomena in which attributions of direct forcings are not entirely free from ambiguity. To further explore the effect of surface heat fluxes on downslope windstorms we turn to numerical experiments of flow over a simplified low 2-D ridge. Experiments were

performed using a modified version of the LES model used in Smith and Skyllingstad (2010) and Smith and Skyllingstad (2009). This model is based on the Deardorff (1980) equation set, with the subgrid-scale model described by Ducros et. al (1996). Pressure in the model is calculated using a compressible pressure solver (Klemp and Wilhelmson, 1978). Terrain in the LES model is prescribed using a shaved cell approach described in Adcroft et. al (1997) and Steppeler et. al (2002). This approach was selected over the more commonly used terrain following coordinate methods to avoid problems with the LES filtering assumptions.

Simulations were conducted using a narrow channel domain with periodic boundaries in the cross slope and along slope direction (figure 4.7). We used a sponge layer in the along slope direction in the first 10 kilometers of the domain to return the flow to an unperturbed upstream condition (Bacmeister and Pierrehumbert, 1987). Further details of the simulations are presented in Smith and Skyllingstad (2010) and Smith and Skyllinstad (2009). A two-dimensional ridge obstructing the flow was based on the Witch of Agnesi profile

$$h(y,z) = \frac{h a^2}{y^2 + a^2} \quad (3)$$

for a mountain of height, $h = 600\text{m}$, and width, $a = 4000\text{m}$, which is comparable to the rotor inducing terrain on the Falkland Islands (fig 4.1). An idealized initial state is prescribed with constant static stability of $N = 0.01 \text{ s}^{-1}$. The streamwise velocity, v , increases linearly from 5 m s^{-1} to 11.5 m s^{-1} at 13 km. Temperature inversions, if present, are centered at $z_i = 900$ and $z_i = 1800$ and have a depth of 200m. Using the velocity at crest level of 5 m s^{-1} and the free troposphere stability, $N = 0.01 \text{ s}^{-1}$, a non-dimensional mountain height of $Nh/v = 1.2$, and a non-dimensional mountain width of $Na/v = 8$ were prescribed for our simulations.

Domain size was set to $80 \times 6480 \times 300$ grid points in the along slope, cross slope, and vertical directions respectively, with grid resolution of 15 m in all directions below 3 km. Above 3 km, the vertical grid spacing stretches from 15 m to 170m at the model domain top. The total domain size was $1.2 \text{ km} \times 97.2 \text{ km} \times 13.1 \text{ km}$. The mountain was centered at $y = 58.3 \text{ km}$, slightly past the center point in the streamwise direction. Surface heating was applied throughout the entire for the entire experiment domain

unless otherwise indicated as being applied upstream of the ridge only, or downstream of the ridge only. A summary of all experiments can be found in table 4.1.

b. Low inversion height

Previous modeling studies of the influence of surface heat fluxes on IGW breaking cases lacking an inversion (Smith and Skillingstad, 2009) combined with studies on how the mechanism of downslope windstorm formation varies according to upstream inversion height (Smith and Skillingstad, 2010) suggests that diurnal variation of downslope windstorm behavior may depend greatly on inversion height. The inversion strengths and heights presented herein are consistent with both previous modeling studies and observations taken on the Falklands Islands (Mobbs et. al, 2005) and serve as a useful simplified guide in interpreting the complex behavior of the surface observations. We first present streamwise velocity for the low inversion case with no surface heating (fig 4.8a), which is identical to that presented in Smith and Skillingstad (2010). In this and subsequent plots we have chosen to present results at dynamically important times in the flow evolution though the experiment does not achieve a quasi-steady state. All variables presented in the plots are instantaneous at a single cross section in the model domain unless otherwise specified as being averaged. Details of our averaging procedure and turbulent kinetic energy (TKE) calculations can be found in the appendix. The lee flow response shows wave breaking and turbulence near $y = 64$ km, where the inversion begins to return to its undisturbed upstream height of $z_i = 900$ m. There is a transition of the shallow water mode as the Froude number, which we define as

$$Fr = \frac{v}{\sqrt{g' z_i}} \quad (4)$$

where the reduced gravity, and g' is defined as

$$g' = g \frac{\Delta\theta}{\theta_0} \quad (5)$$

and $\Delta\theta$ is the strength of the inversion, becomes greater than unity at ridge crest and falls to below unity after the hydraulic jump. Despite the return a large portion of the inversion back to its upstream height, the surface jet reaches fairly far downstream, especially in comparison with the low inversion heating case (fig 4.8b). TKE in the

boundary layer, which is calculated according the method presented in the appendix, is present from the surface up to the inversion (fig 4.9b) both upstream and downstream of the ridge and prevents a well formed jet from reaching significantly far downstream from the ridge. Enhanced turbulence in the heating case also causes substantial mixing of the inversion layer, and the inversion downstream of the ridge is more diffuse than the no heating case. In the cooling case (fig 4.8c and fig 4.10), where 2 hrs of surface cooling of 200 Wm^{-2} were applied after 4 hours of heating of 200 Wm^{-2} , a strong jet and zone of stagnant air located just below the inversion extend far downstream. The transition for the cooling case occurs relatively quickly. After 20 minutes of surface cooling (fig 4.10a) the surface jet has already begun to restratify in the lee of the ridge and has extended a further 10 km downstream relative to the heating case from which this case was initialized. After 40 minutes of surface cooling (fig 4.10b) on the upstream side of the ridge flow blocking and a drainage flow have developed and the boundary layer has begun to restratify as well. After 2 hours of surface cooling (fig 4.8c) the inversion downstream of the jump is relatively weak compared to its undisturbed upstream strength, and a significant portion of it remains in the strongly stably stratified surface jet. Flow blocking and a drainage flow have created a pocket of negative surface velocities on the upstream side of the ridge, while in the far downstream solitary like waves are present and slowly propagate back towards the ridge.

Much of the inversion returns intact to its upstream value in the lee of the ridge in the no heating case, while in the cooling case much of the inversion remains on the lee slope instead. Shear production (also not shown) in all three cases is qualitatively similar to that presented in Smith and Skyllingstad (2010), while for the heating case transport of TKE over the ridge and buoyant production of TKE (not shown) are both important in determining the extent of the lee jet.

c. Medium inversion height

Our previous modeling study (Smith and Skyllingstad, 2010) suggested a distinctly different mechanism of downslope windstorm formation for medium inversion height than that of low inversion height. In fact the inversion instability mechanism was shown to produce downslope windstorms in cases where the velocity and temperature

structure of an upstream sounding which otherwise not predict based on IGW breaking or barotropic Froude number considerations. The medium inversion no heating case (fig 4.11a), which is identical to that presented in Smith and Skillingstad (2010), has a deeper, stronger and slightly shorter jet than the low inversion no heating case (fig 4.8a) since the entire flow beneath the inversion being forced below the stagnation zone. There are also lee wave rotors present in the medium inversion case due to large adverse near surface pressure gradient. The application of surface heating of 200 Wm^{-2} results in a lee flow response in which there is no downslope jet present at all (fig 4.11b). Large amounts of TKE (fig 4.12b) due to buoyant production of TKE (not shown) and reduced stratification in the boundary have prevented a wave response over the ridge, and the perturbations on the inversion are not significant enough to form a large stagnation zone. The surface cooling case (fig 4.11c and fig 4.15), which was run using 6 hours of 200 Wm^{-2} of surface heating followed by 200 Wm^{-2} of surface cooling for 4 hours, is characterized by a strong downslope jet which extends far downstream, strong stratification in the surface layer, and lack of downstream rotors in contrast to the medium height no heating case (fig 4.11a). Turbulence in the stagnation zone for the medium inversion cooling case (fig 4.12c) is broadly similar to that of the medium height no heating case (fig 4.12a) with the exception of the turbulent lee rotors. Turbulence in the heating case is generally confined to the boundary layer (fig 4.12b) and is mainly produced by buoyancy perturbations (not shown), while in the no heating case (fig 4.12a) and medium height cooling case (fig 4.12c) turbulence is generated primarily by shear production at the interface of the stagnation zone and surface jet as shown in Smith and Skillingstad (2010).

The role of transport of turbulence over the ridge versus turbulence generated downstream of the ridge in determining the lee flow response was investigated using simulations in which the surface heating is constrained to either the upstream side of the ridge (fig 4.13a) or the downstream side of the ridge (fig 4.13b). As in Smith and Skillingstad (2009), the upstream heating case (fig 4.13a) is very similar to the case where heating is applied everywhere (fig 4.11b), while the downstream heating case (fig 4.13b) is more similar to the no heating and surface cooling cases (fig 4.11a and fig 4.11c, respectively). Some turbulence is transported over the ridge in the upstream heating case (fig 4.14a), while TKE in the downstream heating case is largely generated downstream

of the ridge itself (fig 4.14b). While this turbulence doesn't interact strongly with that of the stagnation zone near the slope, it is strong enough to mix out any lee rotor structure. TKE in the boundary layer of the upstream heating and downstream heating cases is generated primarily by the buoyant production term (not shown), while shear production along the top of the surface jet and bottom of the stagnation zone in the downstream heating case (not shown) is broadly similar to the no heating case and cooling case (also not shown).

The transition from turbulent boundary layer to downslope jet in the medium height surface cooling case is shown in more detail in figure 4.15. After 140 minutes of surface cooling (fig 4.15a) the boundary layer beneath the inversion has begun to restratify, resulting in a mountain wave induced perturbation on the inversion which slowly begins to propagate back towards the ridge crest. As this perturbation propagates back towards the ridge it amplifies and creates a pocket of neutrally stratified stagnant air whose isotherms begin to overturn (fig 4.15b). The overturning isotherms begin to generate turbulence in the nascent stagnation zone, which begins to grow downwards and downstream, forcing the lee surface jet below (fig 4.15c). The mechanism by which downslope windstorms form in this case is very similar to that presented in Smith and Skillingstad (2010). Briefly, imbalances between pressure gradient and advection terms in the momentum budget equations lead to the propagation of the perturbation on the inversion back towards the ridge, the splitting of the inversion and the creation of a pocket of stagnant air. Shear production from the initial instability and along the top of the surface jet where velocity gradients are large acts to grow the nascent stagnation zone downstream, under which the lee slope jet is forced beneath thus forming a downslope windstorm.

d. Katabatic flow contribution

To ascertain the contribution of katabatic flows to the surface cooling experiments we ran low inversion height and medium inversion height experiments with no mean flow velocity and 50 Wm^{-2} and 200 Wm^{-2} of cooling. The cases with the low inversion height were very similar to those of the medium inversion height case which are presented in figure 4.16. The weak and strong cooling katabatic cases resulted in a

drainage flow that grew to 200 m depth far downslope, with flow velocities of approximately 3 ms^{-1} and 5 ms^{-1} respectively (fig 4.16). The drainage flows extended far downstream. Profiles of flow velocity in the medium inversion cases show very little difference between surface flow velocities of the no heating, weak cooling and strong cooling cases (fig 4.17b) in the near-slope ($y = 65 \text{ km}$) and far downslope locations ($y = 75 \text{ km}$) despite the relatively strong drainage flows that developed in the katabatic only simulations. The far downslope location in the low inversion case however, does show a significant increase in flow velocity in the cooling case relative to the no heating case (fig 4.17a). The increased velocity of the cooling cases with respect to the no heating case can largely be accounted for by the contribution of the drainage flow.

4.4 Conclusions

The focus of this study was to examine observations and numerical experiments of downslope windstorms for evidence of diurnal variation in magnitude, jet length, and preferred onset and cessation times. Analysis of observations taken in the lee of a 2-D ridge revealed a number of interesting characteristics of downslope windstorms on the Falkland Islands. In most events the lee surface jet does not extend very far downstream. Aside from a modulation of boundary layer height which led to increased momentum transfer from aloft, downslope windstorm events preferentially occurred during nighttime. Events with significant downstream extent tended to occur in conjunction with strong inversions, while events that occurred in conjunction with weak inversions were more often of limited downstream extent. A few specific events were presented which were indicative of the general trend: diurnal variations in downslope windstorms do occur, sometimes with or without synoptic changes, and strong inversions tend to lead to lee surface jets with significant downstream extent.

Next a series of simplified numerical experiments were presented which explored the effect of surface heat fluxes on downslope windstorms which occurred in conjunction with a strong ridgetop level inversion. Surface heating was shown to reduce lee jet length due to transport of TKE over the ridge and buoyant production of TKE in the lee of the ridge. Surface cooling applied to a low inversion case with a fully turbulent neutrally stratified boundary layer resulted in an increase in jet length. The katabatic contribution

to this jet length was fairly significant far away from the slope, which seems to be in agreement with observations from the Falkland Islands.

The series of cases presented with a medium height level inversion presented an even more extreme example of surface heating leading to a complete absence of downslope windstorms. It was suggested that this is due to the lack of mountain wave induced perturbation on the inversion. When surface cooling was applied to a medium inversion case with a fully turbulent neutrally stratified boundary layer, the lee flow transitioned to downslope windstorm. The transition which occurred resulted in a jet which, besides additional near surface stratification, was not much stronger than the no heating case, although lee wave rotors were notably absent during the surface cooling case. For the medium inversion height katabatic contributions to the cooling case were minimal.

Overall this study points to a lack of temporally appropriate upper air data to discern diurnal variations in downslope windstorm behavior from those variations which occur on synoptic time scales. The use a well placed profiler would probably be quite useful to address this issue. A number of intriguing agreements, spatially and temporally, between the observations on the Falkland Islands and our numerical experiments were presented with forecasting implications for downslope windstorms over a low ridge.

- 1) Absent synoptic scale changes in forcing, downslope windstorms over a low ridge may preferentially occur in the evening, especially in locations far downstream.
- 2) The downstream extent of an event varies according to inversion strength and surface heating.
- 3) Drainage flow contributions to downslope windstorms vary according to inversion strength and surface heating.

Acknowledgements: This research was funded by the National Science Foundation under grant ATM-0527790. We also wish to thank the anonymous reviewers for their help in strengthening the manuscript.

Appendix

For the purposes of this study we define the average of a variable ϕ as follows.

$$\bar{\phi}(y, z) = \frac{1}{i_{\max} \cdot n_{\max}} \sum_{n=1}^{n_{\max}} \sum_{i=1}^{i_{\max}} \phi(x, y, z) \quad (6)$$

where the overbar denotes average. In this equation i_{\max} is the number of points in the spanwise direction and n_{\max} is the number of time steps over the 5 minute averaging time.

Turbulent kinetic energy, TKE, is calculated by using the spanwise mean

$$\phi_{spanwise\ mean}(y, z) = \frac{1}{i_{\max}} \sum_{i=1}^{i_{\max}} \phi(x, y, z) \quad (7)$$

to calculate perturbations about the spanwise mean

$$\phi'(x, y, z) = \phi(x, y, z) - \phi_{spanwise\ mean}(y, z) \quad (8)$$

and the average resolved eddy TKE is defined as

$$e' = \frac{1}{2} (u'^2 + v'^2 + w'^2), \quad (9)$$

and perturbation velocities are calculated as in (7) and (8), and the averaging is done in the spanwise direction as well as temporally as in (6). Computing averages in this way removes the large-scale internal waves generated by the mountains, however smaller scale waves are still treated as “turbulence.” Nevertheless, this method yields turbulence fields that are consistent with buoyant and shear production of turbulence as shown below.

Figures

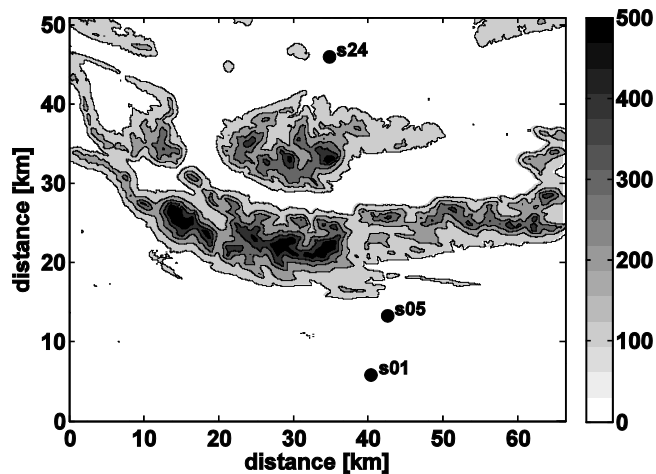


Figure 4.1. The location of the stations on the East Falkland Island used in this analysis. Terrain height (m) is shaded.

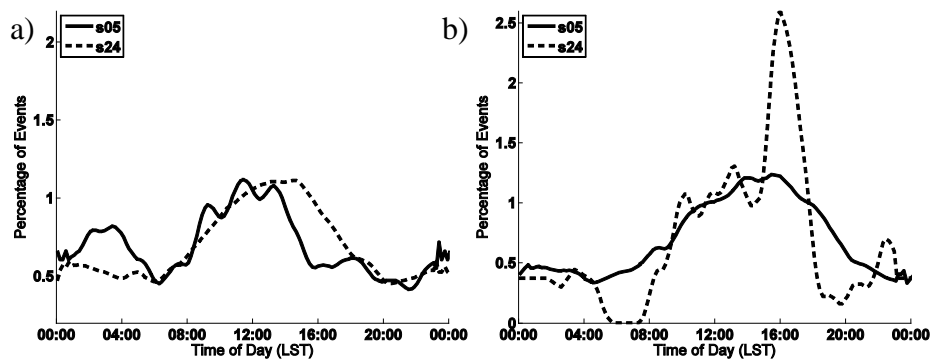


Figure 4.2. Diurnal variation of a) northerly wind events and b) southerly wind events for stations #05 and #24.

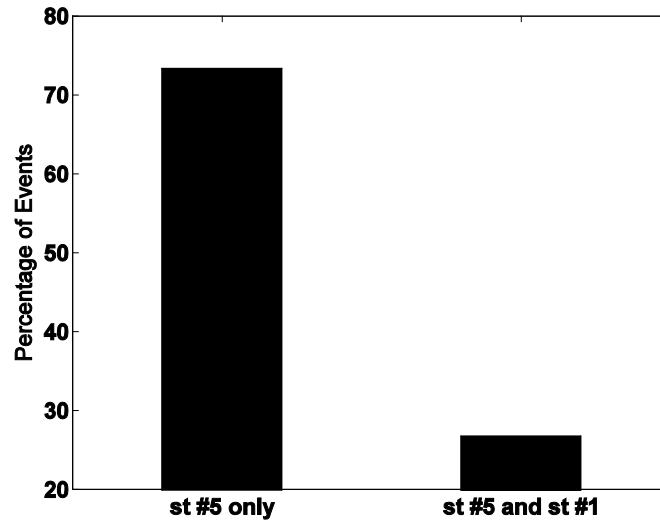


Figure 4.3. Percentage of northerly wind events which occur at station #5 only, and stations #5 and #1 contemporaneously.

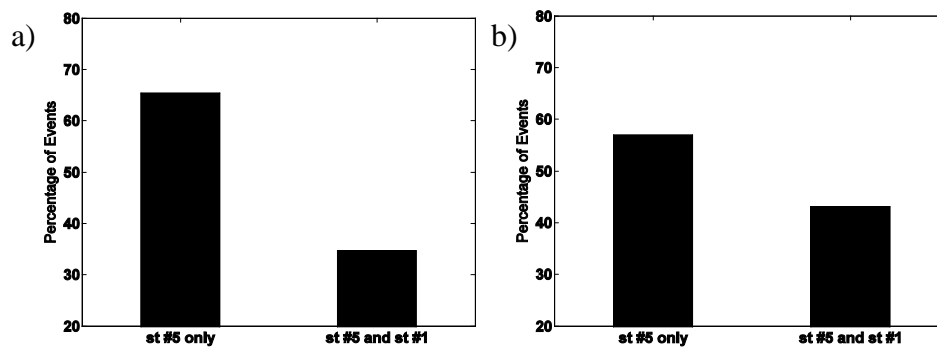


Figure 4.4. Percentage of northerly wind events whose correlated soundings have a) $\Delta\theta < 4 \text{ K}$ and b) $\Delta\theta > 4 \text{ K}$ which occur at station #5 only (left bar), and stations #5, and #1 contemporaneously (right bar).

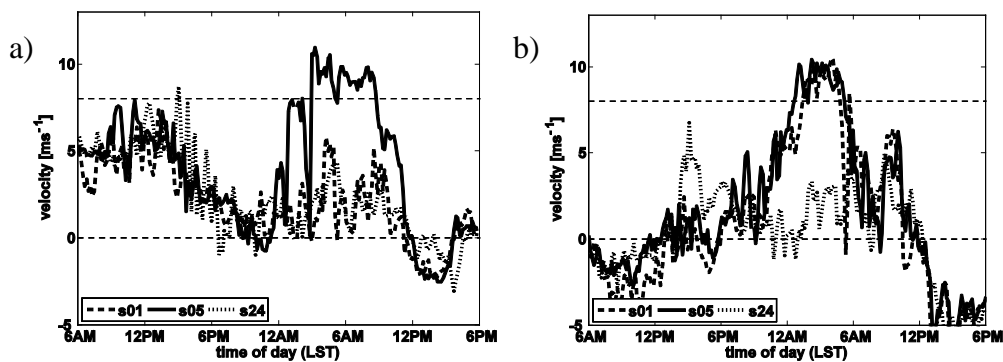


Figure 4.5. Northerly wind velocity at stations #01, #05, and #24 versus time for a) 6am 8/12/01 to 6pm 8/13/01 (LST), and b) 6am 1/26/01 to 6pm 1/27/01 (LST).

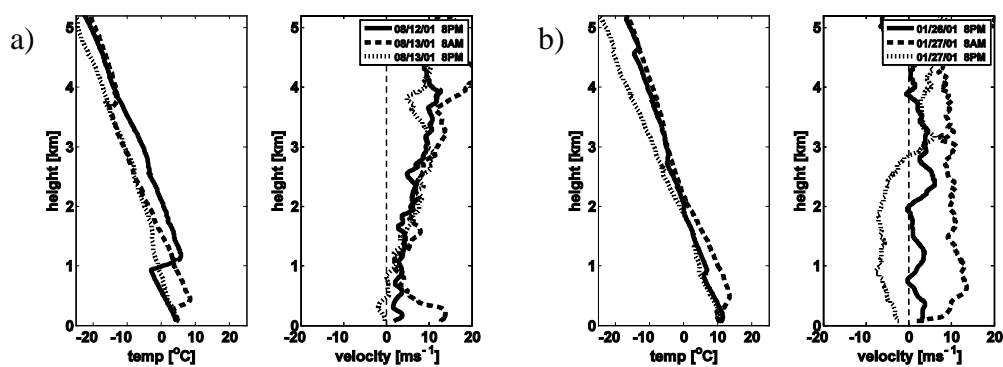


Figure 4.6. Temperature (left column) and northerly wind velocity (right column) versus height for the soundings taken between a) 8pm 8/12/01 to 8pm 8/13/01 (LST) and b) 8pm 1/26/01 to 8pm 1/26/01 (LST).

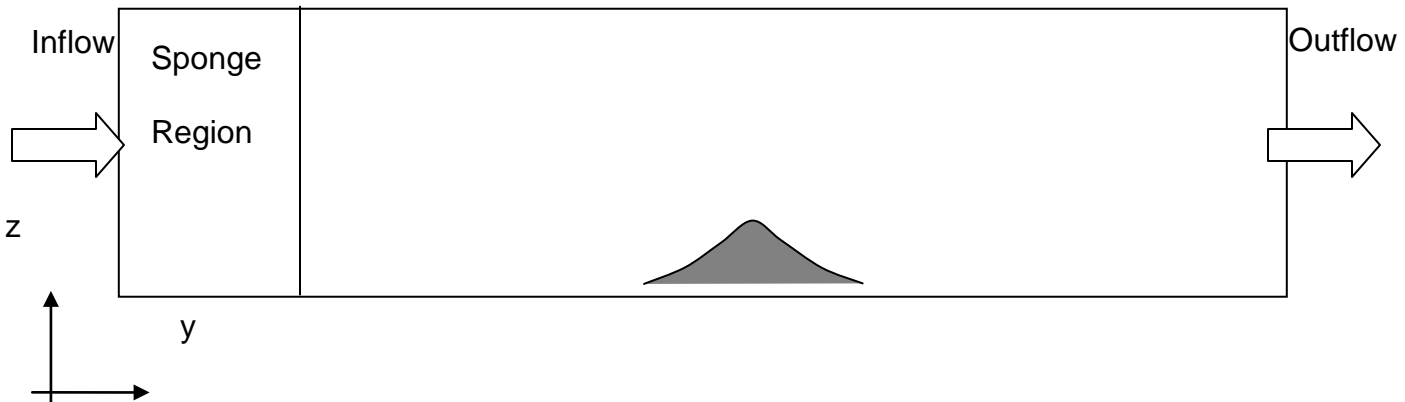


Figure 4.7. Schematic showing the channel flow configuration used in the simulations.

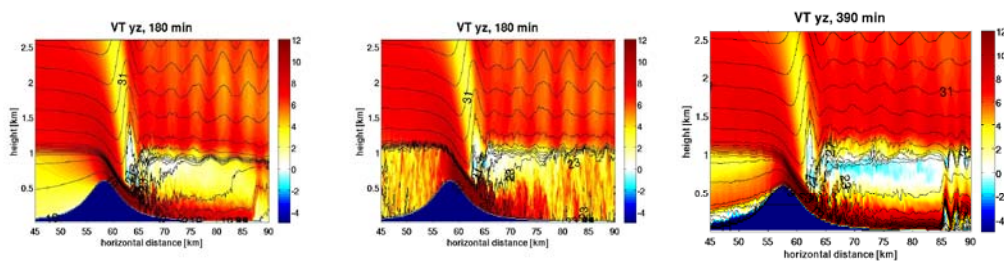


Figure 4.8. Close up view of streamwise velocity (shading in ms^{-1}) and potential temperature (lines of constant $^{\circ}\text{C}$) for the a) low inversion case at $t = 180$ min, b) low inversion heating case at $t = 180$ min c) and low inversion cooling case at $t = 390$ min.

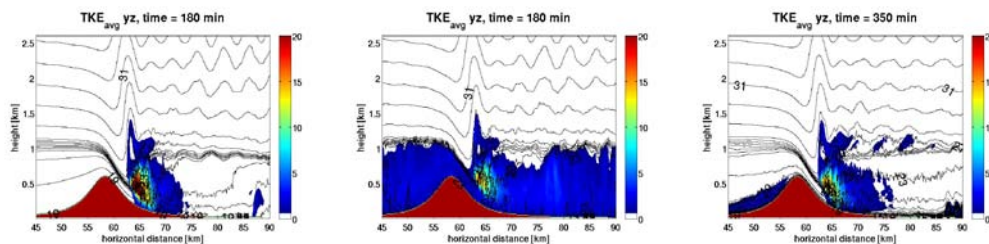


Figure 4.9. Close up view of average TKE (shading in m^2s^{-2}) and potential temperature (lines of constant $^{\circ}\text{C}$) for the a) low inversion case at $t = 180$ min, b) low inversion heating case at $t = 180$ min c) and low inversion cooling case at $t = 350$ min.

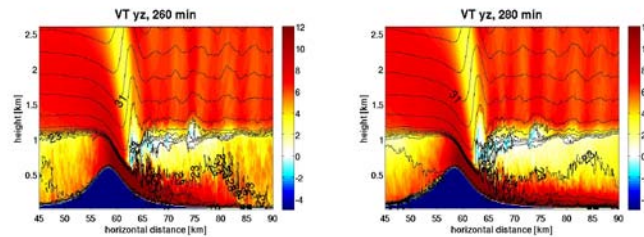


Figure 4.10. Close up view of streamwise velocity (shading in ms^{-1}) and potential temperature (lines of constant $^{\circ}\text{C}$) for the a) low inversion cooling case at a) $t = 260$ min, and b) $t = 280$ min.

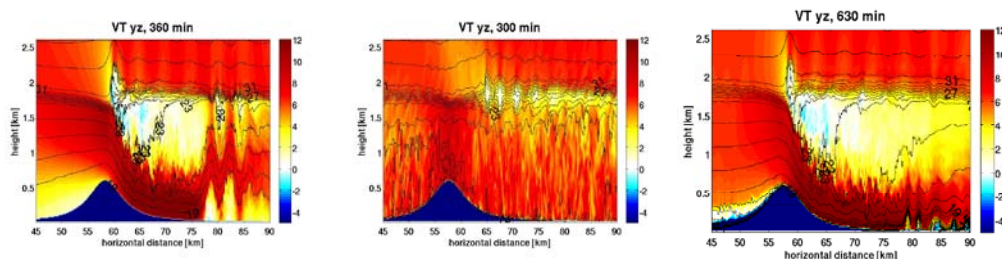


Figure 4.11. Close up view of streamwise velocity (shading in ms^{-1}) and potential temperature (lines of constant $^{\circ}\text{C}$) for the a) medium inversion case at $t = 360$ min, b) medium inversion heating case at $t = 300$ min c) and medium inversion cooling case at $t = 630$ min.

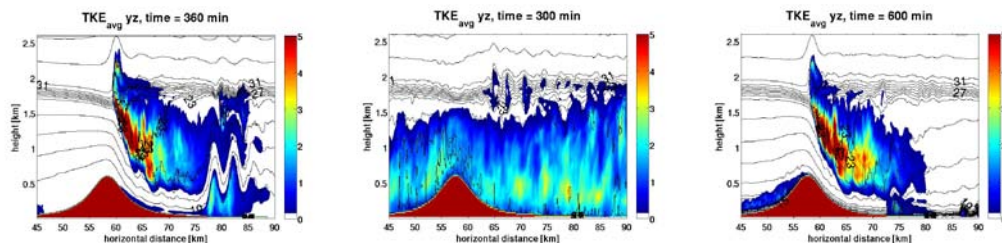


Figure 4.12. Close up view of average TKE (shading in m^2s^{-2}) and potential temperature (lines of constant $^{\circ}\text{C}$) for the a) medium inversion case at $t = 360$ min, b) medium inversion heating case at $t = 300$ min c) medium inversion cooling case at $t = 600$ min.

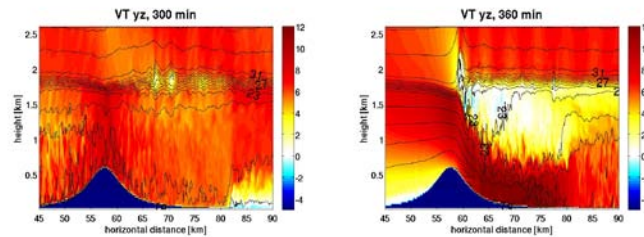


Figure 4.13. Close up view of streamwise velocity (shading in ms^{-1}) and potential temperature (lines of constant $^{\circ}\text{C}$) for the a) medium inversion upstream heating case at $t = 300$ min, b) medium inversion downstream heating case at $t = 360$ min.

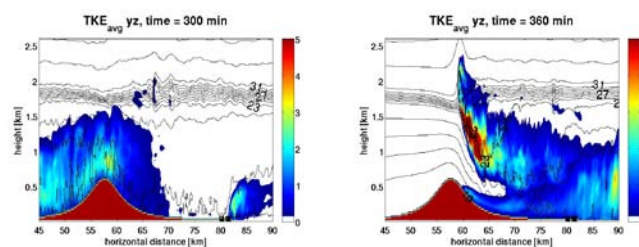


Figure 4.14. Close up view of average TKE (shading in m^2s^{-2}) and potential temperature (lines of constant $^{\circ}\text{C}$) for the a) medium inversion upstream heating case at $t = 300$ min, and b) medium inversion downstream heating case at $t = 360$ min .

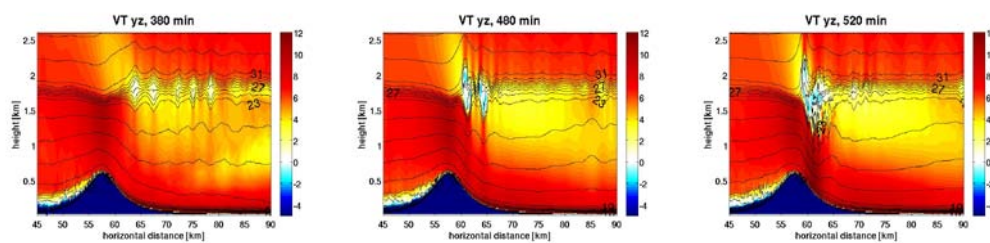


Figure 4.15. Close up view of streamwise velocity (shading in ms^{-1}) and potential temperature (lines of constant $^{\circ}\text{C}$) for the medium inversion cooling case at a) $t = 380$ min, b) $t = 480$ min and c) $t = 520$ min.

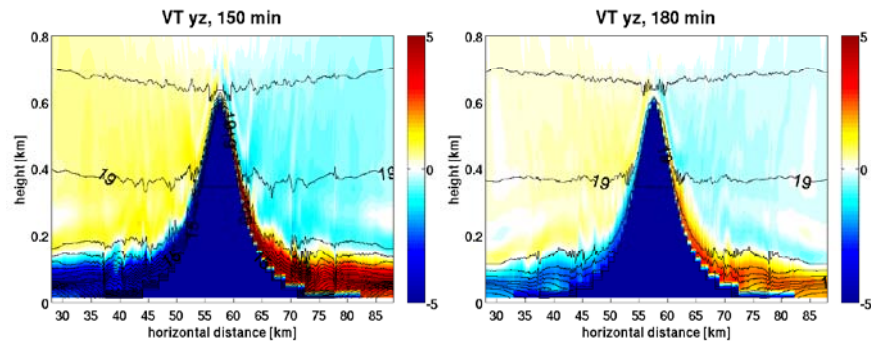


Figure 4.16. Close up view of streamwise velocity (shading in ms^{-1}) and potential temperature (lines of constant $^{\circ}\text{C}$) for the medium inversion a) strong cooling katabatic flow case at $t = 150$ min and b) weak cooling katabatic flow case at $t = 180$ min.

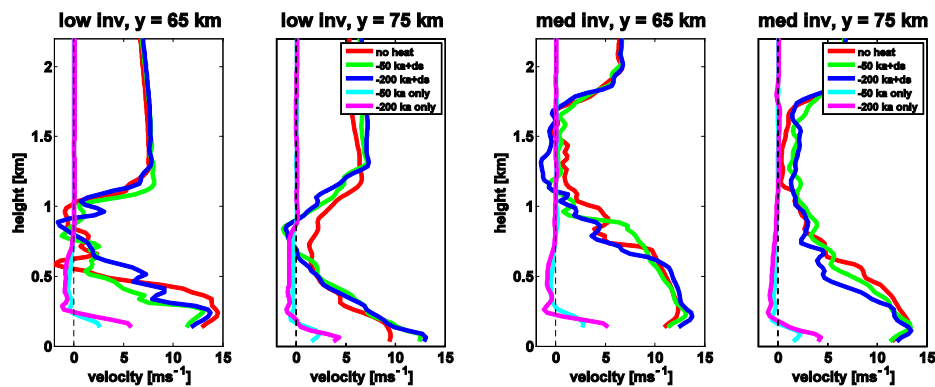


Figure 4.17. Velocity profiles of the a) low inversion and b) medium inversion katabatic flow and katabatic-downslope flows at $y = 65$ km (left) and $y = 75$ km (right).

Tables

	z_i (m)	$\Delta\theta$ (K)	Surface Heat Flux (Wm^{-2})
Low inversion no heating	900	8	000
Low inversion heating	0900	8	+200
Low inversion strong cooling	0900	8	-200
Low inversion weak cooling	0900	8	-50
Low inversion strong katabatic	0900	8	-200
Low inversion weak katabatic	0900	8	-50
Medium inversion no heating	1800	8	000
Medium inversion heating	1800	8	+200
Medium inversion strong cooling	1800	8	-200
Medium inversion weak cooling	1800	8	-50
Medium inversion upstream heating	1800	8	+200 upstream only
Medium inversion downstream heating	1800	8	+200 downstream only
Medium inversion strong katabatic	1800	8	-200
Medium inversion weak katabatic	1800	8	-50

Table 4.1: List of all simulations and their characteristics.

5 Conclusions

5.1 Mechanisms of downslope windstorm formation

Mechanisms of downslope windstorm formation were explored in a number of numerical experiments. A case lacking an inversion case resulted in IGW breaking and the creation of a stagnation zone with a series of trapped lee rotors. The dominant mechanism for downslope windstorm generation in a high inversion case was also shown to be IGW breaking since the inversion height was above the level of breaking so that the creation of the self induced stagnation zone was not constrained. A low inversion led to the creation of a lee slope jet with significant downstream extent, and large amounts of shear production of TKE along the interface between the surface jet and stagnation zone. This may provide a mechanism for the significant gustiness observed in many downslope windstorms. The low inversion case had a control point for interfacial waves at the ridge crest indicating a two layer behavior with a subcritical to supercritical transition of the barotropic interfacial mode. Despite the strong lee jet in the medium inversion case the barotropic Froude number never exceeded unity, indicating that interfacial waves on the inversion may propagate upstream and downstream, and the lee jet was not capped by the strong inversion, but rather the inversion remained above the stagnation zone. Analysis of IGW kinetic energy aloft revealed that trapping of IGW energy in the lower layer by the inversion was also not important in the medium inversion case. A further series of numerical experiments explore the effect of IGW nonlinearity of the medium inversion case, and the resulting flows could not be adequately described by existing IGW breaking theory, i.e. downslope windstorms still occurred for experiments with $Nh/v < 1.0$.

The mechanism of downslope windstorm formation for this case was shown to be mountain wave induced instabilities on the inversion and associated coupling of the stagnation zone with the lee surface jet. The generation of the stagnation zone was due to imbalances in the momentum budget equation in which pressure gradient and advection forces lead to a pocket of neutrally stratified stagnant air which propagates

back to the ridge and amplifies. Amplification of the perturbation and overturning of isotherms led to shear production of TKE which forced the stagnation zone to grow downstream. The lee jet is forced beneath the stagnation zone leading to the creating of a downslope windstorm. The inversion instability mechanism is relevant for forecasters because it suggests a scenario in which downslope windstorms may occur when neither a barotropic transition nor IGW breaking are predicted.

5.2 Influence of surface heat fluxes and slope flows on downslope windstorms

Analysis of observations taken on the Falkland Islands reveal that downslope windstorms may vary in magnitude, spatial extent and existence on diurnal time scales. Aside from the first order effect of modulation of boundary layer top wind speeds due to increased momentum transfer from aloft, downslope windstorm events were shown to preferentially occur during nighttime. Most downslope windstorms events were characterized by a jet of limited downstream extent. Events which occurred in conjunction with a strong inversion often extended far downstream, while those that occurred in conjunction with weak inversions were more often of limited downstream extent. A few specific events were presented which were indicative of the general trend: diurnal variations in downslope windstorms do occur, sometimes with or without synoptic changes, and strong inversions tend to lead to lee surface jets with significant downstream extent.

Next a series of experiments were presented in which the effect of surface heat fluxes on downslope windstorms induced by IGW breaking was explored. In the basic case with no application of surface heat fluxes a typical nonlinear wave response was produced, with a lee side surface jet and a large zone of stagnant air above the lee side of the mountain that eventually resulted in overturning of isotherms and generation of turbulence. Turbulence was initially generated by buoyant production in the IGW overturning region and subsequently by shear production along the edges of the stagnation zone, especially at the interface with the surface jet on the lee of the slope. A series of rotors formed in the lee of the ridge, despite the fact the ridge was fairly broad.

The distinct rotors slowly propagated back towards the ridge, where they were decayed due to mixing by TKE from the stagnation zone and TKE generated indigenously in the rotor zone by gradients in vertical and horizontal velocity.

Weak surface heat flux was found to reduce rotor strength and increase rotor heights. A weak heating of 25 W m^{-2} led to the absence of negative streamwise velocities under the lee waves, which were strongly modified by convective forcing. Lee-side downslope winds in this case were not strongly affected by turbulence unlike the strong surface heating case, which prevented the formation of rotors and produced a much weaker downslope wind event. Simulations with heating confined to either the upstream or downstream side of the mountain revealed that locally generated turbulence on the downstream side of the mountain was more important in controlling the rotor behavior than turbulence advected over the mountain from the upstream boundary layer.

Application of surface cooling forced an enhanced rotor circulation in which the train of lee rotors were capped by a strongly stratified high velocity jet. Increased stratification from surface cooling was found to be important in the formation of the stably stratified undulating jet, which led to increased shear production between the jet and the rotors while increased buoyant destruction of TKE in the rotor downdrafts acted to maintain the rotor circulations for a longer distance downstream from the ridge.

A series of simplified numerical experiments on downslope windstorms which occurred with a strong low level inversion led to distinctly different behavior. For low inversion heights and hydraulically controlled flow, surface heating was shown to reduce lee jet length due to transport of TKE over the ridge and buoyant production of TKE in the lee of the ridge. A simplified day to night transition experiment revealed that the application of surface cooling applied to a fully turbulent neutrally stratified boundary layer resulted in an increase in jet length. Far away from the slope the katabatic contribution to this jet length was significant.

Surface heat fluxes play an even more important role in determining lee flow dynamics in cases where the above described inversion instability mechanism played the dominant role in forming a downslope jet. When surface heating was applied to this case the resulting lack of stratification in the boundary layer beneath the inversion reduced the ability of the mountain wave to perturb the inversion enough that spontaneously growing

instabilities occur and force a growing stagnation zone. The application of surface cooling to a fully turbulent neutrally stratified boundary layer led to a transition of the lee flow to a downslope windstorm in which the lee jet was not much stronger than the no heating case, although lee wave rotors were notably absent during the surface cooling case. The katabatic contribution to this case was minimal.

Overall these observations and experiments suggest the following

- 1) Downslope windstorms over a low ridge may occur even in the absence of synoptic scale changes. These events may preferentially occur in the evening.
- 2) Events that occur in conjunction with a strong low level inversion will tend to extend further downstream than those events that occur in conjunction with weaker or higher inversions.
- 3) In events driven by IGW breaking, lee rotors may extend further downstream during nighttime, and may be characterized by reduced strength and increased height during the daytime.
- 4) The nighttime behavior of hydraulically controlled events may adequately be described as a contribution of a katabatic flow to a downslope windstorm event while drainage flow contributions are not able to adequately account for the strong change in lee flow dynamics in cases with an intermediate inversion height.
- 6) IGW breaking considerations and hydraulic considerations are not able to adequately predict downslope windstorms for cases with an intermediate level inversion. Most likely a non eddy resolving model would predict different behavior than the well resolved instability mechanisms that we see in our experiments.

While downslope windstorms and rotors are considered extremely hazardous to the aviation community, many unanswered questions remain regarding the relative importance of elevated inversions in their formation. Results presented here address some of the outstanding issues regarding the importance of surface heat fluxes in nonlinear IGW and hydraulic regimes, but it is clear that synoptically based upstream soundings (i.e. once every 12 hours) are of limited help in resolving these issues. This

study points to a lack of temporally appropriate upper air data to discern diurnal variations in downslope windstorm behavior from those variations which occur on synoptic time scales. A well placed profiler would probably be quite useful to address this issue.

References

- Adcroft, A., C. Hill, and J. Marshall, 1997: Representation of topography by shaved cells in a height coordinate ocean model. *Mon. Wea. Rev.*, **125**, 2293-2315.
- Afanasyev, Y., and W. Peltier, 1998: The three-dimensionalization of stratified flow over two-dimensional topography. *J. Atmos. Sci.*, **55**, 19-39.
- Bacmeister, J. T., and R. T. Pierrehumbert, 1988: On high drag states of nonlinear stratified flow over an obstacle. *J. Atmos. Sci.*, **45**, 63-80.
- Belusic D., M. Zagar, and B. Grisogono, 2007: Numerical simulation of pulsations in the bora wind. *Q. J. R. Meteorol. Soc.* **133**, 1371-1388.
- Bower, J. B., and D. R. Durran, 1986: A study of wind profile data collected upstream during windstorms in Boulder, Colorado. *Mon. Wea. Rev.*, **114**, 1491-1500.
- Brinkmann, W. A. R., 1974: Strong downslope winds at Boulder, Colorado. *Mon. Wea. Rev.*, **102**, 592-602.
- Clark, T. L., and W. R. Peltier, 1977: On the evolution and stability of finite-amplitude mountain waves. *J. Atmos. Sci.*, **34**, 1715-1730.
- Clark, T. L., and W. R. Peltier, 1984: Critical level reflection and the resonant growth of nonlinear mountain waves. *J. Atmos. Sci.*, **41**, 3122-3134.
- Clark, T. L., W. D. Hall, R. M. Kerr, D. Middleton, L. Radke, F. M. Ralph, P. J. Neiman, and D. Levinson, 2000: Origins of aircraft-damaging turbulence during the 9 December 1992 Colorado downslope windstorm: Numerical simulations and comparison with observations. *J. Atmos. Sci.*, **57**, 1105-1131.
- Colle, B. A., and C. F. Mass, 1998a: Windstorms along the western side the Washington Cascades. Part I: A high resolution observations and modeling study of the 12 February 1995 event. *Mon. Wea. Rev.*, **126**, 28-52.
- Colle, B. A., and C. F. Mass, 1998b: Windstorms along the western side the Washington Cascades. Part II: Characteristics of past event and three dimensional idealize simulations. *Mon. Wea. Rev.*, **126**, 53-71.
- Colman, B. R., and C. F. Dierking, 1992: The Taku wind of Southeast Alaska: Its identification and prediction. *Weather and Forecasting*, **7**, 49-63.

- Colson, D., 1954: Meteorological problems in forecasting mountain waves. *Bull. Amer. Meteor. Soc.*, **35**, 363-371.
- Czyzyk, S., and K. Runk, 2006: Operational forecast support by national weather service forecast office in Las Vegas, Nevada during the Terrain-Induced Rotor Experiment. Online Proceedings. 12th Conference on Mountain Meteorology. Amer. Meteor. Soc. Paper **2.5**
- Deardorff, J. W., 1980: Stratocumulus-capped mixed layers derived from a three-dimensional model. *Boundary-Layer Meteor.*, **18**, 495-527.
- Dornbrack, A., 1998: Turbulent mixing by breaking gravity waves. *J. Fluid Mech.* **375**, 113-141.
- Doyle, J. D., D. R. Durran, C. Chen, B. A. Colle, M. Georgelin, V. Gruibisic, W. R. Hsu, C. Y. Huang, D. Landau, Y. L. Lin, G. S. Poulos, W. Y. Sun, D. B. Weber, M. G. Wurtele, and M. Xue, 2000: An intercomparison of model-predicted wave breaking for the 11 January 1972 Boulder windstorm. *Mon. Wea. Rev.*, **128**, 901-914.
- Doyle, J. D., and D. R. Durran, 2002: The dynamics of mountain-wave-induced rotors. *J. Atmos. Sci.*, **59**, 186-201.
- Doyle, J. D., M. A. Shapiro, Q. Jiang and D. L. Bartels, 2005: Large-amplitude mountain wave breaking over Greenland. *J. Atmos. Sci.*, **62**, 3106-3126.
- Doyle, J. D., and D. R. Durran, 2007: Rotor and subrotor dynamics in the lee of three-dimensional terrain. *J. Atmos. Sci.*, **64**, 4202-4221.
- Drobinski, P., C. Flamant, J. Dusek, P. Flamant, and J. Pelon, 2001: Observational evidence and modeling of an internal hydraulic jump at the atmospheric boundary-layer top during a tramontane event. *Boundary-Layer Meteor.*, **98**, 497-515.
- Ducros, F., P. Comte, and M. Lesieur, 1996: Large-eddy simulation of transition to turbulence in a boundary layer developing spatially over a flat plate. *J. Fluid Mech.* **326**, 1-37.
- Durran, D. R., and J. B. Klemp, 1983: A compressible model for the simulation of moist mountain waves. *Mon. Wea. Rev.*, **111**, 2341-2361.

- Durran, D. R., 1986: Another look at downslope windstorms. Part I: The development of analogs to supercritical flow in an infinitely deep, continuously stratified fluid. *J. Atmos. Sci.*, **43**, 2527-2543.
- Durran, D. R., and J. B. Klemp 1987: Another look at downslope windstorms. Part II: Nonlinear amplification beneath wave-overtaking layers. *J. Atmos. Sci.*, **44**, 3402-3412.
- Epifanio, C. C., and T. Qian, 2008: Wave-turbulence interactions in a breaking mountain wave. *J. Atmos. Sci.*, **65**, 3139-3158.
- Flamant, C., P. Drobinski, L. Nance, R. Banta, L. Darby, J. Dusek, M. Hardesty, J. Pelon, and E. Richard, 2002: Gap flow in and Alpine valley during a shallow south fohn event: Observations, numerical simulations and hydraulic analogue. *Q. J. R. Meteorol. Soc.*, **128**, 1173-1210.
- Fritts, D. C., J. R. Isler, and O. Andreassen, 1994: Gravity wave breaking in two and three dimensions 2. Three-dimensional evolution and instability structure. *J. Geophys. Res.* **99**, 8109-8123.
- Fritts, D. C., J. F. Garten, and O. Andreassen, 1996: Wave breaking and transition to turbulence in stratified shear flows. *J. Atmos. Sci.* **53**, 1057-1085.
- Fritts, D. C., J. F. Garten, and O. Andreassen, 1996: Wave breaking and transition to turbulence in stratified shear flows. *J. Atmos. Sci.* **53**, 1057-1085.
- Gheusi, F., J. Stein and O. S. Eiff, 2000: A numerical study of three-dimensional orographic gravity-wave braking observed in a hydraulic tank. *J. Fluid Mech.* **410**, 67-99.
- Glasnovic, D. and V. Jurcec, 1990: Determination of upstream bora layer depth. *Meteorol. Atmos. Phys.*, **43**, 137-144.
- Glickmann, T. S., Ed., 2000: *Glossary of Meteorology*. 2nd ed. Amer. Meteor. Soc., 855 pp.
- Gohm, A. and G. J. Mayor, 2004: Hydraulic aspect of fohn winds in and Alpine Valley. *Q. J. R. Meteorol. Soc.*, **130**, 449-480.
- Gohm, A. and G. J. Mayor, 2005: Numerical and observational case-study of a deep Adriatic bora. *Q. J. R. Meteorol. Soc.*, **131**, 1363-1392.

- Gohm, A., G. Mayr, A. Fix, and A. Giez, 2008: On the onset of bora and the formation of rotors and jumps near a mountain gap. *Q. J. R. Meteorol. Soc.*, **134**, 21-46.
- Grubisic, V., and J. P. Kuettner, 2003: Terrain-Induced Rotor Experiment (T-REX). Paper 11.3, 10th AMS Conference on Mesoscale Meteorology. American Meteorological Society, Portland, OR, USA. Available online from the American Meteorological Society at <http://ams.confex.com/ams/htsearch.cgi>.
- Grubisic, V., and M. Xiao, 2006: Climatology of westerly wind events in the lee of the Sierra Nevada. Online Proceedings. 12th Conference on Mountain Meteorology. Amer. Meteor. Soc. Paper **2.8**
- Hertensein, R. F., and J. P. Kuettner, 2005: Rotor types associated with steep lee topography: Influence of the wind profile. *Tellus*, **57A**, 117-135.
- Houghton, D. D., and A. Kasahara, 1968: Nonlinear shallow fluid flow over an isolated ridge. *Comm. Pure Appl. Math.*, **21**, 1-23.
- Jiang, Q., and J. D. Doyle, 2004: Gravity wave breaking over the central Alps: Role of complex terrain. *J. Atmos. Sci.*, **61**, 2249-2266.
- Jiang, Q., J. D. Doyle, and R. B. Smith, 2006: Interaction between trapped waves and boundary layers. *J. Atmos. Sci.*, **63**, 617-633.
- Jiang, Q., J. D. Doyle, S. Wang, and R. B. Smith, 2007: On boundary layer separation in the lee of mesoscale topography. *J. Atmos. Sci.*, **64**, 401-420.
- Jiang, Q., and J. D. Doyle, 2008: Diurnal variation of downslope winds in Owens Valley during the Sierra Rotor Experiment. *Mon. Wea. Rev.*, **136**, 3760-3780.
- Klemp, J. B. and R. Wilhelmson, 1978: The simulation of three dimensional convective storm dynamics. *J. Atmos. Sci.*, **35**, 1070-1096.
- Klemp, J. B., and D. R. Durran, 1987: Numerical modelling of bora winds., *Meteorol. Atmos. Phys.*, **36**, 215-227.
- Klemp, J. B., Rotunno, R., Skamarock, W. C., 1997: On the Propagation of Internal Bores. *J. Fluid Mech*, **331**, 81-106
- Klemp, J. B., and D. R. Durran, 1987: Numerical modelling of bora winds., *Meteorol. Atmos. Phys.*, **36**, 215-227.
- Klemp, J. B., Rotunno, R., Skamarock, W. C., 1997: On the propagation of internal bores. *J. Fluid Mech*, **331**, 81-106.

- Kuettner, J., 1959: The rotor flow in the lee of mountains: G. R. D. Res. Notes, No. 6, Air Force Cambridge Res. Center, 20pp.
- Lilly, D. K., and E. J. Zipser, 1972: The Front Range windstorm of January 11, 1972: *Weatherwise*, **25**, 56-63.
- Lin, Y. and T. Wang, 1996: Flow regimes and transient dynamics of two-dimensional stratified flow over an isolated mountain ridge. *J. Atmos. Sci.*, **53**, 139-158.
- Liu, M., D. L. Westphal, T. R. Holt, and Q. Xu, 2000: Numerical simulation of a low-level jet over complex terrain in Southern Iran. *Mon. Wea. Rev.*, **128**, 1309-1327.
- Long, R. R., 1954: Some aspects of the flow of stratified fluids. Part II: Experiments with a two fluid system: *Tellus*, **6**, 97-115.
- Laprise, R. and W. R. Peltier, 1989a: The linear stability of nonlinear mountain waves: Implications for the understanding of severe downslope windstorms., *J. Atmos. Sci.*, **46**, 545-564.
- Laprise, R. and W. R. Peltier, 1989b: The structure and energetics of transient eddies in a numerical simulation of breaking mountain waves., *J. Atmos. Sci.*, **46**, 565-585.
- Laprise, R. and W. R. Peltier, 1989c: On the structural characteristics on steady finite-amplitude mountain waves over bell-shaped topography., *J. Atmos. Sci.*, **46**, 586-595.
- Lilly, D. K., and E. J. Zipser, 1972: The Front Range windstorm of January 11, 1972: *Weatherwise*, **25**, 56-63.
- Lilly, D. K., 1978: A severe downslope windstorm and aircraft turbulence event induced by a mountain wave., *J. Atmos. Sci.*, **35**, 59-77.
- Mayor, S. D., P. R. Spalart, and G. J. Tripoli, 2002: Application of a perturbation recycling method in the large-eddy simulation of a mesoscale convective internal boundary layer. *J. Atmos. Sci.*, **59**, 2385-2395.
- Miller, D. M., W. A. R. Brinkmann, and R. G. Barry, 1974: Windstorms: A case study of wind hazards for Boulder Colorado, in G. F. White (ed.), *Natural Hazards: Local, national global*, Ch. 10, Oxford University Press, New York, p, 80-86.
- Mobbs, S. D., S. B. Vosper, P. F. Sheridan, R. Cardoso, R. R. Burton, S. J. Arnold, M. K. Hill, V. Horlacher, and A. M. Gadian., 2005: Observations of downslope winds and rotors in the Falkland Islands. *Q. J. R. Meteorol. Soc.*, **131**, 329-351.

- Norte, F. A., 1988: Características del viento Zonda en la región de Cuyo. Ph.D. thesis, Buenos Aires University, 355 pp. [Available from Programa Regional de Meteorología, Instituto Argentino de Nivología, Glaciología y Ciencias Ambientales, Centro Regional de Investigaciones Científicas y Técnicas (CRICYT)/CONICET, Calle Bajada del Cerro s/n (5500) Mendoza, Argentina.]
- Olafsson, H., and P. Bougeault, 1997: The effect of rotation and surface friction on orographic drag. *J. Atmos. Sci.*, **54**, 193-210.
- Orlanski, I., 1976: A simple boundary condition for unbounded hyperbolic flows. *J. Comput. Phys.*, **21**, 251-269.
- Peltier, W. R., and T. L. Clark, 1979: The evolution and stability of finite-amplitude mountain waves. Part II: Surface wave drag and severe downslope windstorms. *J. Atmos. Sci.*, **36**, 1498-1529.
- Peng, S., and W. T. Thompson, 2003: Some aspects of the effect of surface friction on flows over mountains. *Q. J. R. Meteorol. Soc.*, **129**, 2527-2557.
- Poulos, G. S., J. E. Bossert, T. B. McKee, and R. A. Pielke, 2000: The interaction of katabatic flow and mountain waves. Part I: Observations and idealized simulations. *J. Atmos. Sci.*, **57**, 1919-1936.
- Richard, E., P. Mascart, and E. C. Nickerson, 1989: The role of surface friction in downslope windstorms. *J. Appl. Meteor.*, **28**, 241-251.
- Rotunno, R., and P. K. Smolarkiewicz, 1995: Vorticity generation in the shallow-water equations as applied to hydraulic jumps. *J. Atmos. Sci.*, **52**, 320-330.
- Seluchi, M. E., F. A. Norte, P. Satyamurty, and S. C. Chou, 2003: Analysis of three situations of the foehn effect over the Andes (Zonda wind) using the Eta-CPTEC regional model. *Weather and Forecasting.*, **18**, 481-501.
- Skyllingstad, E. D., 2003: Large eddy simulation of katabatic flows. *Boundary-Layer Meteor.*, **106**, 217-243.
- Skyllingstad, E. D., and H. W. Wijesekera, 2004: Large eddy simulation of flow over obstacles: High drag states and mixing. *J. Phys. Oceanogr.*, **34**, 94-112.
- Smith, C. M. and Skillingstad, E. D., 2005: Numerical simulation of katabatic flow with changing slope angle: *Mon. Wea. Rev.*, **133**, 3065-3080.

- Smith, C. M. and Skillingstad, E. D., 2009: Investigation of upstream boundary layer influence on mountain wave breaking and lee wave rotors using a large eddy simulation: *J. Atmos. Sci.*, **66**, 3147-3164.
- Smith, C. M. and Skillingstad, E. D., 2010: An inversion based instability mechanism for downslope windstorms: *In review*.
- Smith, R. B., 1985: On severe downslope winds: *J. Atmos. Sci.*, **42**, 2597-2603.
- Smith, R. B., Q. Jiang and J. Doyle, 2006: A theory of gravity wave absorption by a boundary layer. *J. Atmos. Sci.*, **63**, 774-781.
- Smolarkiewicz, P. K., and L. G. Margolin, 1994: Variational solver for elliptic problems in atmospheric flows. *Appl. Math. Comput. Sci.*, **4**, 527-551.
- Steppeler, J. H.-W. Bitzer, M. Minotte, and L. Bonaventura, 2002: Nonhydrostatic atmospheric modeling using a z-coordinate representation. *Mon. Wea.Rev.*, **130**, 2143-2149.
- Vosper, S. B., 2004: Inversion effects on mountain lee waves. *Q. J. R. Meteorol. Soc.*, **130**, 1723-1748.
- Winters, K. B. and E. A. D'Asaro, 1994: Three-dimensional wave instability near a critical level. *J. Fluid Mech.* **272**, 255-284.
- Ying, Q., and F. Baopu, 1993: A theoretical study on the interaction between airflow over a mountain and the atmospheric boundary layer. *Boundary-Layer Meteor.*, **64**, 101-126.
- Zhong, S., J. Li, C. B. Clements, S. F. J. De Wekker, and X. Bian, 2008: Forcing mechanism for the Washoe Zephyr. *Journal of Applied Meteorology and Climatology*, **47**, 339-350.